Shock and Vibration

# Advanced Condition Monitoring Methods of Mechanical Systems for Industry Applications

Lead Guest Editor: Liu Jing
Guest Editors: Min Xia, Wei Wu, and Xiaohua Song

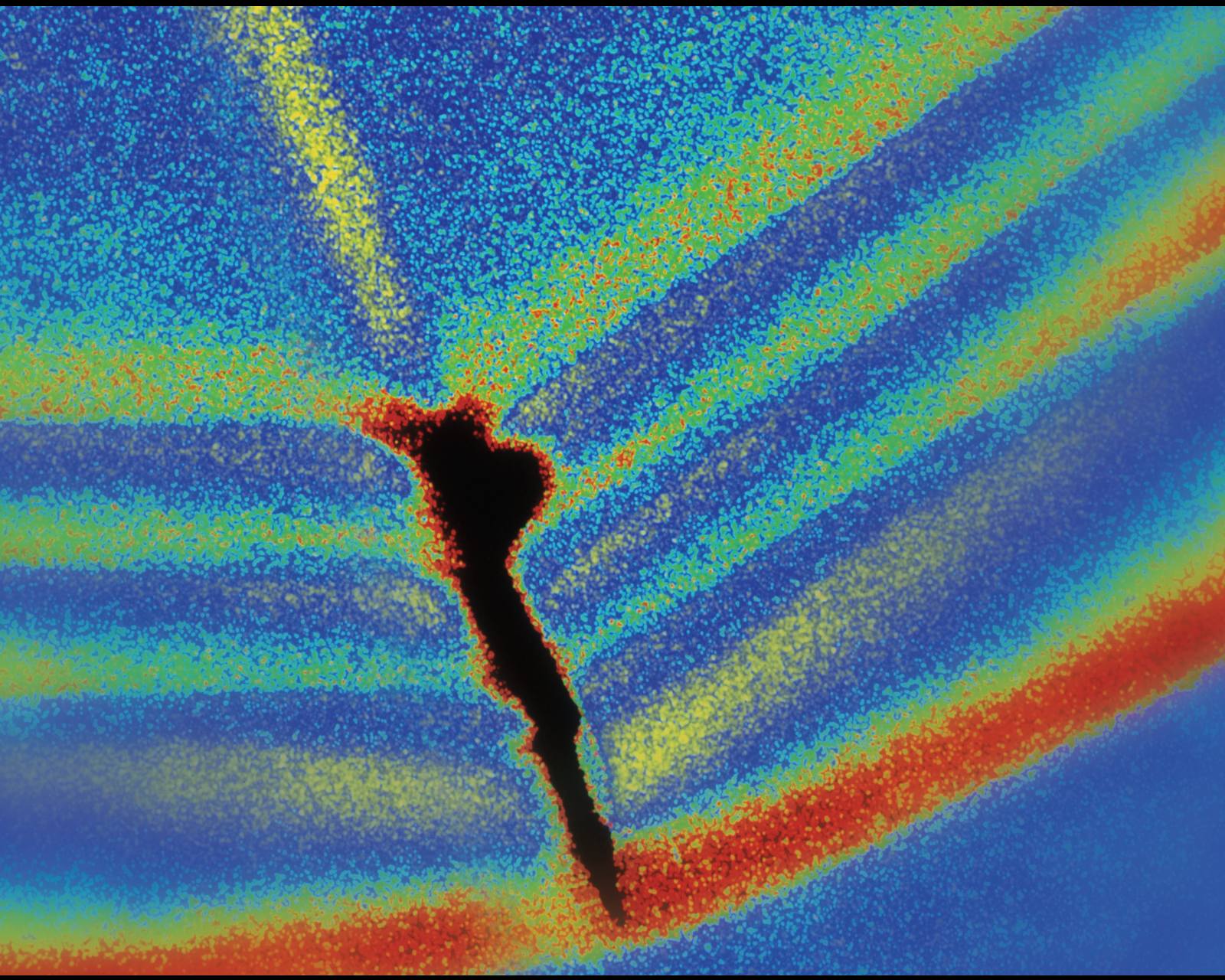

# Advanced Condition Monitoring Methods of Mechanical Systems for Industry Applications

Shock and Vibration

# Advanced Condition Monitoring Methods of Mechanical Systems for Industry Applications

Lead Guest Editor: Liu Jing
Guest Editors: Min Xia, Wei Wu, and Xiaohua Song

# Chief Editor



## Associate Editors



## Academic Editors

# Contents

**Remaining Useful Life Prediction of Milling Tool Based on Pyramid CNN**
Ning Hu, Zhenguo Liu, Shixin Jiang, Quanzhou Li, Shuqi Zhong, and Bingquan Chen
Research Article (14 pages), Article ID 1830694, Volume 2023 (2023)

**A New Dynamic Balance Framework Based on Blind Source Separation under Multiple Fault Conditions**
Bo Lang, Xinyi Zhang, Jun Xiao, Shouhang Lu, and Bing Li
Research Article (14 pages), Article ID 4059824, Volume 2022 (2022)

**Three-Level SOC Equalization Control Strategy for MMC-BESS Based on Feedforward Sliding Window Integral Method**
Yuan Cheng, Hui Zhang, Xiaohui Wei, and Wenquan Shao
Research Article (19 pages), Article ID 1546622, Volume 2022 (2022)

**A Composite Method of Marine Shafting's Fault Diagnosis by Ship Hull Vibrations Based on EEMD**
Xiaofei Wen, Wenjie Meng, Xiaoxiao Sun, and Ruiping Zhou
Research Article (11 pages), Article ID 1236971, Volume 2022 (2022)

**Vibration Transmission Characteristics and Measuring Points Analysis of Bearing Housing System**
Wenbing Tu, Jinwen Yang, Ya Luo, Lianbao Jiang, Jin Xu, and Wennian Yu
Research Article (12 pages), Article ID 4334398, Volume 2022 (2022)

Hindawi
Shock and Vibration
Volume 2023, Article ID 1830694, 14 pages
https://doi.org/10.1155/2023/1830694

*Research Article*

# Remaining Useful Life Prediction of Milling Tool Based on Pyramid CNN

**Ning Hu**[1,2], **Zhenguo Liu**[1,2], **Shixin Jiang**[1,2], **Quanzhou Li**[1,2], **Shuqi Zhong**[1,2] and **Bingquan Chen**[1,2]

[1]*China Electronic Product Reliability and Environmental Test Institute, Guangzhou 510610, China*
[2]*Key Laboratory of Industrial Equipment Quality Big Data, MIIT, Guangzhou 510610, China*

Correspondence should be addressed to Shixin Jiang; jiangshixinwh@163.com

Received 16 June 2022; Revised 18 October 2022; Accepted 24 November 2022; Published 11 February 2023

Academic Editor: Liu Jing



Remaining useful life prediction of a milling tool is one of the determinants in making scientific maintenance decision for the CNC machine tool. Predicting the RUL accurately can improve machining efficiency and the quality of product. Deep learning methods have strong learning capability in RUL prediction and are extensively used. Multiscale CNN, a typical deep learning model in RUL prediction, has a large number of parameters because of its parallel convolutional pathways, resulting in high computing cost. Besides, the MSCNN ignores various influences of different scales of degradation features on RUL prediction accuracy. To address the issue, a pyramid CNN (PCNN) is proposed for RUL prediction of the milling tool in this paper. Group convolution is used to replace parallel convolutional pathways to extract multiscale features without additional large number of parameters. And the channel attention with soft assignment is used to select the key degradation features, considering different sensors and scales. The milling tool wear experiments show that the score value of the proposed method achieved $51.248 \pm 1.712$ and the RMSE achieved $19.051 \pm 0.804$, confirming better performance of the proposed method compared with the traditional MSCNN and other deep learning methods. Besides, the number of parameters of the proposed method is reduced by 62.6% and 54.8% compared with the MSCNN with self-attention and the MSCNN methods, confirming its lower computing cost.

## 1. Introduction

As a basic tool of industry, computer numerical control (CNC) machine tool plays an important role in industrial manufacture. With the increasing demand for product quality, stability of machining process becomes more and more important. Tool wear is a common negative effect on machining quality during the high-speed machining process [1]. And it not only affects the quality of machined surface and the machining precision but also results in increasing machining cost. Moreover, unnecessary tool replacement that aims at preventing the decrease in surface quality will increase the downtime and machining cost in high-speed milling [2]. The effects for tool degradation mainly include cutting parameters, work material, and cutting tool. However, the internal law of these effects on tool degradation is hard to determine for their various combinations. Since it could not be directly detected during the process, it is hard to make scientific maintenance decisions without interrupting the machining process. Therefore, a significative work is to accurately predict the remaining useful life (RUL) of the milling tool.

With the widely usage of industrial internet of thing in condition monitoring of machinery, a mass of monitoring data of the CNC machine tool are acquired by various sensors. The explosive growth of monitoring data brings new opportunities to RUL prediction of the milling tool. Compared with model-driven RUL prediction methods, data-driven RUL prediction methods are able to learn degradation characteristics of a tool from massive monitoring data. And it could also build the corresponding RUL prediction models automatically, which means neither deep understanding of system-failure physics nor complete knowledge of the dynamics is required. Therefore, data-

driven RUL prediction methods are gaining more and more attention in the field of RUL prediction recently [3].

Traditional data-driven prognostic approaches usually contain three steps: hand-crafted feature extraction, degradation behavior learning, and RUL prediction [4, 5]. Hand-crafted feature extraction is to use signal process methods to extract sensitive degradation features from the monitoring data. Then, these features are fed into machine learning models, such as ridge regression, support vector machine (SVM), and so on, to learn the degradation features and predict the RUL. For example, Park et al. [6] extract time, frequency, and time-frequency domain features, and these features are input into the ridge regression model after dimension reduction using PCA. Zhao et al. [7] extract high-dimensional feature using time-frequency representation (TFR), which are fed into the simple multiple linear regression model to predict the RUL after supervised dimensionality reduction using PCA and LDA. Liu et al. [8] used the integration of empirical mode decomposition (EMD) and Wigner–Ville distribution (WVD) to extract degradation feature from gearbox vibration signal, and then particle filter (PF) with the state space model based on the Wiener process is used to predict the RUL of gearbox considering degradation feature. Even though these methods have a good performance on the RUL prediction, they still need to take much effort on hand-crafted feature design [9, 10]. To avoid this situation, it is desirable to find a new method to automatically extract degradation feature from monitoring data. Therefore, deep learning-based RUL prediction methods have gained more and more attention in the field of data-driven RUL prediction [11–20].

Deep learning, structured by a stack of multiple layers of nonlinear processing units [21], can extract high-level feature without human intervention. Thus, deep learning shows a more powerful feature extraction ability, and achieves state-of-the-art accuracy in many tasks, such as image classification, natural language processing (NLP), target detection, and so on. Deep belief network (DBN), auto-encoder network (AEN), recurrent neural network (RNN), and convolution neural network (CNN) are mainstream architectures in deep learning [22]. Wang et al. [23] proposed a deep separable convolution network (DSCN) for RUL prediction of bearing, which extracted the degradation feature from monitoring data using deep separable convolution and predicted the RUL using fully connected layers. Hinchi and Tkiouat [24] used CNNS to extract features from vibration signal, and then employed LSTM to predict the RUL of rolling element bearings. Zhang et al. [25] proposed a multiobjective DBN ensemble method for RUL prediction of turbofan engines. Wang et al. [26] use DCAE and SOM to gain the health index of rolling bear, and then use this health index as a label to train a CNN-based RUL prediction model to predict the RUL. Ding et al. [27–29] proposed three meta deep learning methods to predict the RUL of the machine under different conditions and limited and variable-length data. Zhang et al. [30] proposed a deep representation regularization-based transfer learning method for remaining useful life predictions under different machinery operating conditions and no target-domain run-to-failure training data.

Because of the remarkable ability of extracting degradation features from monitoring data, CNN-based RUL prediction methods become a research hotspot, especially the multiscale CNN (MSCNN) [31–39]. The architecture of traditional MSCNN with self-attention is shown in Figure 1. Parallel convolutional pathways are used to extract different scales of degradation features, which is developed by different size of convolution kernel for different convolutional pathways. And the self-attention is embedded to avoid the interference caused by the redundant and uncorrelated information of partial sensors, improving the performance of the networks. The usage of parallel learning strategy, however, greatly increases the parameters of the model, leading to higher cost of computing during model training. The self-attention, in addition, can only consider the contribution of different sensors to RUL prediction. In other words, the contribution of different scale of degradation features is not taken into account.

To deal with the mentioned problems, a pyramid CNN (PCNN) is proposed in this paper. The architecture of the proposed PCNN is shown in Figure 2. The monitoring data acquired from different sensors can be directly fed into the proposed network without any preprocessing, which means complex signal processing techniques do not require. This network contains two parts, multiscale feature learning subnetwork and RUL predicting subnetwork. The multiscale feature learning subnetwork is built by stacking one-dimensional (1D) convolution layers and pyramid convolution layers. Low-level features are extracted by the one-dimensional (1D) convolution layers and fed into the pyramid convolution layers. In the pyramid convolution layers, group convolution is used to extract multiscale high-level degradation features. Then, the channel attention model is used to generate attention weight for each channel. A soft assignment is used to recalibrate the attention weight of different scales so that the key degradation features can be selected from not only different sensors but also from different scales. The RUL predicting subnetwork contains global pooling and fully connected layers (FCLs). The mapping relationship between degradation features and the RUL is established in these parts. The tool wear experiment is used to verify the proposed method. Compared with the traditional MSCNN, the proposed method has higher accuracy of RUL prediction and smaller number of parameters.

The rest of this article is structured as follows. The basic theory of the proposed method is expounded in detail in Section 2. Experiment and comparison analyses are illustrated in Section 3. Conclusions are composed in Section 4.

## 2. Proposed PCNN for RUL Prediction of Milling Tool

*2.1. One-Dimensional (1D) Convolution Layer and Shortcut Connection.* On-dimensional convolution is used to extract degradation feature from raw data in this paper. The 1-*D* convolutional operation can be described as

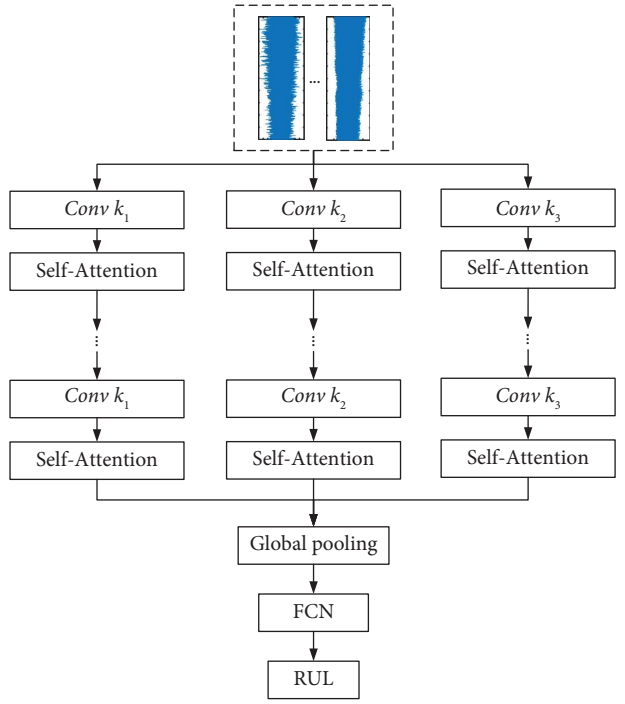


Figure 1: The architecture of traditional MSCNN with attention mechanism.

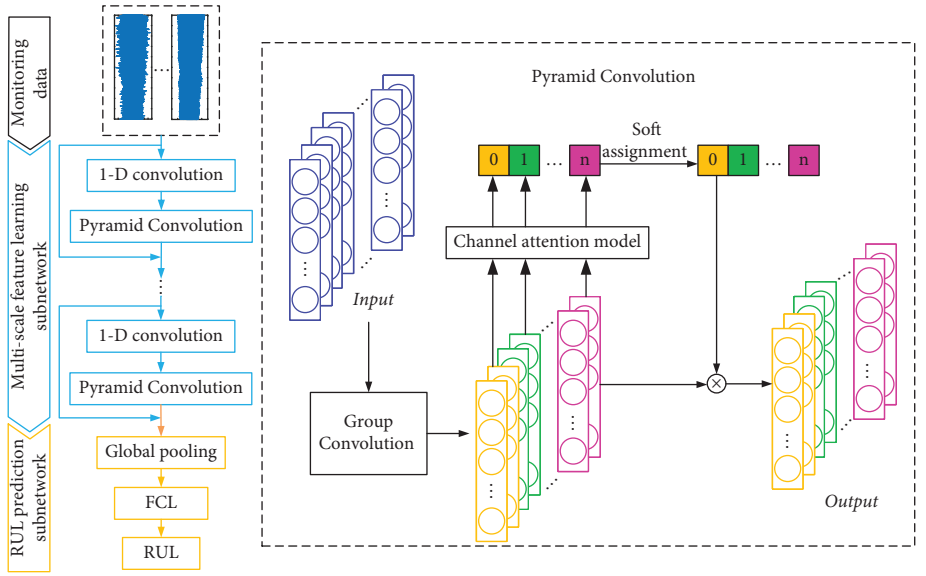


Figure 2: The architecture of the proposed PCNN.

$$y_0 = f\left(\sum_{i=1}^{n} k_{0,i} * X_0 + b_{0,i}\right), \tag{1}$$

where $X_0$ is the raw data, $y_0$ is the output of the process, $k_{0,i}$ is the learnable convolutional kernel, $b_{0,i}$ is the bias tern, $*$ represent the convolutional operation, and $f(\cdot)$ is the nonlinear activation function. In this paper, the rectified linear unit (ReLU) is used as the nonlinear activation function of the 1-$D$ convolution operation. By repeating this process twice, low-level degradation features, denoted as $F_0$, can be obtained.

Gradient vanishing/exploding and weight matrix degradation is a considerable problem of deep learning. To address this issue, shortcut connection is introduced in this network.

The raw data acquired from the sensor is fed into the shortcut connection pathway, which contains a convolution layer and a max pooling layer. The size of the convolutional kernel in the shortcut connection is $1 \times 1$, which aims to

increase the dimension of $X_0$. The max pooling layer is used to downsample the output of the convolution layer. The output of the shortcut connection model, denoted as $S_{\text{out}}$, is given by

$$S_{\text{out}} = Y + \text{pool}(k_c * X_0), \tag{2}$$

where $Y$ is the output of the pyramid convolution layer, $\text{pool}(\cdot)$ is the pooling function, $k_c$ is the convolution kernel with the size of $1 \times 1$, and $*$ is the convolution operation.

*2.2. Pyramid Convolution Layer.* In this layer, multiscale high-level degradation information from different sensors is extracted and fused. First, a group convolution operation is used to extract different scale of high-level degradation features. After doing this, the channel attention model is used to generate the attention weights of the multiscale features. Finally, the soft assignment is used to recalibrate the attention weight of the corresponding scale.

*2.2.1. Group Convolution.* The monitoring data acquired from the sensors are nonlinear signals containing a lot of noise. While the degradation features can be extracted by convolution operation, the receptive field range of the convolution kernels have great influence on the degradation features. Large-scale degradation features can be extracted by a larger receptive field, while detailed degradation features can be extracted by a smaller receptive field. Therefore, it is necessary to use different size of convolution kernels to extract multiscale degradation features. The traditional multiscale convolution uses parallel pathways to extract multiscale features. The size of convolution kernel in various convolution pathways is different. Although the performance of the network is proved, a large number of parameters increases the computing cost. Therefore, it is desirable to find an efficient multiscale feature extraction method.

In this paper, group convolution is used to replace parallel convolutional pathways so that multiscale features can be extracted without additional large number of parameters. The architecture of this model is shown in Figure 3.

The input low-level feature $F_0 \in \mathbb{R}^{L \times C}$ is splitted into $s$ groups along with the channel direction, denoted as $X_i \in \mathbb{R}^{L \times c/s}$, with $i = 1, 2, \ldots, s$, where $c$ is the number of channel and $L$ is the length of $F_0$. A set of learnable kernels is used to convolve $X_i$. The output of the convolution, denoted as $F_i$, can be obtained by

$$F_i = \sum_{c=1}^{\frac{c}{s}} k_{i,c} * X_i + b_{i,c}, \tag{3}$$

where $C/s$ is the number of learnable kernels and the number of input channels, $*$ denotes the convolution operator, $k_{i,c} \in \mathbb{R}^{F \times 1 \times (C/s) \times (C/s)}$ is the $c - th$ convolution kernel of the $i - th$ group, and $b_{i,c}$ is the bias term. Different convolution kernels $k_{i,c}$ have different sizes, which can extract different scales of degradation features. Finally, the whole multiscale feature can be obtained by the concatenation of all the $F_i$.

*2.2.2. Channel Attention Model and Soft Assignment.* The data from different sensors contain different degrees of degradation information. In other words, some important degradation information only exists in partial sensors. Furthermore, different scales of features also contain different degrees of degradation information. Therefore, it is important to select key degradation information from the multiscale feature $F$. In this paper, a channel attention model is used to obtain the attention weight from the input feature $F$. Then, the soft assignment is used to recalibrate the attention weight of the corresponding scale. The structure of this model is shown in Figure 4.

Attention weights of the features of different scales can be obtained by using parallel processing pathways. Each processing pathway includes global information encoding and channel-wise relationship information recalibrating. The global information encoding is done by global average pooling and global max pooling, and the channel-wise relationship information recalibrating is done by fully connected networks with one hidden layer.

The global average pooling (GAP) and the global max pooling (GMP) can aggregate the global information of each channel, generating two vectors: $V_a$ and $V_m$. Both $V_a$ and $V_m$ contain $J = C/s$ channel-wise statistics. The channel-wise statistics of the $j$-th channel $V_{a,j}$ and $V_{m,j}$ is obtained by

$$V_{a,j} = \frac{1}{P} \sum_{p}^{P} V_{a,j,p} V_{m,j} = \max\left(V_{m,j,p}\right). \tag{4}$$

Then, $V_a$ and $V_m$ are fed into the fully connected network (FCN) with one hidden layer. The neuron number of the hidden layer in the FCN is $J/r$, where $r$ is the ratio of dimensionality reduction. After that, the attention weight of $F_i$, denoted as $Z_i$, can be calculated by

$$Z_i = \sigma\left(W_{a2}\left(W_{a1} V_a\right) \oplus W_{v2}\left(W_{v1} V_m\right)\right), \tag{5}$$

where $W_{a1} \in \mathbb{R}^{J/R \times J}$, $W_{a2} \in \mathbb{R}^{J \times J/R}$, $W_{\text{v1}} \in \mathbb{R}^{J/R \times J}$, and $W_{\text{v2}} \in \mathbb{R}^{J \times J/R}$ are the weight matrices in the FCNs, $\oplus$ denotes the element-wise summation, and $\sigma(\cdot)$ is the sigmoid activation function.

By doing this, the network can fuse degradation information from different sensors and produce a better attention for high-level degradation feature. Furthermore, in order to enhance the key degradation features of some scales and suppress the irrelevant ones without destroying the original channel attention vector, a soft assignment is used to adaptively recalibrate the attention weight of the corresponding scale. After doing this, the key degradation features are selected not only from different sensors but also from different scales. The soft assignment is given by

$$\text{att}_i = \frac{\exp\left(Z_i\right)}{\sum_{i=o}^{s-1} \exp\left(Z_i\right)}. \tag{6}$$

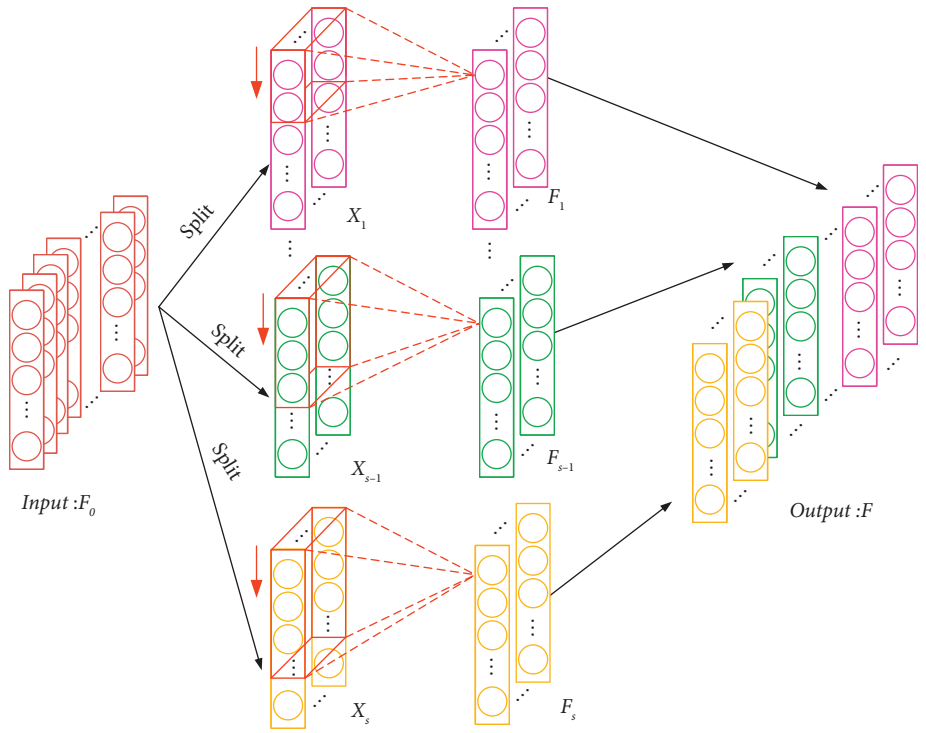


Figure 3: Architecture of the group convolution.

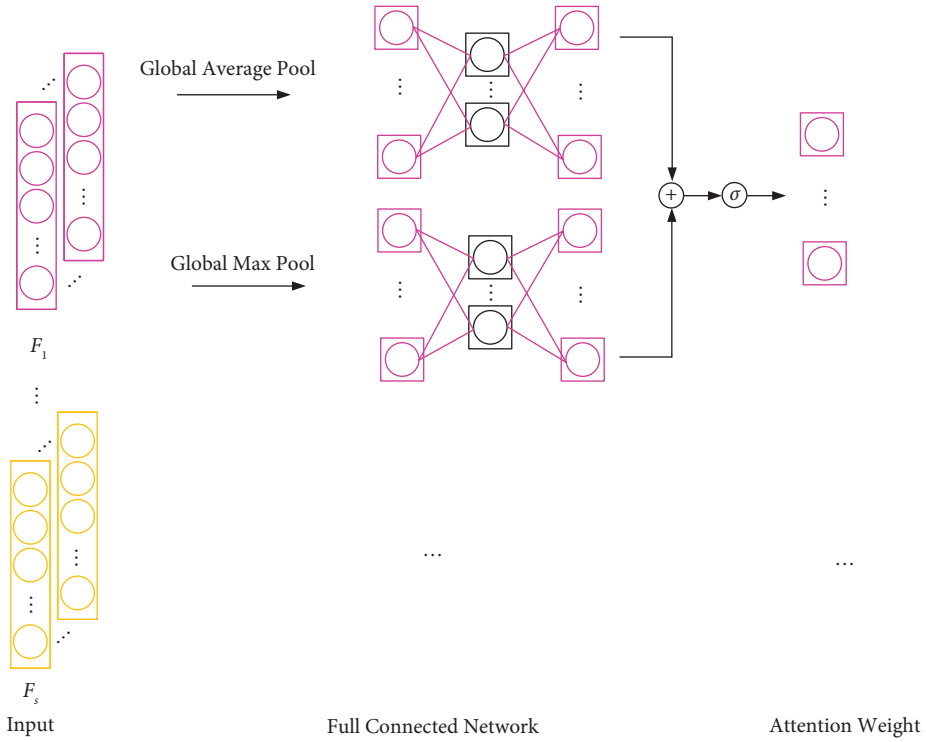


Figure 4: Architecture of the channel attention model.

Then, the multiscale high-level degradation feature with multiscale channel-wise attention weight, denoted as $Y_i$, can be obtained by

$$Y_i = F_i \odot \text{att}_i, \tag{7}$$

where $\odot$ is the channel-wise multiplication.

Finally, the output of the pyramid convolution layer, denoted as $Y$, can be obtained by the concatenation of all the $Y_i$.

## 3. Experimental Verification

*3.1. Data Description.* As shown in Figure 5, the life testing of the milling tool is conducted in a computer numerical control (CNC) milling machine.

The material of the workpiece is 316L stainless steel, and the milling tool is cemented carbide insert deposited by TiAlN coating. During the milling process, the table feeds the workpiece from front to back along the $Y$-axis. As tabulated in Table 1, a total of 4 milling tool are tested and all tests are carried out without the application of a cutting fluid. As shown in Figure 6, two types of sensors are installed in the milling machine, including accelerometer (Kistler Z292A600) and rotary dynamometer (Pro-Micro). For the accelerometer, the sampling frequency is set as 10 kHz. For the rotary dynamometer, the sampling frequency is set as 2.5 kHz.

As shown in Figure 6, a metallographic microscope is used to measure the width of the flank wear. When the width of the flank wear is greater than 0.2 mm, the tested tool wear achieves the limit [1]. The acquired monitoring data of the $C1$ during the whole operating life is shown in Figure 7.

As shown in Figure 7, some of these monitoring data have obvious degradation trends with the increasing of cutting time, while others do not have these trends.

*3.2. Experimental Study.* In this case, all of the monitoring data are used as the input of the network to verify the effectiveness of the proposed method. The size of an input sample is $10000 \times 1 \times 5$.

One of the main hyperparameters that may affect the prediction performance of the proposed model is the number of groups, which directly affects the dimension of feature extract in the pyramid convolution layer. For investigating this influence, different number of groups in the proposed PCNN are applied to estimate the RUL prediction. The number of groups is set to be 2, 4, and 8. Figure 8 shows the score values and RMSE of $C4$, and the corresponding training time and model parameters are given in Table 2.

It can be observed that the score value is the lowest and the RMSE is the highest when the number of group is set to be 2, which indicates that the prediction performance is relatively poor. The accuracy of the RUL prediction results is closer for others. As the number of groups increased, the model becomes more computationally intensive. Therefore, it can be observed in Table 2 that the model training time and the number of parameters increased with the increase in the number of groups. Though a bigger number of groups can extract more features of different scales, resulting in better prediction performance, the calculation burden is aggravated and the performance improvement is limited when the number of group increases to a certain extent. By the trade-off between accuracy and efficiency, the number of groups is finally selected as 4.

The final architecture of the network is shown in Figure 9. And the hyperparameters of the pyramid convolution layer of the PCNN are listed in Table 3.

Mean square error is used as the loss function of the network and Adam optimizer with a mini-batch size of 128 is used to update its weights and biases. The trained network is used to predict the RUL values of the testing dataset after training 150 epochs. If the prediction value was bigger than the actual value, it may cause low process quality or even a scrapped products due to a overwear in the tool. Taking this situation into account, except for root mean square error (RMSE), a score function is used to evaluate the performance of the network. The score value is given by

$$\begin{aligned} \text{Score} &= \frac{1}{S}\sum_{i=1}^{S} S_i, \\ S_i &= \begin{cases} 100 * \exp^{-\ln(0.5)\cdot(y-\widehat{y}/5),} & y \le \widehat{y}, \\ 100 * \exp^{\ln(0.5)\cdot(y-\widehat{y}/20),} & y > \widehat{y}, \end{cases} \end{aligned} \tag{8}$$

where $S$ is the number of samples in the testing dataset, $y$ is the actual value, and $\widehat{y}$ is the predicted value. The higher the score values, the more accurate the performance of the RUL prediction is.

Figure 10 shows the RUL prediction result of $C4$ using the proposed method. As shown in Figure 10, the predicted RUL value fluctuates slightly with the actual RUL, and the fluctuation becomes smaller and smaller with the increase of the cutting time. Furthermore, cross validation is used to prove the stability of the proposed method. Each test is repeated ten times, and the mean and standard deviation of these four testing dataset are listed in Table 4.

As shown in Table 4, on the one hand, both score and RMSE of each testing dataset has small standard deviation, which proves that the proposed model has good stability for the same task. On the other hand, the mean value of both score and RMSE of these four testing dataset has small fluctuation, which proves that the proposed network has good stability for different tasks. In conclusion, the proposed network has a good prediction result and good stability in both the same task and the different task, which means the predicted result of the proposed method is credible.

*3.3. Comparison Analysis*

*3.3.1. Ablation Experiments.* In order to illustrate the advantage of the proposed PCNN, ablation experiments are done in this part. The other three prognostic networks are employed to predict the RUL and they are denoted as Network-1, Network-2, and Network-3. The architectures of these three networks are similar to that of the PCNN, and the differences are that (1) Network-1 does not use group convolution and channel attention with soft assignment, (2) Network-2 only use group convolution, and (3) Network-3 only use channel attention with soft assignment. In addition, the hyperparameters settings of these three networks are the same as those of the PCNN, and the cross validation used in

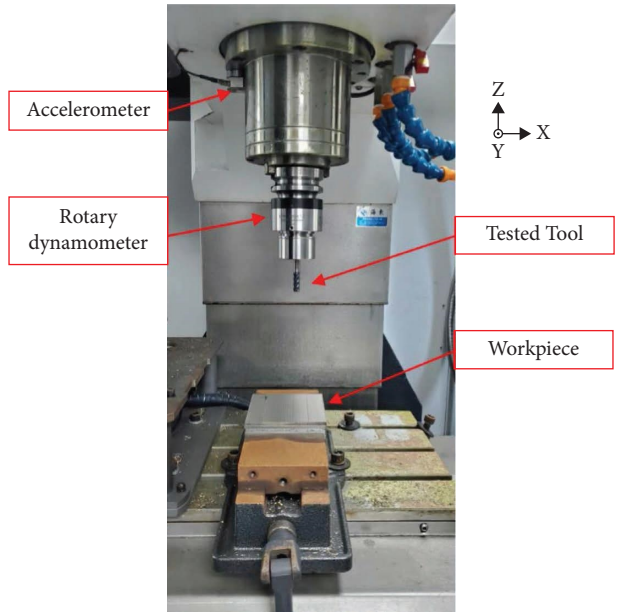


Figure 5: CNC machine and sensor placement.

Table 1: Cutting condition of milling tool.

| Spindle speed | Feed rate | Depth of cut | Width of cut | Dataset |
|---|---|---|---|---|
| 3500 rpm | 300 mm/min | 2 mm | 2 mm | *C*1, *C*2, *C*3, and *C*4 |

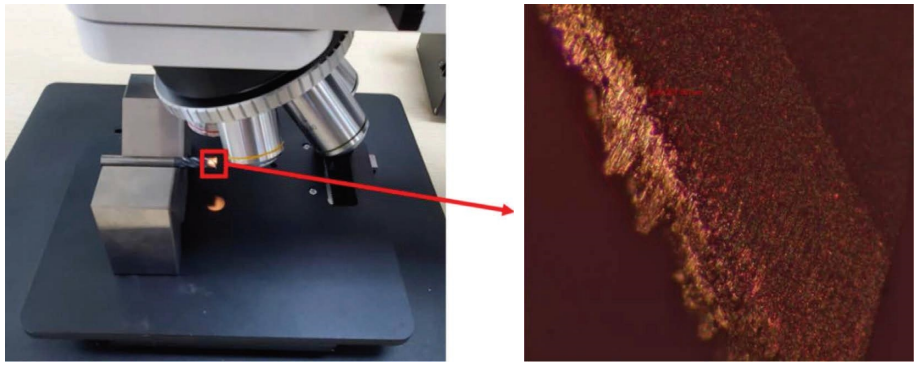

Figure 6: Milling tool deterioration photograph.

Section 3.2 is used in this part too. The performance estimation results of these four different networks are listed in Table 5 and drawn in Figure 11.

It can be observed that compared with the classic multiscale convolutional network without attention mechanisms (i.e., Network-1 [37]), the use of group convolution or channel attention with soft assignment effectively improves the prediction performance and stability of the network, resulting in higher score value and lower RMSE. For Network-2, the performance improvement is attributed to the use of group convolution, which reduces the risk of overfitting by reducing the number of learning parameters. For Network-3, the employment of channel attention with soft assignment make the network enhance key degradation features of some sensors and scales. Besides, it is to be noted that through systematically integrating group convolution and soft attention with soft assignment, the proposed PCNN obtains the highest score value and the lowest RMSE value for each testing dataset among four different prognostic networks, which verifies again the performance of the proposed method.

*3.3.2. Comparison with the State-of-the-Art Models.* In this part, eight state-of-the-art models, including two machine learning models, random forests (RF), and support vector

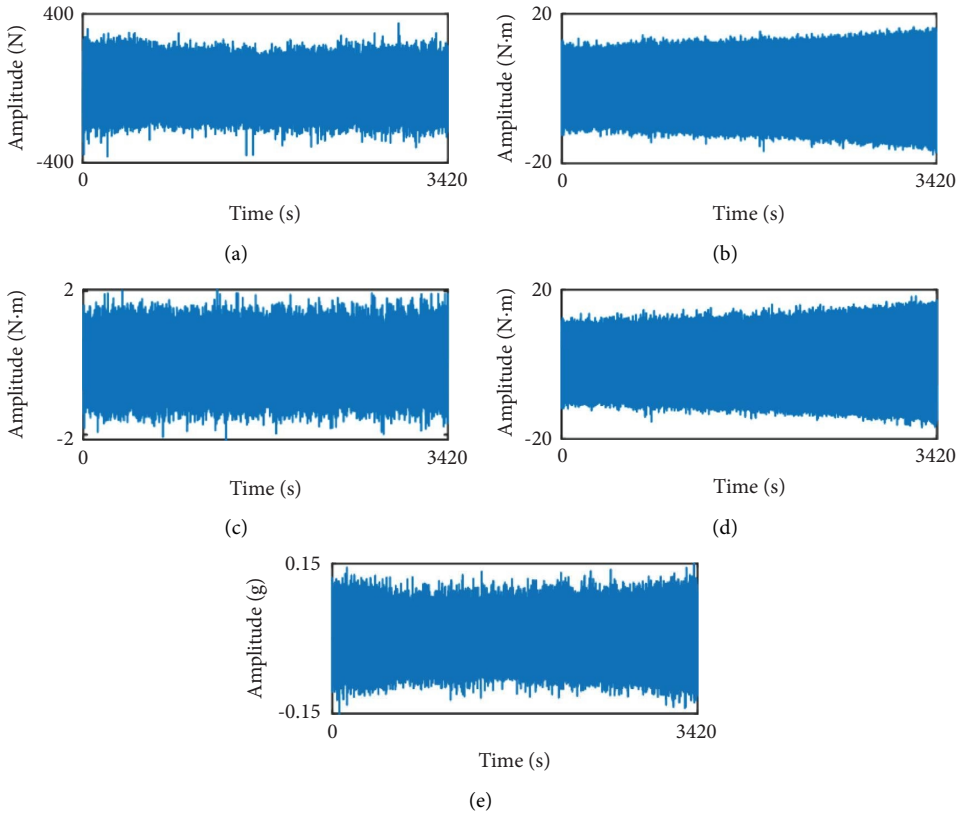


Figure 7: Monitoring data of the $C1$ during the whole operating life. (a) Force data in the $Z$-axis. (b) Bending moment data in the $X$-axis. (c) Torque data. (d) Bending moment data in the $Y$-axis. (e) Vibration data in the $Y$-axis.

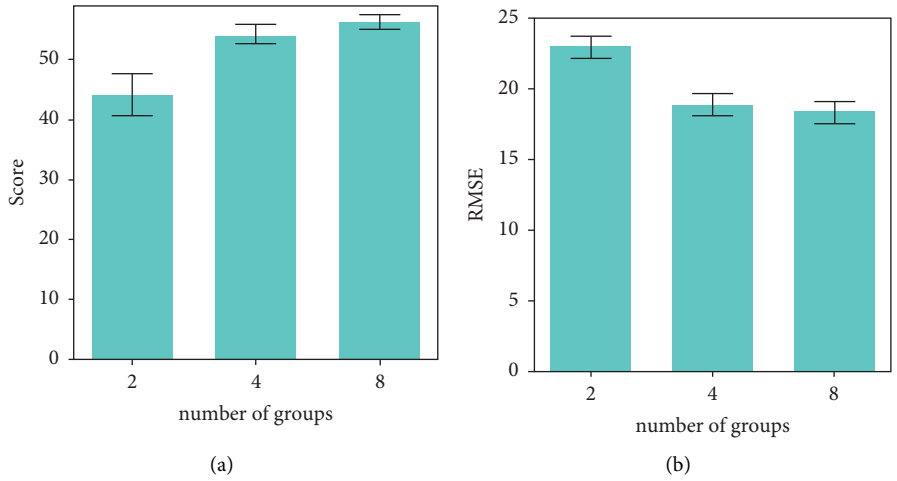


Figure 8: RUL prediction result of $C4$ based on different number of groups. (a) Score values. (b) RMSE.

regression (SVR) [34] and six deep learning model, deep convolution neural network (DCNN) [35], residual dense network (RDN) [36], multiscale convolutional neural network (MSCNN) [37], convolutional long-short-term memory network (CLSTM) [24], deep belief networks (DBN) [38], and multiscale convolutional attention network (MSCAN) [39] are utilized to estimate the RUL for the comparison analysis. For the RF and SVR, features listed in [34] are extracted from all the monitoring data. Then, these features are fed into the corresponding model to predict the RUL. The score value and RMSE of these methods are listed in Table 6. Both score value and RMSE are calculated form the half of the life too.

From Table 6, it can be found that the proposed method has the highest score value and the lowest RMSE, which confirms the proposed method can predict the RUL

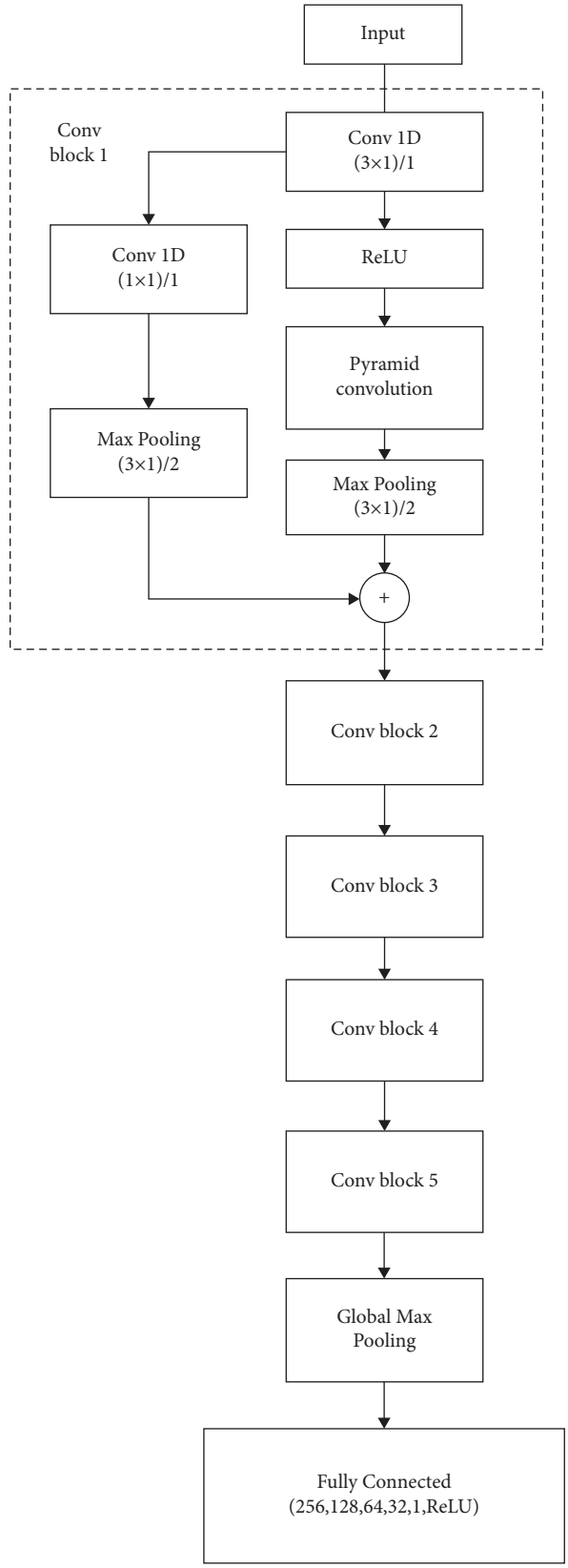


Figure 9: Architecture of the proposed PCNN.

Table 2: Comparison of model parameters and training time with different numbers of groups.

| Number of groups | 2 | 4 | 8 |
|---|---|---|---|
| Training time (s) | 1100 | 1230 | 1353 |
| Total model parameters | 613,225 | 765,993 | 1,115,425 |

Table 3: Hyperparameters of the pyramid convolution layer.

| Hyperparameters | Values |
|---|---|
| The ratio of dimensionality reduction $r$ | 4 |
| Size of convolution kernel $k_i$ with $i = 1, 2, ..., s$ | $3 \times 1$, $5 \times 1$, $7 \times 1$, $9 \times 1$ |
| Number of group $s$ | 4 |

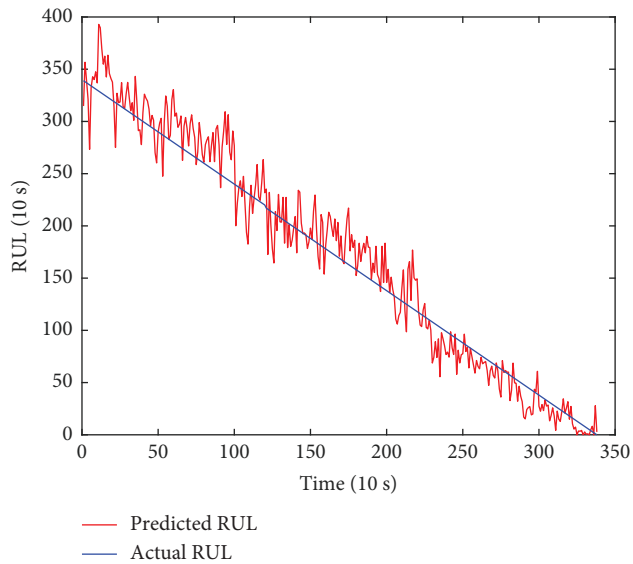


Figure 10: RUL prediction result of $C4$ using the proposed method.

Table 4: Performance estimation result of four testing dataset.

| Testing datasets | Scores | RMSE |
|---|---|---|
| $C1$ | $50.962 \pm 1.813$ | $19.374 \pm 0.923$ |
| $C2$ | $51.217 \pm 1.872$ | $19.139 \pm 0.853$ |
| $C3$ | $50.771 \pm 1.617$ | $19.424 \pm 0.721$ |
| $C4$ | $51.248 \pm 1.712$ | $19.051 \pm 0.804$ |

Table 5: Performance estimation result of four different networks.

| Testing datasets | | Network-1 | Network-2 | Network-3 | PCNN |
|---|---|---|---|---|---|
| $C1$ | Score | $40.152 \pm 7.486$ | $42.934 \pm 5.063$ | $47.013 \pm 4.828$ | $\mathbf{53.962 \pm 1.813}$ |
| | RMSE | $29.407 \pm 1.712$ | $25.122 \pm 1.592$ | $23.114 \pm 1.581$ | $\mathbf{19.374 \pm 0.923}$ |
| $C2$ | Score | $40.274 \pm 7.397$ | $43.771 \pm 4.811$ | $48.167 \pm 4.765$ | $\mathbf{52.217 \pm 1.872}$ |
| | RMSE | $28.903 \pm 1.664$ | $24.913 \pm 1.428$ | $23.022 \pm 1.412$ | $\mathbf{19.139 \pm 0.853}$ |
| $C3$ | Score | $39.914 \pm 8.152$ | $43.912 \pm 4.702$ | $48.369 \pm 4.105$ | $\mathbf{52.771 \pm 1.617}$ |
| | RMSE | $29.729 \pm 1.677$ | $24.502 \pm 1.437$ | $23.216 \pm 1.241$ | $\mathbf{19.424 \pm 0.721}$ |
| $C4$ | Score | $40.889 \pm 7.109$ | $44.068 \pm 4.155$ | $48.154 \pm 3.907$ | $\mathbf{54.248 \pm 1.712}$ |
| | RMSE | $28.597 \pm 1.402$ | $23.662 \pm 1.339$ | $22.901 \pm 1.209$ | $\mathbf{19.051 \pm 0.804}$ |

The bold values express that the PCNN has the best performance.

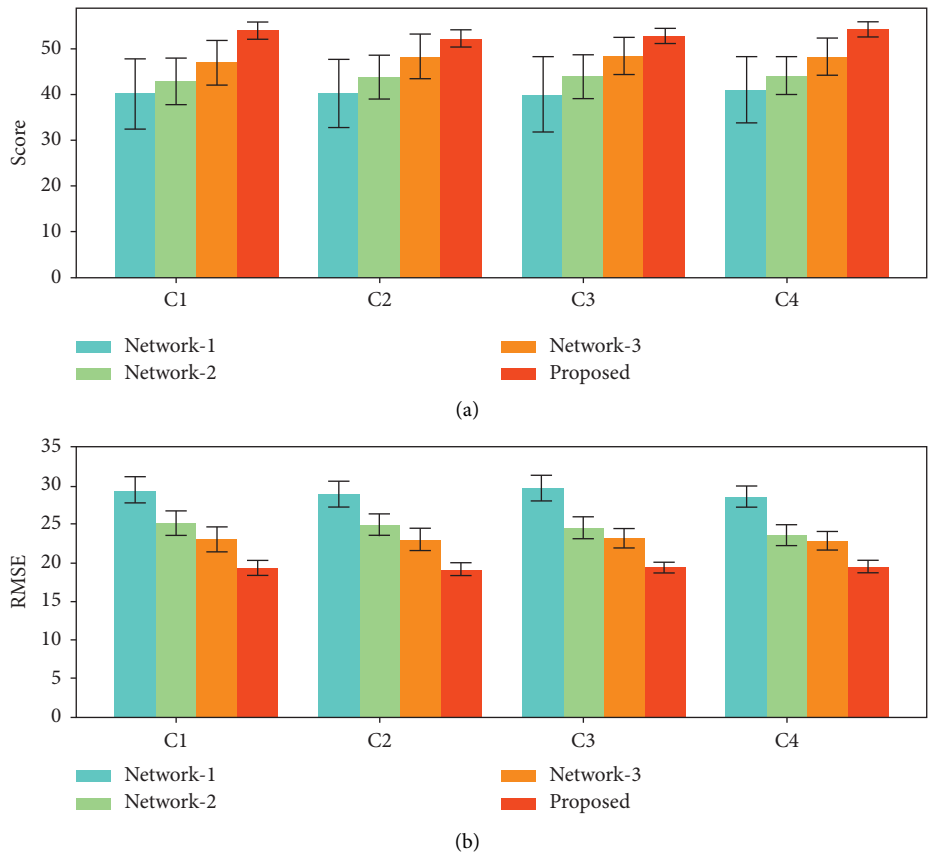


Figure 11: Performance estimation result of four different networks. (a) Score values. (b) RMSE values.

accurately. This performance enhancement demonstrates again the advantage of the PCNN.

Besides, in order to illustrate the efficiency of the PCNN, the number of parameters and the training and testing time of three multiscale learning models are listed in Table 7. All experiments in this paper are performed on a server configured with two Intel (R) Xeon (R) Gold 6242R CPU@ 3.10 GHz processors, eight NVIDIA GeForce RTX 3090 graphics cards, and a total of 512 GB memory (RAM).

As shown in Table 7, the total model parameters of the proposed method are respectively reduced by 62.6% and 54.8% compared to the MSCNN with self-attention and the MSCNN methods. Both training time and testing time of the proposed method are greatly reduced, which means

Table 6: Performance estimation result of the testing dataset for eight state-of-the-art models.

| Methods | Scores | | | | RMSE | | | |
|---|---|---|---|---|---|---|---|---|
| | *C*1 | *C*2 | *C*3 | *C*4 | *C*1 | *C*2 | *C*3 | *C*4 |
| DCNN [35] | 5.572 ± 10.297 | 4.835 ± 10.112 | 5.214 ± 10.822 | 5.713 ± 10.640 | 44.694 ± 2.558 | 45.206 ± 2.353 | 44.967 ± 2.301 | 44.515 ± 2.140 |
| SVR [34] | 16.997 ± 9.125 | 16.935 ± 9.002 | 17.279 ± 8.910 | 17.529 ± 8.812 | 39.012 ± 1.213 | 39.245 ± 1.221 | 38.914 ± 1.208 | 38.839 ± 1.194 |
| DBN [38] | 38.114 ± 5.198 | 38.202 ± 5.109 | 38.883 ± 4.950 | 39.163 ± 4.792 | 30.891 ± 1.315 | 31.048 ± 1.382 | 31.008 ± 1.213 | 30.427 ± 1.290 |
| RDN [36] | 31.341 ± 9.914 | 31.840 ± 9.757 | 32.019 ± 9.857 | 32.498 ± 9.309 | 29.890 ± 1.811 | 29.784 ± 1.887 | 29.560 ± 1.891 | 29.216 ± 1.921 |
| MSCNN [37] | 40.152 ± 7.486 | 40.274 ± 7.397 | 39.914 ± 8.152 | 40.889 ± 7.109 | 29.407 ± 1.712 | 28.903 ± 1.664 | 29.729 ± 1.677 | 28.597 ± 1.402 |
| CLSTM [24] | 45.331 ± 4.980 | 45.519 ± 4.832 | 45.712 ± 4.962 | 45.870 ± 4.954 | 28.245 ± 1.290 | 28.552 ± 1.285 | 28.771 ± 1.297 | 28.245 ± 1.314 |
| MSCAN [39] | 32.497 ± 2.244 | 32.575 ± 2.225 | 32.573 ± 2.294 | 32.814 ± 2.106 | 28.612 ± 1.104 | 28.504 ± 1.123 | 28.482 ± 1.109 | 28.374 ± 1.011 |
| RF [34] | 40.126 ± 2.268 | 40.125 ± 2.740 | 40.219 ± 2.442 | 40.370 ± 2.589 | 21.441 ± 1.071 | 21.372 ± 1.096 | 21.457 ± 1.101 | 21.371 ± 1.002 |
| Proposed | **53.962 ± 1.813** | **52.217 ± 1.872** | **52.771 ± 1.617** | **54.248 ± 1.712** | **19.374 ± 0.923** | **19.139 ± 0.853** | **19.424 ± 0.721** | **19.051 ± 0.804** |

The bold values express that the proposed method has the best performance.

Table 7: The number of parameters of different models.

| Methods | Number of parameters | Training time/s | Testing time/s |
|---|---|---|---|
| MSCAN | 2,047,409 | 1980 | 7 |
| MSCNN | 1,694,337 | 1838 | 6 |
| Proposed | **765,993** | **1230** | **3** |

the computing cost is reduced and the efficiency is improved.

## 4. Conclusion

Because of the strong learning capability, the CNN is widely used in degradation feature extraction, especially the multiscale CNN which has a stronger representing learning ability. Because of the parallel convolutional pathways, the traditional MSCNN, however, has a large number of parameters, which means a higher computing cost. In addition, a lack of consideration of contribution of different scale of degradation feature makes poor performance of RUL prediction. To address the issue, a pyramid CNN (PCNN) is proposed for RUL prediction of the milling tool is proposed in this paper. In this network, group convolution is used to replace parallel convolutional pathways to extract multiscale features without additional large number of parameters. The channel attention with soft assignment selects the key degradation features not only from different sensors but also from different scales. The proposed method was experimentally validated by the milling tool wear experiment. Some related methods and state-of-the-art models, including machine learning methods and deep learning methods, are analyzed for comparison with the proposed method. The result of it indicates that the proposed method is able to predict the RUL accurately.

Although the proposed method achieves a good RUL prediction result, there are still a few shortcomings in its application. The premise of the application of the proposed method is that the working condition of the testing data is the same as training data, which limits the application in practical engineering because the working condition of the machining process is dynamic. And limited labeled training samples prevents us from training a model for every working condition. To address the issue, a promising work is to introduce transfer learning or meta learning into the model, which can make the model achieve good performance under small samples. Furthermore, this can be combined with some adaptive optimization algorithms to automatically determine the hyperparameters of the model, which can achieve better performance of it.

## Data Availability

The test data used to support the findings of this study are available from the corresponding author upon request.

## Conflicts of Interest

The authors declare that they have no conflicts of interest.

## Acknowledgments

This research was funded by the Key Research and Development Projects in Guangdong Province, grant number 2021B0101220005; Basic Research Program of Guangzhou, grant number 202102080349; industrial internet platform innovation development project of MIIT—New Potential Failure Mode and Effects Analysis System Based on Industrial Internet Platform, grant number TC210804F.

## References

[1] Z. W. Lai, C. Y. Wang, L. J. Zheng et al., "Adaptability of AlTiN-based coated tools with green cutting technologies in sustainable machining of 316L stainless steel," *Tribology International*, vol. 148, Article ID 106300, 2020.

[2] W. Liu, W.-A. Yang, and Y. You, "Three-stage wiener-process-based model for remaining useful life prediction of a cutting tool in high-speed milling," *Sensors*, vol. 22, no. 13, p. 4763, 2022.

[3] Y. Lei, *Intelligent Fault Diagnosis and Remaining Useful Life Prediction of Rotating Machinery*, Elsevier Butterworth-Heinemann, Oxford, Amsterdam, Netherlands, 2016.

[4] C. C. Chen, B. Zhang, and G. Vachtsevanos, "Prediction of machine health condition using neuro-fuzzy and bayesian algorithms," *IEEE Transactions on Instrumentation and Measurement*, vol. 61, no. 2, pp. 297–306, 2012.

[5] P. Ding, M. P. Jia, and X. A. Yan, "Stationary subspaces-vector autoregressive with exogenous terms methodology for degradation trend estimation of rolling and slewing bearings," *Mechanical Systems and Signal Processing*, vol. 150, Article ID 107293, 2021.

[6] P. Park, M. Jung, and P. Di Marco, "Remaining useful life estimation of bearings using data-driven ridge regression," *Applied Sciences*, vol. 10, no. 24, p. 8977, 2020.

[7] M. H. Zhao, B. P. Tang, and Q. Tan, "Bearing remaining useful life estimation based on time-frequency representation and supervised dimensionality reduction," *Measurement*, vol. 86, pp. 41–55, 2016.

[8] X. Liu, Y. X. Jia, Z. W. He, and J. Zhou, "Application of EMD-WVD and particle filter for gearbox fault feature extraction and remaining useful life prediction," *Journal of Vibroengineering*, vol. 19, no. 3, pp. 1793–1808, 2017.

[9] B. Zhang, C. Sconyers, C. Byington, R. Patrick, M. E. Orchard, and G. Vachtsevanos, "A probabilistic fault detection approach: application to bearing fault detection," *IEEE Transactions on Industrial Electronics*, vol. 58, no. 5, pp. 2011–2018, 2011.

[10] N. P. Li, Y. G. Lei, T. Yan, N. B. Li, and T. Y. Han, "A wiener-process-model-based method for remaining useful life prediction considering unit-to-unit variability," *IEEE Transactions on Industrial Electronics*, vol. 66, no. 3, pp. 2092–2101, 2019.

[11] W. B. Chen, W. Z. Chen, H. X. Liu, Y. Q. Wang, C. L. Bi, and Y. Gu, "A RUL prediction method of small sample equipment based on DCNN-BiLSTM and domain adaptation," *Mathematics*, vol. 10, no. 7, p. 1022, 2022.

[12] H. Cheng, X. G. Kong, Q. B. Wang, H. B. Ma, S. K. Yang, and G. G. Chen, "Deep transfer learning based on dynamic domain adaptation for remaining useful life prediction under different working conditions," *Journal of Intelligent Manufacturing*, 2021.

[13] C. Sun, M. Ma, Z. B. Zhao, S. H. Tian, R. Q. Yan, and X. F. Chen, "Deep transfer learning based on sparse autoencoder for remaining useful life prediction of tool in manufacturing," *IEEE Transactions on Industrial Informatics*, vol. 15, no. 4, pp. 2416–2425, 2019.

[14] S. Khan and T. Yairi, "A review on the application of deep learning in system health management," *Mechanical Systems and Signal Processing*, vol. 107, pp. 241–265, 2018.

[15] P. H. Li, X. Z. Liu, and Y. H. Yang, "Remaining useful life prognostics of bearings based on a novel spatial graph-temporal convolution network," *Sensors*, vol. 21, no. 12, p. 4217, 2021.

[16] L. X. Cao, Z. Qian, H. Zareipour et al., "Prediction of remaining useful life of wind turbine bearings under non-stationary operating conditions," *Energies*, vol. 11, no. 12, p. 3318, 2018.

[17] P. Ding and M. P. Jia, "Mechatronics equipment performance degradation assessment using limited and unlabeled data," *IEEE Transactions on Industrial Informatics*, vol. 18, no. 4, pp. 2374–2385, 2022.

[18] H. Cheng, X. G. Kong, G. G. Chen, Q. B. Wang, and R. B. Wang, "Transferable convolutional neural network based remaining useful life prediction of bearing under multiple failure behaviors," *Measurement*, vol. 168, Article ID 108286, 2021.

[19] H. Cheng, X. G. Kong, Q. B. Wang, H. B. Ma, and S. K. Yang, "The Two-Stage RUL Prediction across Operation Conditions Using Deep Transfer Learning and Insufficient Degradation Data," *Reliability Engineering & System Safety*, vol. 225, Article ID 108581, 2022.

[20] P. Ding, M. P. Jia, J. C. Zhuang et al., "Multiobjective evolution enhanced collaborative health monitoring and prognostics: a case study of bearing life test with three-Axis acceleration signals," *IEEE Transactions on Instrumentation and Measurement*, vol. 71, pp. 71–12, 2022.

[21] Y. LeCun, Y. Bengio, and G. Hinton, "Deep learning," *Nature*, vol. 521, no. 7553, pp. 436–444, 2015.

[22] F. Y. Deng, Y. Bi, Y. Q. Liu, and S. P. Yang, "Deep-learning-based remaining useful life prediction based on a multi-scale dilated convolution network," *Mathematics*, vol. 9, no. 23, p. 3035, 2021.

[23] B. Wang, Y. G. Lei, N. P. Li, and T. Yan, "Deep separable convolutional network for remaining useful life prediction of machinery," *Mechanical Systems and Signal Processing*, vol. 134, Article ID 106330, 2019.

[24] A. Z. Hinchi and M. Tkiouat, "Rolling element bearing remaining useful life estimation based on a convolutional long-short-term memory network," *Procedia Computer Science*, vol. 127, pp. 123–132, 2017.

[25] C. Zhang, P. Lim, A. K. Qin, and K. C. Tan, "Multiobjective deep belief networks ensemble for remaining useful life estimation in prognostics," *IEEE Transactions on Neural Networks and Learning Systems*, vol. 28, no. 10, pp. 2306–2318, 2017.

[26] C. Y. Wang, W. L. Jiang, X. K. Yang, and S. Q. Zhang, "RUL prediction of rolling bearings based on a DCAE and CNN," *Applied Sciences*, vol. 11, no. 23, Article ID 11516, 2021.

[27] P. Ding, M. P. Jia, Y. Ding, Y. Cao, X. Zhao, and X. Zhao, "Intelligent machinery health prognostics under variable operation conditions with limited and variable-length data," *Advanced Engineering Informatics*, vol. 53, Article ID 101691, 2022.

[28] P. Ding, M. P. Jia, and X. L. Zhao, "Meta deep learning based rotating machinery health prognostics toward few-shot prognostics," *Applied Soft Computing*, vol. 104, Article ID 107211, 2021.

[29] P. Ding, M. P. Jia, Y. F. Ding, and X. L. Zhao, "Statistical alignment-based metagated recurrent unit for cross-domain machinery degradation trend prognostics using limited data," *IEEE Transactions on Instrumentation and Measurement*, vol. 70, pp. 1–12, 2021.

[30] W. Zhang, X. Li, H. Ma, Z. Luo, and X. Li, "Transfer learning using deep representation regularization in remaining useful life prediction across operating conditions," *Reliability Engineering & System Safety*, vol. 211, Article ID 107556, 2021.

[31] F. Y. Deng, H. Ding, S. P. Yang, and R. J. Hao, "An improved deep residual network with multiscale feature fusion for rotating machinery fault diagnosis," *Measurement Science and Technology*, vol. 32, no. 2, Article ID 024002, 2021.

[32] X. Li, W. Zhang, H. Ma, Z. Luo, and X. Li, "Degradation alignment in remaining useful life prediction using deep cycle-consistent learning," *IEEE Transactions on Neural Networks and Learning Systems*, vol. 33, no. 10, pp. 5480–5491, 2022.

[33] H. Cheng, X. G. Kong, Q. B. Wang, H. B. Ma, and S. K. Yang, "The Two-Stage Rul Prediction across Operation Conditions Using Deep Transfer Learning and Insufficient Degradation Data," *Reliability Engineering & System Safety*, vol. 225, 2022.

[34] D. Z. Wu, C. Jennings, J. Terpenny, R. X. Gao, and S. Kumara, "A comparative study on machine learning algorithms for smart manufacturing: tool wear prediction using random forests," *Journal of Manufacturing Science and Engineering*, vol. 139, no. 7, 2017.

[35] X. Li, Q. Ding, and J. Q. Sun, "Remaining useful life estimation in prognostics using deep convolution neural networks," *Reliability Engineering & System Safety*, vol. 172, pp. 1–11, 2018.

[36] Y. T. Li, Q. S. Xie, H. S. Huang, and Q. P. Chen, "Research on a tool wear monitoring algorithm based on residual dense network," *Symmetry*, vol. 11, no. 6, p. 809, 2019.

[37] H. Li, W. Zhao, Y. X. Zhang, and E. Zio, "Remaining useful life prediction using multi-scale deep convolutional neural network," *Applied Soft Computing*, vol. 89, Article ID 106113, 2020.

[38] Y. X. Chen, Y. Jin, and G. Jiri, "Predicting tool wear with multi-sensor data using deep belief networks," *International Journal of Advanced Manufacturing Technology*, vol. 99, no. 5-8, pp. 1917–1926, 2018.

[39] B. A. Wang, Y. G. Lei, N. P. Li, and W. T. Wang, "Multiscale convolutional attention network for predicting remaining useful life of machinery," *IEEE Transactions on Industrial Electronics*, vol. 68, no. 8, pp. 7496–7504, 2021.

Hindawi
Shock and Vibration
Volume 2022, Article ID 4059824, 14 pages
https://doi.org/10.1155/2022/4059824

*Research Article*

# A New Dynamic Balance Framework Based on Blind Source Separation under Multiple Fault Conditions

**Bo Lang,[1] Xinyi Zhang,[1] Jun Xiao,[2] Shouhang Lu,[3] and Bing Li[4,5]**

[1]*School of Mechanical Engineering, Xi'an Jiaotong University, Xi'an, Shaanxi 710049, China*
[2]*State Key Laboratory of Compressor Technology (Anhui Laboratory of Compressor Technology), Hefei, Anhui 230031, China*
[3]*Xi'an Shaangu Engineering and Technology Co., Ltd, Xi'an, Shaanxi 710075, China*
[4]*School of Mechano-Electronic Engineering Xidian University, Xi'an, Shaanxi 710071, China*
[5]*Xi'an Key Laboratory of Intelligent Instrument and Packaging Test, Xidian University, Xi'an, Shaanxi 710071, China*

Correspondence should be addressed to Bing Li; libing@xidian.edu.cn

Received 17 June 2022; Revised 8 August 2022; Accepted 9 August 2022; Published 29 September 2022

Academic Editor: Liu Jing



Accordingly, the mass unbalance of the rotors is usually the major cause of excessive vibration. The information extracted at the fundamental frequency is often employed to fix the unbalance issue. However, other rotor faults like rotor bending and bearing-failure effect also generate additional components to the characteristics. Thus, it is necessary to isolate the corresponding features and obtain the intrinsic causes of the multiple failures. In this paper, a productive hybrid method is successfully developed to deal with the root mass unbalance problem with additional force interference by integrating the superiority of different methods, including Ensemble Empirical Mode Decomposition (EEMD) and Nonnegative Matrix Factorization (NMF), where EEMD is used to obtain sensitive IMFs and NMF is employed to acquire the inherent source signal, respectively. Meanwhile, a root dynamic balancing and implemental framework is also developed to accomplish the task of vibration reduction. For verification, a serial of simulations and experimental investigations have been analysed to demonstrate the preferable potentialities of the proposed method. In particular, a standard Bently Nevada rotor rig with a specifically designed device was employed to simulate appended faults by adjusting the additional forces during the experimental steps. The analysis results show that the proposed method can isolate and extract the unbalance faults from the raw vibration signals and achieve accurate correction balancers, where a nearly identical correction angle has been achieved, which indicates that the optimal installation position has been successfully figured out.

## 1. Introduction

As one of the most vital apparatuses, rotating machinery of great significance in defensive and civil fields is the fundamental infrastructure and key to national economic production equipment. Unfortunately, these oscillatory systems are easily susceptible to unwanted vibrations, where some negatives and factors like excessive vibration, structural noise, and thermal deformation will be generated and significantly enhanced with the increase of rotational speed [1–4].

In reality, a rotor system may suffer from different types of failures during long-term operating. The most common causes including unbalance, misalignment, fatigue crack, thermal deformation, rotor-stator friction, and benting may further induce sudden breakdowns and make undesired vibrations arise during operation [3–5]. Among the abovementioned causes, unbalance failures represent 35% of the mechanical problems of rotating machines and account for more than 75% of the rotating machine vibration fault [1, 6, 7]. Therefore, it is critical and reasonable to investigate effective and reliable techniques to eradicate this issue and further achieve reliable operation.

In addition, it is cumbersome to fix the mass unbalance issue under multifault condition, in which another aspect of the rotor system vibration behaviour can also be traced to

initial deformations like rotor bending and contact friction. In particular, the coupling misalignment and the thermal bowing can also change the unbalance distribution [8]. Once the preliminary deformation of a rotor shaft couples with the unbalance issue, the synchronous vibration response, which only differs from the mass unbalance, can be extracted [9]. In this case, the characteristics extracted from analysis sources like vibration and acoustics become ambiguous and unintuitive. Thus, to identify and isolate the inherent features that directly reflect the rotor faults and achieve reliable maintenance strategies and practical operations, more effective and in-depth investigations should be established to address the above issues.

Nowadays, lots of literature has accumulated and documented many investigations on rotor systems such as base motion, vibration resonance, friction, and contact [10]. In particular, in situ rotor balancing has attracted considerable attention from industry and academia [3, 11–13]. Meanwhile, the research and development on the efficient dynamic balancing method have been treated as a decisive technology for fault recovery and vibration reduction [10]. Specifically, representative methods used to address the rotor unbalance issue involve the influence coefficient method (ICM), modal balancing, Holo-balancing, and autobalancing [2, 10, 14–17]. As a data-driven method, ICM that only requires machine runs with trial weights can be simply implemented without any prior knowledge of the rotor model. ICM has been widely employed and intensively applied in the industry and experimental environment, and the corresponding theory and applications are matured after years of development and refinement [15]. On the other hand, if the full-model parameters of the rotor system are known in advance, the modal balancing method can be highly competent to account for rotor unbalance using the modal shapes. In this method, the intrinsic mechanism relies heavily on adding trial weights to N balance surfaces to counteract the corresponding N modal unbalance responses [10, 15]. Generally, to achieve a satisfactory result using modal balancing, one should rely on an accurate numerical model and prior knowledge of the entire rotor dynamics or a highly skilled engineer. As for the Automatic Ball Balancer (ABB), it can be used to reduce rotor vibrations by compensating for mass unbalance of the rotor. This method is better adapted to applications where the amount of imbalance varies with the operating conditions. However, due to its inherent nonlinear properties, on some occasions, especially during the run-up and shutdown stage, ABB may enhance the original vibration level rather than eliminating the vibration response [17]. Owing to the advantages of easy implementation and high efficiency, ICM has become the most commonly used balancing method in industries.

In general, the vibration frequencies of the rotor imbalance are synchronous, i.e., one times the shaft rotational speed (1X rpm), and the imbalance forces cause the shaft rotation frequency (1X) dominating its harmonic frequencies [18]. The core issue of the dynamic balancing procedure is to precisely extract the 1X frequency components from the raw vibration signal. However, it could be a daunting task to obtain the pure unbalance components of 1X, especially for multiple faults, since other rotor failures such as cracks, bends, looseness problems, and misalignments also introduce disturbances to the balancing characteristics of the rotor system [2, 3, 19]. That is, the evidence 1X commonly calculated from the original signal should be treated as the superposition of different frequency responses that are closely associated with the external forces generated by the rotor failure. In field operations, however, many technicians indiscriminately use the mixed amplitude and phase information at 1X to handle the mass unbalance without considering the superposition of unbalance and other rotor faults. Sometimes, promised results may be achieved with the entire vibration level decreasing to the allowable range or even better. However, vibration symptoms may reappear or even increase within a short period of time once the fault coupling force changes, i.e., oil-film force and blade force. The reason for the phenomenon is briefly induced by the root cause misjudgment. Thus, fault coupling and isolation procedures should be on the agenda and systematically investigated to reach the root response characteristics and further improve the maintenance effect.

In this paper, we focus on identifying the inherent unbalance parameters of the rotor system using blind source separation (BSS) and Ensemble Empirical Mode Decomposition under multiple fault conditions. The two signal processing methods are introduced in Section 2. As a representative and prevalent BSS technique, Nonnegative Matrix Factorization (NMF) is delivered to accomplish the fault isolation task. EEMD is employed to calculate the most valuable intrinsic mode functions (IMFs). Thereafter, the fundamental principle of ICM is described and the main framework of the proposed method is illustrated. The effectiveness of the new method is verified using different simulations and experiments, and some relevant discussions are presented in the next section. Finally, some conclusions are presented in the last section.

## 2. Basic Concepts of the Involved Signal Processing Approaches

To figure out the root response that corresponds to the inherent fault, in the current section, a new fusion approach is established by combining Ensemble Empirical Mode Decomposition (EEMD) with Nonnegative Matrix Factorization (NMF) to accomplish the ultimate target of inherent unbalance extraction. The principles of the two methods are briefly introduced. Thereafter, the core framework is given.

*2.1. Nonnegative Matrix Factorization.* Blind source separation (BSS) is widely used to extract underlying information from a mixture of different behaviours, i.e., multifault response and mixed sound signals. The main task of BSS for signal decomposition relies on inferring and estimating the most probable sources[20], i.e., fault signals and speech components from the acquired signals. The ideal model of BSS can be formulated as

$$\mathbf{X}(t) = \mathbf{A}\mathbf{S}(t) + \mathbf{E}, \tag{1}$$

where $\mathbf{X}(\mathbf{t}) \in \mathbf{R}^{P\times N}$ is the so-called observed matrix that can be expressed as $[x_1(t), x_2(t)\cdots x_P(t)]^T$;$\mathbf{S}(\mathbf{t}) \in \mathbf{R}^{n\times N}$ is the separated matrix that consists of unknown source signals, i.e., $\mathbf{S}(\mathbf{t}) = [s_1(t), s_2(t), \cdots s_n(t)]^T$; $\mathbf{A} \in \mathbf{R}^{P\times n}$stands for the mixing matrix and $\mathbf{E} \in \mathbf{R}^{P\times N}$ denotes the additive Gaussian noise with zero mean.

Unlike most BSS algorithms that learn holistic representations, e.g., independent component analysis (ICA), principal component analysis (PCA), and sparse component analysis (SCA), Nonnegative Matrix Factorization (NMF) only learns partial features with nonnegative constraints to better decompose the objective matrix. The output of NMF is to figure out an approximate factorization into two nonnegative factors. Since NMF was first proposed by Lee and Seung in nature, it has attracted widespread interest at the intersection of many scientific and engineering disciplines, such as face recognition, blind source separation, speech enhancement, fault diagnosis, pattern recognition, and data mining [21, 22].

Given a matrix $\mathbf{V}$ with nonnegative observations$v_{ij}$, NMF is used to factorize matrix $\mathbf{V}$ into two main parts: the basis matrix $\mathbf{W}$and component matrix.

$$\begin{aligned}&\mathbf{V} \approx \mathbf{WH}\\ &s.t.\ v_{ij} \geq 0,\ w_{ik} \geq 0,\ h_{kj} \geq 0, i = 1, \ldots, n; j = 1, \ldots m; k = 1, \ldots, r\end{aligned}, \tag{2}$$

where $\mathbf{V} \in \mathbf{R}^{n\times m}$ is a nonnegative mixed matrix constructed and formed from vibration vectors, $\mathbf{W} \in \mathbf{R}^{n\times k}$ is the basis matrix that is considered as a set of basis vectors, and $H \in R^{k\times m}$ is so-called coefficient matrix (or component matrix) that is treated as the coordinates of each sample with respect to these basis vectors [22, 23].

To accomplish the factorization of $\mathbf{V} \approx \mathbf{WH}$ as accurately as possible, a robust and effective objective function should be designed to quantify the approximation quality. Herein, the commonly used squared error (Euclidean distance) function and the Kullback–Leibler divergence are introduced as the objective functions for factorization.

The objective function of NMF is formulated by the Euclidean distance; namely,

$$\begin{aligned}&D(\mathbf{V}\|\mathbf{W}, \mathbf{H}) = \|\mathbf{V} - \mathbf{WH}\|^2 = \sum_{i,j}\left[v_{ij} - (\mathbf{WH})_{i,j}\right]^2\\ &s.t.\ \mathbf{W}_{ia} \geq 0, \mathbf{H}_{bj} \geq 0, \forall a, b, i, j\end{aligned}, \tag{3}$$

where $D(\mathbf{V}\|\mathbf{W}, \mathbf{H})$ stands for the distance between the data matrix and the two factorized matrixes.

Correspondingly, the objective function constructed in terms of Kullback–Leibler divergence is given as follows:

$$\begin{aligned}&minD(\mathbf{V}\|\mathbf{W}, \mathbf{H}) = \sum_{i,j}\left\{v_{ij}\left[\log\left(\frac{v_{ij}}{(\mathbf{WH})_{ij}}\right) - 1\right] + (\mathbf{WH})_{i,j}\right\}\\ &s.t.\ \mathbf{W}_{ia} \geq 0, \mathbf{H}_{bj} \geq 0, \forall a, b, i, j\end{aligned}. \tag{4}$$

As can be noticed in (4), the core values of NMF can be recognized as the optimal linear combination using the basis matrix to approximately recover the original data matrix. The objective function of the NMF optimization model based on Euclidean distance is a bit simpler to implement and achieve good performance.

Theoretically, it is scarcely possible to find the global minima of the objective function, since the convexification of the two terms $(\mathbf{W}, \mathbf{H})$ together could be a long-beleaguered task. To minimize the cost function, Lee and Seung presented efficient multiplicative elementwise update formulae for these two minimization problems and proved their convergence [22, 23].

The alternation and iterative operations are utilized for matrix updating, i.e., the nth updated result $\mathbf{W}^{(\mathbf{n})}$ is fixed and employed for the further renewable process on $\mathbf{H}^{(\mathbf{n+1})}$. Thereafter, a new iterative result $\mathbf{W}^{(\mathbf{n+1})}$ can be calculated using the unvaried item $\mathbf{H}^{(\mathbf{n+1})}$. The regeneration formulae for the Euclidean distance are written as

$$\begin{cases} w_{ik} \leftarrow w_{ik}\dfrac{\left(\mathbf{VH}^T\right)_{ik}}{\left(\mathbf{WHH}^T\right)_{ik}} \\ h_{kj} \leftarrow h_{kj}\dfrac{\left(\mathbf{W}^T\mathbf{V}\right)_{kj}}{\left(\mathbf{W}^T\mathbf{WH}\right)_{kj}} \end{cases}. \tag{5}$$

For the Kullback–Leibler divergence model, the corresponding updated role is

$$\begin{cases} w_{ik} \leftarrow w_{ik}\dfrac{\sum_j h_{kj}v_{ij}/(\mathbf{WH})_{ij}}{\sum_u h_{ku}} \\ h_{kj} \leftarrow h_{kj}\dfrac{\sum_i h_{ik}v_{ij}/(\mathbf{WH})_{ij}}{\sum_v h_{vk}} \end{cases}. \tag{6}$$

The steady states of the two matrices $\mathbf{W}$ and $\mathbf{H}$ can be achieved and the iteration is terminated when the iteration number of NMF algorithm reaches its threshold. More details can be found in [21, 23].

For source separation or dimension reduction, the number of rows $r$ is supposed to satisfy the inequality$r(m + n) < mn$. Note that the key parameter $r$ is related to the expected number of faults in the rotor system in our following application.

*2.2. Ensemble Empirical Mode Decomposition.* Empirical Mode Decomposition (EMD) method has attracted considerable attention and has been widely investigated in the

fields of condition monitoring and fault diagnosis. EMD-based research and application have become an important branch for handling nonlinear and nonstationary data. This technique can decompose the analysis signal into a serial of intrinsic mode functions (IMFs) or monocomponent functions. Meanwhile, each IMF satisfies the following prerequisites and definitions [24–26].

Firstly, in the whole data set, the number of extrema and the number of zero-crossings must be equal or differ by at most one.

Secondly, at any point, the mean value of the envelope defined by the local maxima and the envelope defined by the local minima must be equal to zero.

Through the standard procedure, the final decomposition result can be gained accordingly.

$$\mathbf{Y}(t) = \sum_{i=1}^{n} \mathbf{c}_i(t) + \mathbf{r}_n(t). \tag{7}$$

According to the theory of EMD, the relevant center frequency for each IMF component gradually reduces, where the first IMF owns the highest frequency bandwidth while the last IMF is associated with the low-frequency components. Conventionally, for the sake of fault diagnosis, the usual practice relies on the features extraction from the first few IMFs since localized fault characteristics are usually displayed in the high-frequency bands. However, as for further information utilization, different IMF components have abilities in which the discarded low-frequency IMFs may contain beneficial effects that can be further utilized to treat other applications.

EMD also suffers from several inherent drawbacks, i.e., the choice of a relevant stopping criterion, mode-mixing problem. Mode-mixing that can be arbitrarily split into two groups, including oscillations of dramatically disparate scales and similarly scaled components residing in different IMFs, is the major drawback of EMD, sometimes causing severe aliasing or inducing unpredictable and inexplicable results.

By means of adding a finite white noise to the raw signal, EEMD was successfully developed to improve the EMD algorithm [26, 27]. It can be seen that EEMD is a noise-assisted data analysis method. Here, the two parameters, the ensemble number and the noise level, play an important role in determining the decomposition effect. Some background theories and applications can be found in [25, 27]. The corresponding flow of EEMD can be briefly listed as follows.

Step1 Collect the original noise signal $\mathbf{Z}(t)$ from the experiment platform or field industry.

Step2 Set the initial parameters of the noise components and the number of ensemble$M$.

Step3 Construct loops for each IMF extraction and perform $M$ times of standard EMD steps for the signal with white noise while the loop is repeated.

Step4 Calculate the ensemble average of $M$ trials to obtain the related IMFs during this loop.

Step5 Compute the residual$R_m(t) = \mathbf{Z}(t) - IMF_i(t)$.

Step6 Consider the residual signal as the original signal and repeat the whole process until a constant residual is achieved.

If necessary, it is suggested for the reader to view [25] for more details of EEMD algorithm.

*2.3. Brief Summary of Rotor Balancing.* The influence coefficient, which can reflect the linear relationship between the trial weight and characteristics, is relevant to the sensor/balancer position and the rotating speed (see Figure 1).

Once the trial weight is installed into the correction plane, the characteristic response of 1X from the output end is obtained. The influence coefficient in Figure 1 briefly relies on two assumptions: (1) the rotor synchronous response is proportional to the imbalance; (2) the effects of individual imbalances can be superimposed to obtain the effect of a set of imbalances [19, 28].

The general formulation of the influence coefficient method is

$$\mathbf{V} = \mathbf{V_0} + \mathbf{PD}, \tag{8}$$

where $\mathbf{V} \in \mathbf{C}^{r\times 1}$ is the complex vector representing the rotor synchronous vibration (1X) measured at $r$ locations, $\mathbf{V_0} \in \mathbf{C}^{r\times 1}$ denotes the synchronous vibration at the $r$ sensor position caused by the system inherent imbalance, $\mathbf{P} \in \mathbf{C}^{r\times s}$ is the influence coefficients matrix, and $\mathbf{D} \in \mathbf{C}^{s\times 1}$ is the imbalance weight provided by the balancer in the balancer coordinate system.

The matrix $\mathbf{P}$ can be obtained after a series of trial runs. Assume that the vibration characteristic is $V_i$ when the imbalance of the balancer $D_i$ is installed into the correction plane. Then, the influence coefficient is estimated using (2)

$$P^{ij} = \frac{V_1^i - V_2^i}{D_1^j - D_2^j}, \tag{9}$$

where $P^{ij}$ is the $ij$th element of $\mathbf{P}$, $V^i$ represents the vibration at the $i$th measurement location, and $D^j$ is the imbalance provided by the $j$th balancer.

The optimal imbalance weights can be obtained using the least squares solution:

$$\mathbf{D} = -\left(\mathbf{P}^{\mathbf{T}}\mathbf{P}\right)^{-1}\mathbf{P}^{\mathbf{T}}\mathbf{V_0}. \tag{10}$$

For more detailed information about ICM, the readers can be referred to [19, 28].

*2.4. The Proposed Procedure for Dynamic Rotor Balance.* With the assistance of NMF and EEMD, a hybrid method named BSS-ICM is developed to accomplish the multiple fault identification and isolation tasks. Meanwhile, a root dynamic balancing and implemental framework is also proposed to realize vibration reduction, in which the main goal is to find the root inherent balancing causes and to further operate with safety, stability, and long-term runnings.

The sketch of the proposed main framework can be seen in Figure 2.

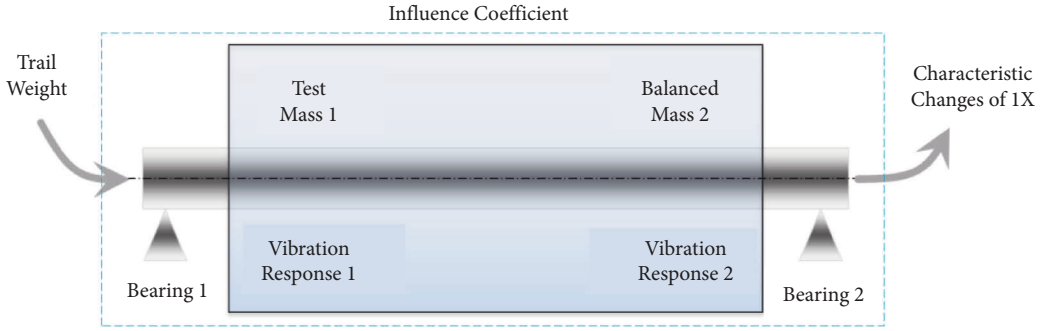


Figure 1: The influence coefficient calculation model.

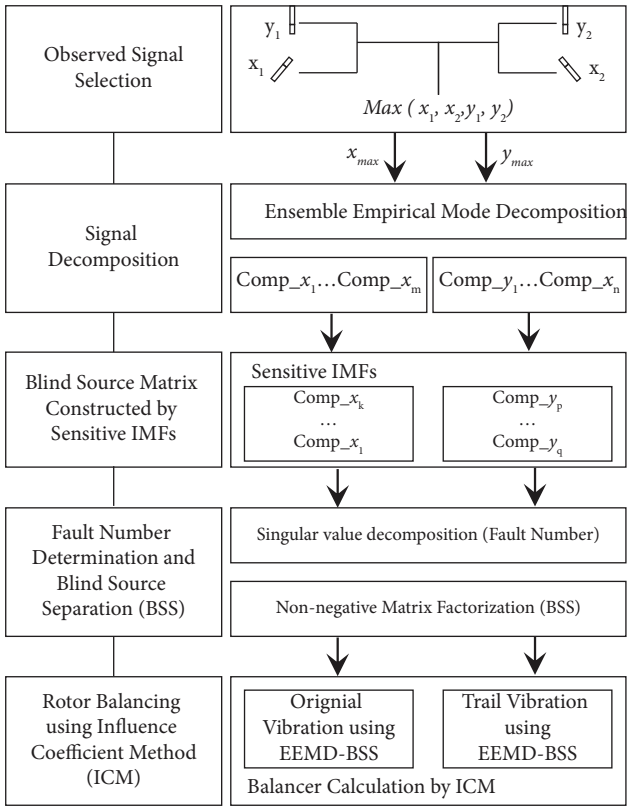


Figure 2: The framework of BSS-ICM.

As can be viewed in Figure 2, the new method mainly consists of five portions, i.e., observed signal selection, signal decomposition, blind source matrix construction, fault number determination, blind source separation, and ICM-based rotor balancing.

(1) Signal collection and analysis source selection: the observed signal is simultaneously collected by the acquisition system and selected for further analysis according to the magnitude level. Note that the comparison must be applied to signals of the same direction.

(2) Signal decomposition: EEMD is utilized to decompose each selected signal into a serial of IMFs. Sensitive IMFs are identified according to the similarity between the extracted IMF and the original signal. The basic idea of IMF selection relies on the use of representative IMFs to replace the raw signal for precise balancing calculation.

Herein, the cosine similarity measure metric is involved in enhancing the effectiveness and automation of IMF selection. This metric is originally defined as the inner product of two vectors $\mathbf{X} = [x_1, x_2, \ldots, x_N]$ and $\mathbf{Y} = [y_1, y_2, \ldots, y_N]$ divided by the product of their lengths [24], which can be written as

$$\mathrm{Sim}_{\cos}(\mathbf{X}, \mathbf{Y}) = \cos(\alpha) = \frac{\left|\sum_{k=1}^{N} x_k y_k\right|}{\sqrt{\sum_{k=1}^{N} x_k^2} \times \sum_{k=1}^{N} y_k^2}. \quad (11)$$

Note that the symbol $\alpha$ in (11) represents the included angle between the two vectors. Herein, we a little more focus on the cosine similarities than the angle itself. It can be observed that the magnitude range of the similarity starts from [0, 1], where the more extensive the cosine value is, the higher the similar degree of two vectors would be and vice versa.

(3) Blind source matrix construction: the source matrix is constructed using the sensitive IMFs. The popular Singular Value Decomposition (SVD) is employed to calculate the fault number in the rotor system. Number estimation is considered as a crucial step in most BSS circumstances. The main principle behind this strategy is that the dominant and nondominant singular values obtained by SVD correspond to the faulty and normal component, respectively. Thus, the largest decline ratio of adjacent eigenvalues can be delivered as a criterion to distinguish the faults from normal (or noise).

(4) Nonnegative matrix factorization is utilized to decompose the source matrix to acquire the inherent source signal.

(5) Depending on the signal characteristics, fault diagnosis and isolation results can be demonstrated from

the inherent source signal. Signals with dominated amplitudes at 1X and very small amplitudes at other harmonics will be treated as the vibration responses related to the mass unbalance failure.

(6) ICM is introduced to accomplish the balancing task once the original and the trial signals are processed using the above steps.

## 3. Case Studies for Performance Verification

To evaluate the performance of the proposed approach, in this section, different verifications using simulations and experiments have been concerned and demonstrated by means of BSS-ICM. Note that all simulations and experiments were performed on a computer with the Intel Core i7-8565u@1.80 GHz 1.99 GHz and 16.0 GB (15.7 GB usable) memory by 64 bit MATLAB 2010b on Windows 10.

*3.1. The Main Comparison Flowchart.* To make a systematic comparison, three groups of analyses are involved in this section. The main comparison flowchart is shown in Figure 3. For illustration purposes, the studies related to these three groups are named case 1 (conventional ICM without other faults), case 2 (conventional ICM with additional force), and case 3 (BSS-ICM with additional force).

According to Figure 3, some important descriptions are briefly given.

(1) Conventional ICM is employed to address the rotor balancing issue under different conditions, i.e., with and without other failures. In this case, the balancing parameters calculation of the rotor system without other faults is regarded as the reference.

(2) Without regard to the distinction between the two methods (conventional ICM and BSS-ICM), the whole signal comparison process is quite similar, using the same signals and obtained results with the same patterns.

(3) Since it is quite difficult to simulate the whole process of rotor balancing, the final step in Subsection 3.3 using ICM is abruptly neglected in the simulation case. Analysis results from the first five steps of BSS-ICM will be used to validate the operating performance in this case.

(4) For a common and united comparison, the simulation and experimental parameters are identically designed (see Table 1).

Note that, due to the space restraint, the rotor system without fault using BSS-ICM is ignored in the experimental case in Section 3.3.

*3.2. Numerical Simulations and Discussions.* In this section, numerical simulation is introduced to verify the performance of the proposed algorithm. The effectiveness of BSS-ICM is validated by comparing the extraction results with the simulated sinusoidal signal that only contains one frequency component. The single frequency signal herein denotes the vibration response generated by the mass unbalance.

The two-fault candidate can be considered as one of the most prevalent and representative multiple fault patterns in industrial applications, and multiple faults with more than two sources rarely occur due to periodical maintenance and scientific management. Thus, the mixed signal containing two sources is employed to highlight the prominent properties of our method.

Let $\mathbf{Q}$ be the observed matrix composed of a white noise term $v_i(t)$ and a superposition of two sources, i.e., $S_1(t)$ and $S_2(t)$. The source and mixed signals are defined as follows, respectively:

$$\begin{cases} s_1(t) = d_1 \sin\left(2\pi f_1 t + \varphi_1\right) + v_1(t) \\ \\ s_2(t) = d_2\left[1 + \sin\left(2\pi f_1 t + \varphi_2\right)\right]\sin\left(2\pi f_2 t + \varphi_4\right) + v_2(t)' \end{cases} \tag{12}$$

$$\mathbf{Q} = \begin{bmatrix} Q_1(t) \\ Q_2(t) \end{bmatrix} = \mathbf{AS} = \begin{bmatrix} a_{11} & a_{12} \\ a_{21} & a_{22} \end{bmatrix}\begin{bmatrix} s_1(t) \\ s_2(t) \end{bmatrix}, \tag{13}$$

where the corresponding parameters are illustrated in Table 2.

During the simulating process, the mixing matrix $\mathbf{A}$ is artificially designed as

$$\mathbf{A} = \begin{bmatrix} a_{11} & a_{12} \\ a_{21} & a_{22} \end{bmatrix} = \begin{bmatrix} 0.8 & 0.6 \\ -0.7 & 0.1 \end{bmatrix}. \tag{14}$$

The signal is generated over a time of 0.5 s with a sample frequency of 1 kHz. Figure 4 gives two time curves of the observed signals $Q_1(t)$ and $Q_2(t)$. EEMD results related to $Q_1(t)$ are shown in Figure 5.

Meanwhile, the cosine similarities between each IMF and the observed signals are obtained by (11) and listed in Tables 3 and 4, respectively. The IMF with the most prominent similarity is selected to achieve the source separation task, while the others are discarded as irrelevant components. Here, IMF3 and IMF2 are, respectively, selected and utilized for further analysis as they own the highest similarities compared to the others in each table.

By comparing the observed signal in Figure 4(b) with its IMFs in Figure 5, significant evidence can be automatically obtained and visually distinguished.

Thereafter, SVD is delivered to estimate the source number and the first 20 decline ratios are plotted in Figure 6.

It can be noticed that the highest value of the decline ratio shows up at the second position, which means that the source number is equal to two accordingly.

Thereafter, the observed matrix and the selected IMFs are treated as the new observed matrix and processed using the NMF method to carry out the inherent sources. Furthermore, to reflect the original sources $\mathbf{S}$, i.e., $s_1(t)$ and $s_2(t)$, the extracted sources are estimated by the characteristics of frequency distribution. For better comparison, the corresponding components for the same pattern are intensively drawn in the single chart in Figure 7.

At first glance, analogous properties appear in each chart in Figure 7, especially the phase information, where nearly identical results have been achieved. On closer inspection, a

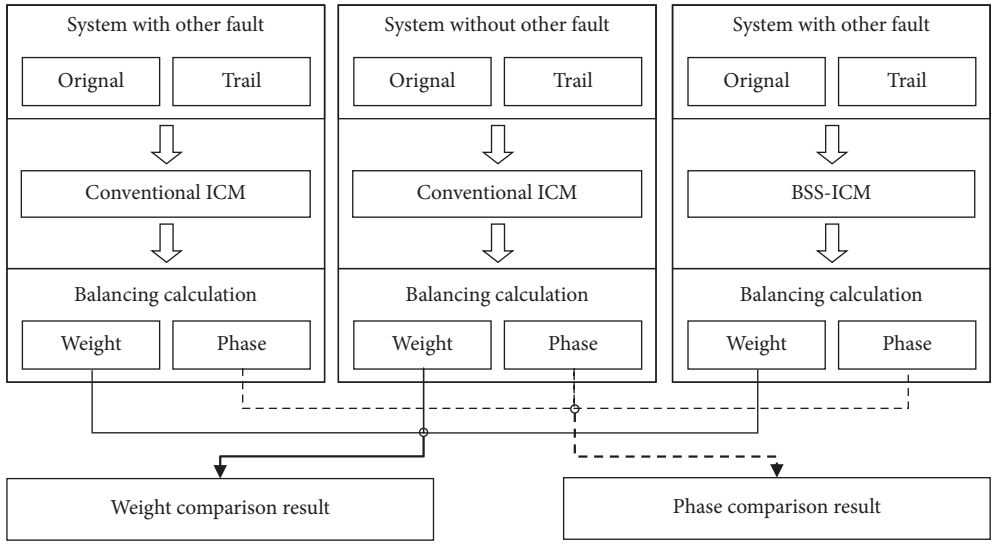


Figure 3: The main comparison flowchart using the proposed method.

Table 1: Same parameters used for simulation and experiment cases.

| Parameters | Source number | Sensitive IMFs number | Ensemble number | Noise level | Max iterative | Residual threshold |
|---|---|---|---|---|---|---|
| Values | 2 | 2 | 100 | 0.1 | 10000 | 1e-5 |

Table 2: Some parameters of the mixed signal in (12).

| Parameters/units | $d_1/\mu m$ | $f_1$/Hz | $\varphi_1$/rad | $d_2/\mu m$ | $\varphi_2$/rad | $f_2$/Hz | $\varphi_3$/rad | $\upsilon_i(t)$ |
|---|---|---|---|---|---|---|---|---|
| Values | 20 | 20 | $\pi/3$ | 15 | $\pi/4$ | 40 | $\pi/2$ | 10 dB |

slight difference can be noticed between these two charts. In Figure 7(a), for the simulated mass unbalance components, the estimated amplitudes coincide precisely with each other, and a tiny phase shift phenomenon shows up. In Figure 7(b), the fluctuation has increased between the theoretical and the estimated sources. However, the phase shift seems disappeared compared to the previous case. Note that the difference between the theoretical and estimated sources in each case is so slight that the spectrum calculation and analysis are negligible considering the space limitation.

It can be inferred from the above discussions that the extracted information corresponding to the "mass unbalance" obtained by the proposed method is perfectly reserved and can be representatively used for further unbalancing calculations.

### 3.3. Experimental Results and Discussions

*3.3.1. Experiment Setup.* To verify the rotor balancing performance in practice, a series of experiments are developed under different external forces. Note that multiple faults are simulated using a specifically designed Bently Nevada Rotor Kit (see Figure 8).

Figure 8 illustrates the structure chart of the rotor balancing test rig together with the specific loading structure. As can be observed, the whole rig consists of a speed controller, a DC motor, a serial of standard weights, and a small range electric balance. A NI-4432 data acquisition card was used for the vibration signal collection. Moreover, six eddy current displacement probes perpendicular to each other were installed separately and further used to perform the task of vibration information capture (see Figure 8(a)). The other two probes were employed for speed measurement and control. More details of the rig can be found in [19].

It needs to be emphasized that the specific loading device installed is used to simulate additional failures like pipeline excitation, which directly affect the distribution of the radial forces by the four linked springs (see B-direction in Figure 8(a)). The current device is able to generate different levels of external forces in terms of the four round nuts. Theoretically, it is capable of loading radial forces in any direction on the rotating components. Since the force applied to the spring is proportional to the spring deformation, the change of the deformation can be quantified and transformed into the changes of pitch number. Thus, the pitch number directly substitutes the real force for convenience.

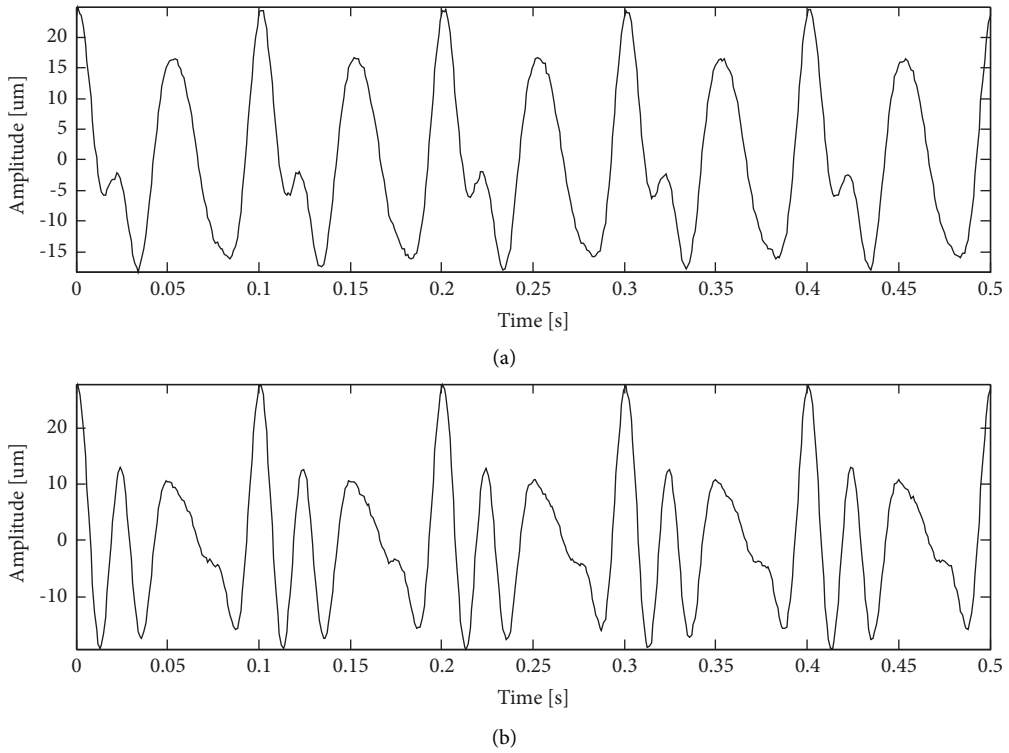


Figure 4: Time curves corresponding to the two observed signals.

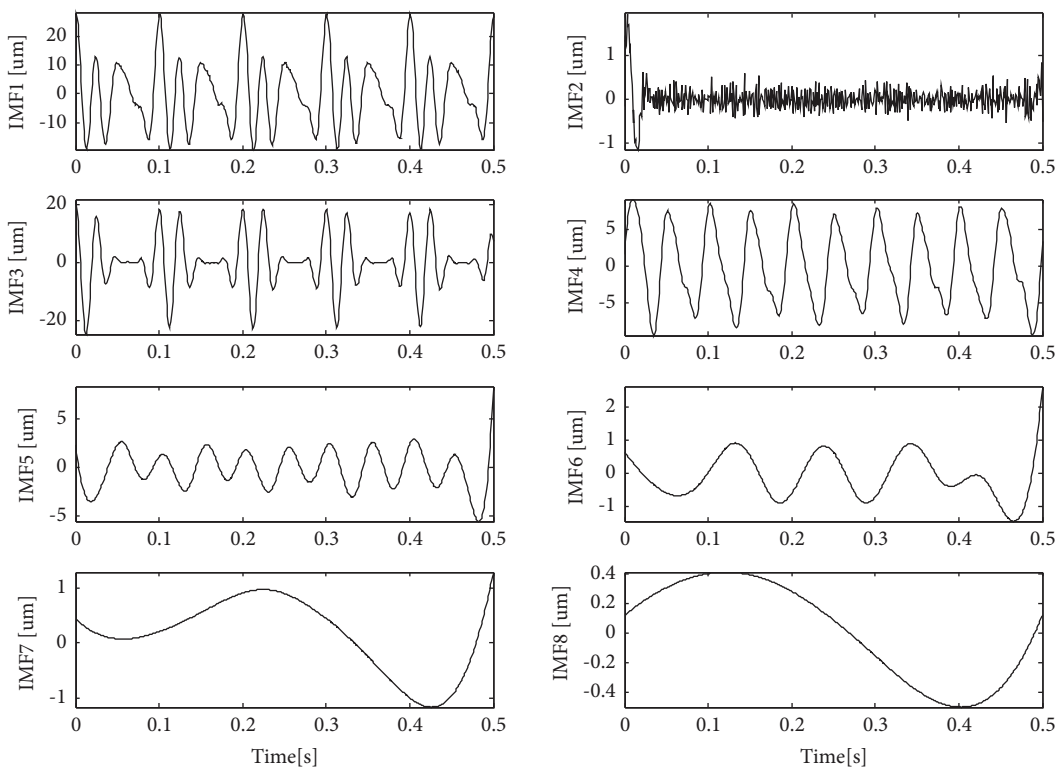


Figure 5: EEMD results of the observed signal in Figure 4(b).

Meanwhile, the four directions of top, down, left, and right were represented by four capital letters *T*, D, *L*, and *R*, respectively. The numbers are attached to the capital letters to represent the force vectors (magnitude and direction). For example, L2T3 means two forces of 2 pitches and 3 pitches simultaneously applied to the left and top directions.

Table 3: Cosine similarities between each IMF and the mixed signal in Figure 4(a).

| IMF | 1 | 2 | 3 | 4 | 5 | 6 | 7 | 8 |
|---|---|---|---|---|---|---|---|---|
| $Sim_{cos}$ | 0.012 | 0.091 | 0.860 | 0.646 | 0.104 | 0.056 | 0.019 | 0.020 |

Table 4: Cosine similarities between each IMF and the mixed signal in Figure 4(b).

| IMF | 1 | 2 | 3 | 4 | 5 | 6 | 7 | 8 |
|---|---|---|---|---|---|---|---|---|
| $Sim_{cos}$ | 0.215 | 0.983 | 0.183 | 0.110 | 0.044 | 0.015 | 0.004 | 0.014 |

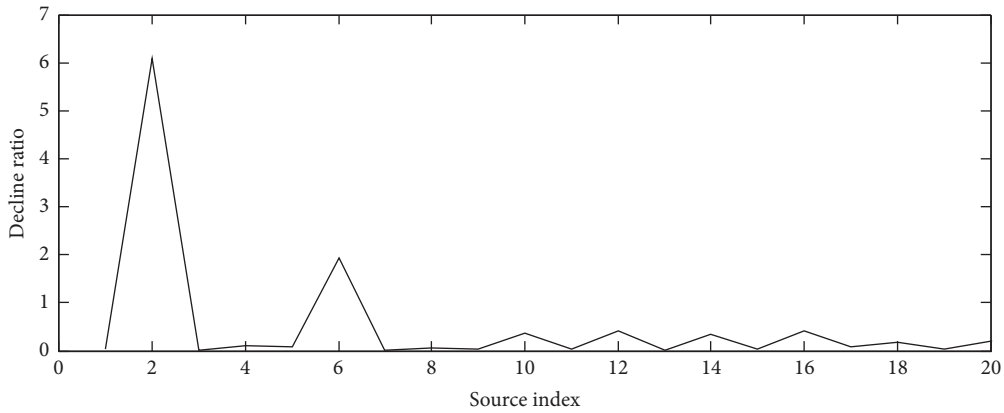


Figure 6: Changes of decline ratio with source index.

Note that, for comparison, all operating conditions, including the data collection parameters, are identical. The input rotating speed of the DC motor was approximately equal to 1000 rpm. Vibration signals were collected simultaneously using five probes. Each file of the vibration signal consisted of 2 s of data at a sampling rate of 4096 Hz. The order tracking technique was also involved in gaining vibration parameters as precisely as possible when the procedure was used to process vibration signals. Meanwhile, because rotor balancing essentially requires the phase measurement of the synchronous harmonics of the vibration signal with respect to a reference, the key phasor (one of the probes fixed near the motor) was adopted to provide the reference phase angle value associated with the filtered amplitudes measured by each transducer.

*3.3.2. The Standard Rotor Balance Process.* The standard rotor balance process without additional radial force was first introduced to obtain the reference parameters, such as mass unbalance vector and balancing vector corresponding to the original imbalance.

First, the peak-to-peak values and vibration vectors at 1X were extracted from the raw data and shown in Table 5.

As can be seen, the vibration information collected from different sensors is distinct from one another, even from the same rotor section. The probe with the highest amplitude was chosen for the balancing task according to the maintenance experience to achieve a better contrast.

A trial weight of 9.8 g was located at 270° (both quantity and angle were randomly chosen). Based on conventional ICM, rotor balancing results were gained under the unloaded condition, which inferred that only mass unbalance failures were artificially concerned regardless of the mechanical assembly errors. Note that here the mass unbalance that can be treated as the inherent failure of the rotor system persisted through the whole duration.

*3.3.3. Rotor Balance Process with External Force Interference.* In practical experiments, a serial of experimental investigations have been established under different loading conditions. Considering the limit of the paper, only the condition with an additional T5R6 force was engaged to demonstrate the superior performance of the BSS-ICM algorithm. Moreover, in contrast to the previous analysis using the probe with the highest amplitude, all vibration signals were referred to the signal source to be analysed. Because there are two groups of orthogonally installed probes, the two raw signals were selected by the magnitude level. Herein, raw signals collected from 3# and 4# sensors were selected according to the magnitude. Corresponding waveforms of these two signals are described in Figure 9.

According to the algorithm flow, EEMD was used to process the selected raw signals to obtain the IMFs. Particularly, EEMD results extracted from the 3rd probe are representatively illustrated in Figure 10.

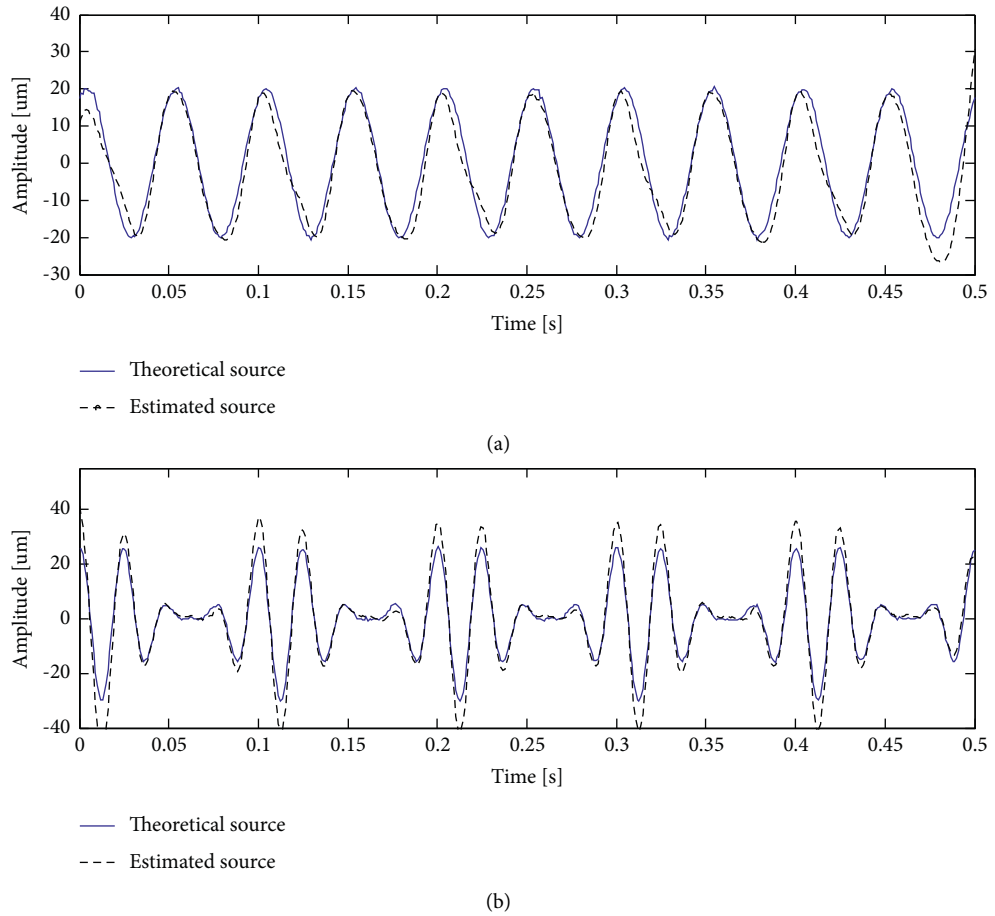


Figure 7: Source estimations using the proposed method.

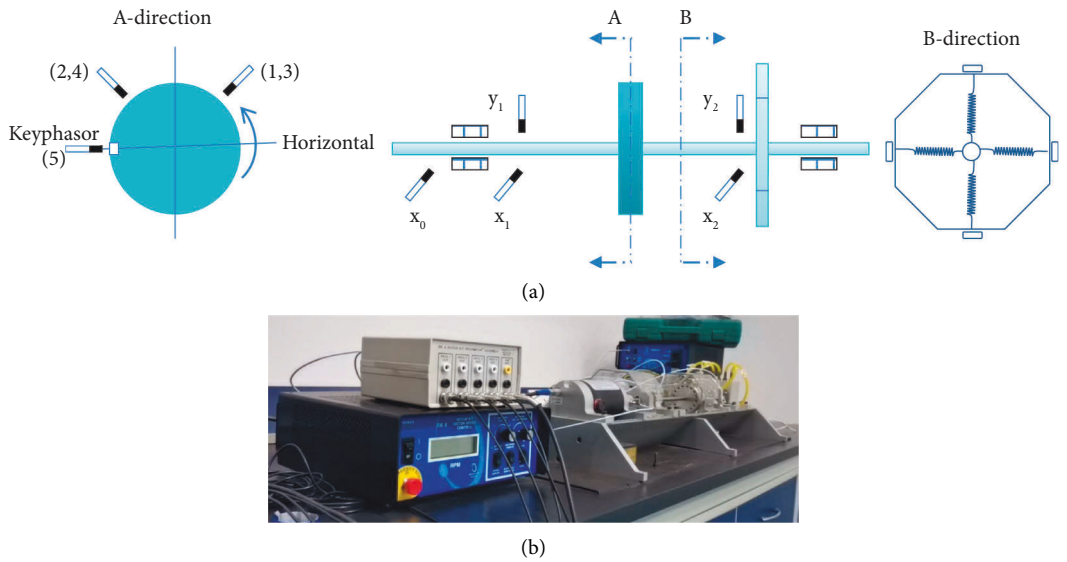


Figure 8: Bently Nevada Rotor Kit with a specific force loading device. (a) The structure chart and (b) the physical view.

Thereafter, the similarity between each IMF and the original vibration is computed using (11) to capture the most representative IMF. Together with the original signal, herein, the IMF with the most significant similarity (IMF4 owns the highest values in each group) is employed to form the mixing matrix for fault number determination and blind source separation.

Table 5: Vibration vectors of raw signals.

| Probes | 1st | 2nd | 3rd | 4th |
|---|---|---|---|---|
| Peak-to-peak value $\mu$m | 42.1 | 53.0 | 112.0 | 70.0 |
| 1X vector $\mu$m$\angle^{\circ}$ | 36.2$\angle$347 | 51.2$\angle$79 | 104$\angle$340 | 69.9$\angle$76 |

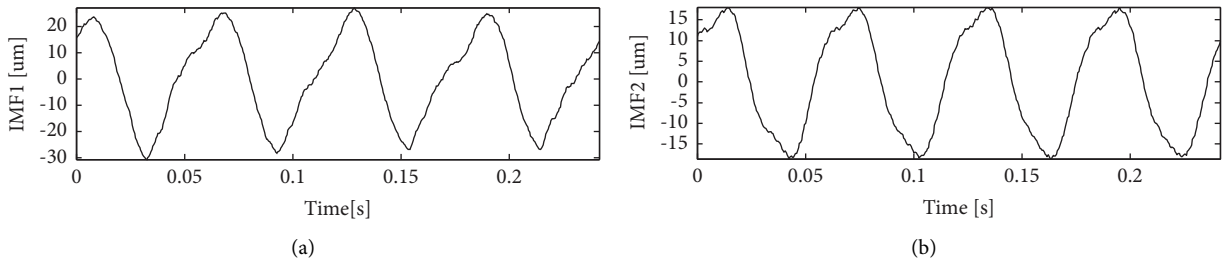


Figure 9: The original signal collected from (a) the 3# and (b) 4# sensors.

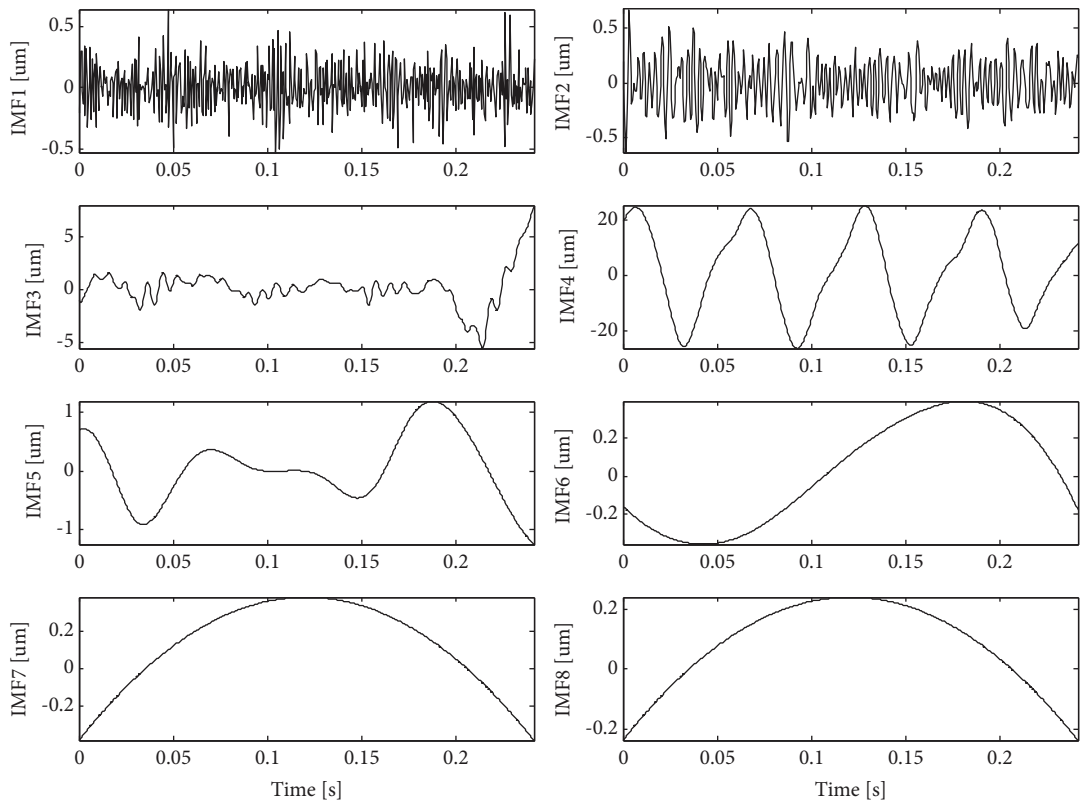


Figure 10: First eight IMFs of the 3rd vibration signal (from high- to low-frequency bands).

Table 6: Results of cosine similarities based on the first selected raw data.

| IMF | 1 | 2 | 3 | 4 | 5 | 6 | 7 | 8 |
|---|---|---|---|---|---|---|---|---|
| $\text{Sim}_{\cos}$ | 0.019 | 0.020 | 0.477 | 0.991 | 0.444 | 0.011 | 0.040 | 0.040 |

Tables 6 and 7 give the corresponding similarities of the two groups of IMFs, respectively.

Then, the SVD method is used for fault number estimation. Table 8 shows the details of the top 20 nonzero eigenvalues related to the new observed matrix. The decline ratios are illustrated in Figure 11.

In Figure 11, it is clear that the second ratio owns the most considerable value compared to the others. In other

Table 7: Results of cosine similarities based on the second selected raw data.

| IMF | 1 | 2 | 3 | 4 | 5 | 6 | 7 | 8 |
|---|---|---|---|---|---|---|---|---|
| $Sim_{cos}$ | 0.035 | 0.014 | 0.061 | 0.959 | 0.830 | 0.025 | 0.024 | 0.023 |

Table 8: Nonzero eigenvalues obtained by SVD.

| Index | 1 | 2 | 3 | 4 | 5 | 6 | 7 | 8 | 9 | 10 |
|---|---|---|---|---|---|---|---|---|---|---|
| $Sim_{cos}$ | 28273 | 28107 | 4004 | 3459 | 2188 | 2183 | 1168 | 735 | 321 | 207 |
| Index | 11 | 12 | 13 | 14 | 15 | 16 | 17 | 18 | 19 | 20 |
| $Sim_{cos}$ | 107 | 95 | 89 | 61 | 49 | 49 | 40 | 25 | 23 | 21 |

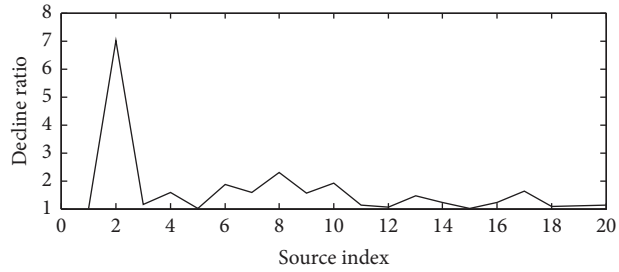


Figure 11: Changes of decline ratio with source index under experiment condition.

Table 9: Rotor balancing results using convention ICM without external force.

| Run state | At condition weight (g)/angle (°) | Vibration amplitude ($\mu$m) | Phase angle (°) | External force |
|---|---|---|---|---|
| Original | — | 104 | 340 | — |
| Trial | 9.8/270 | 51 | 345 | — |
| Balanced | 19/275 | 24.4 | 59 | — |

Final vibration amplitude reduction %: (104–24.4)/104 = 76.54%.

words, the rotor system suffers from two main faults that correspond to the mass unbalance and the simulated fault generated by the external force.

Thereafter, NMF is adopted to separate the main sources from the new observed matrix, and the relationship between the decomposed signals and the two faults can be determined based on the frequency distribution. The corresponding order spectrums are introduced to obtain a much more precise balancer vector, because the order spectrum is able to eliminate the interference of the speed fluctuation.

The proposed method is validated during the whole balancing process without additional operations. Thus, the above flow involving some key steps (steps 1, 2, 4, and 5 in Section 2.4) will be repeated to obtain the corresponding vibration information under the trial condition. Note that SVD can be omitted in this case since the source number has been obtained under the original vibration situation.

Finally, once all relevant information has been obtained, ICM is employed to accomplish the rotor balancing task. Three sets of analytical results are calculated using the conventional ICM. The corresponding results are intensively elaborated in Tables 9–11.

*3.3.4. Results and Discussions.* According to the rotor balancing results in Tables 9–11, a brief summary can be reached. (1) Conventional ICM plays an important role in the process of rigid rotor balancing, in which the axial vibrations at 3# in cases 1 and 2 were reduced by more than 75% after field balancing. (2) The impact of the additional force is undeniable, where all amplitudes of vibrations decrease to a slighter level under the external radial force. (3) Significant changes are seen in the final balancer vectors in two cases, especially, in the correction angle, where a deviation angle of 40° is obtained. In reality, the deviation is an outrageous option. It can be easily inferred that once the external force disappears (e.g., the run-in period after the overhaul), the inappropriate installation may result in the opposite effect or uncontrollable situations like a malfunction or even fatal damage. (4) Regardless of the amplitude difference, the final balancer vector obtained by BSS-ICM in case 3 is much more effective. Compared to the referred angle in case 1, a nearly identical correction angle has been achieved, which indicates that the optimal installation position has been figured out, even if the balancing effectiveness may decline. However, the inherent balancing has been accurately modified accordingly.

Table 10: Rotor balancing results using convention ICM with external force.

| Run state | At condition weight (g)/angle (°) | Vibration amplitude ($\mu$m) | Phase angle (°) | External force |
|---|---|---|---|---|
| Original | — | 43 | 26 | T5R6 |
| Trial | 4.9/135 | 75.8 | 24 | T5R6 |
| Balanced | 6.5/315 | 8.5 | 129 | T5R6 |

Final vibration amplitude reduction %: (43–8.5)/43 = 80.23%. Final amplitude error of balancer vector %: (19–6.5)/19 = 65.8%. Final angle error of balancer vector %: (278-275)/275 = 14.55%.

Table 11: Rotor balancing results using BSS-ICM with external force.

| Run state | At condition weight (g)/angle (°) | Vibration amplitude ($\mu$m) | Phase angle (°) | External force |
|---|---|---|---|---|
| Original | — | 39.41 | 95 | T5R6 |
| Trial | 4.9/135 | 50.75 | 104 | T5R6 |
| Balanced | 14.48/278 | — | — | T5R6 |

Final amplitude error of balancer vector %: (19–14.48)/19 = 23.8%. Final angle error of balancer vector %: (278-275)/275 = 1.09%.

## 4. Conclusions

In this paper, a hybrid method named BSS-ICM is successfully developed. In conjunction with the superiority of EEMD, SVD, and NMF, extraction and division of multiple features have been accomplished. The corresponding analysis results and conclusions are given as follows:

(1) The hybrid method is capable of maximizing the use of the vibration information, where signals collected from different sensors are involved for further analysis.

(2) A root dynamic balancing and implemental framework is successfully developed to accomplish the task of vibration reduction.

(3) The effectiveness of the proposed method is verified using both numerical simulations and practical applications, in which the signal characteristics of the common rotor failure are successfully obtained and utilized for further analysis, i.e., rotor balancing.

(4) Results of simulations and experiments indicate that the novel method has the potential ability of extracting the inherent faults from the mixed vibration signals.

Nevertheless the investigation on rotor balancing by means of BSS is still in its infancy, and modern signal processing techniques have not been sufficiently applied to this field yet, there is a slight amplitude deviation between the two balancers obtained by BSS-ICM and conventional ICM. Moreover, the final balancer vector cannot be verified because of the permission restrictions and algorithm development period, even though, based on the angle information, it still can be deduced that the calculation result meets the requirements of inherent rotor balancing.

## Data Availability

The test data used to support the findings of this study are available from the corresponding author upon request.

## Conflicts of Interest

The authors declare that they have no conflicts of interest.

## Acknowledgments

This current work was supported by the Postdoctoral Science Foundation of China (Grant no. 2021M692603), the Natural Science Basic Research Program of Shaanxi (Grant no. 2022JM-264), and the Fundamental Research Funds for State Key Laboratory of Compressor Technology (Anhui Laboratory of Compressor Technology) (Grant nos. SKL-YSJ202106 and SKL-YSJ201907), which is highly appreciated by the authors.

## References

[1] A. M. Haidar and J. L. Palacios, "Modified ball-type Automatic balancer for rotating shafts: analysis and experiment," *Journal of Sound and Vibration*, vol. 496, Article ID 115927, 2021.

[2] A. A. Ibraheem, N. M. Ghazaly, and G. Abdel-Jaber, "Review of rotor balancing techniques," *American Journal of Industrial Engineering*, vol. 6, pp. 19–25, 2019.

[3] A. R. Bhende, "A new rotor balancing method using amplitude subtraction and its performance analysis with phase angle measurement-based rotor balancing method," *Australian Journal of Mechanical Engineering*, vol. 18, no. 1, pp. 112–118, 2020.

[4] J. Wu, X. Zhang, and B. Li, "A study on vibration component separation of a rotor system during startup and its application in fault diagnosis," *Measurement Science and Technology*, vol. 30, no. 9, Article ID 095104, 2019.

[5] G. Ranjan and R. Tiwari, "Application of active magnetic bearings for in situ flexible rotor residual balancing using a novel generalized influence coefficient method," *Inverse Problems in Science and Engineering*, vol. 27, no. 7, pp. 943–968, 2019.

[6] R. Ye, L. Wang, X. Hou, Z. Luo, and Q. Han, "Balancing method without trial weights for rotor systems based on similitude scale model," *Frontiers of Mechanical Engineering*, vol. 13, no. 4, pp. 571–580, 2018.

[7] S. Liu, "A modified low-speed balancing method for flexible rotors based on holospectrum," *Mechanical Systems and Signal Processing*, vol. 21, no. 1, pp. 348–364, 2007.

[8] D. S. Alves, T. H. Machado, K. L. Cavalca, and N. Bachschmid, "Characteristics of oil film nonlinearity in bearings and its effects in rotor balancing," *Journal of Sound and Vibration*, vol. 459, Article ID 114854, 2019.

[9] S. Singh and N. Kumar, "Combined rotor fault diagnosis in rotating machinery using empirical mode decomposition," *Journal of Mechanical Science and Technology*, vol. 28, no. 12, pp. 4869–4876, 2014.

[10] S. Zhao, X. Ren, W. Deng, K. Lu, Y. Yang, and C. Fu, "A transient characteristic-based balancing method of rotor system without trail weights," *Mechanical Systems and Signal Processing*, vol. 148, Article ID 107117, 2021.

[11] V. Prasad and R. Tiwari, "Identification of speed-Dependent active magnetic bearing parameters and rotor Balancing in high-speed rotor Systems," *Journal of Dynamic Systems, Measurement, and Control*, vol. 141, no. 4, 2019.

[12] G. Ranjan and R. Tiwari, "On-site high-speed balancing of flexible rotor-bearing system using virtual trial unbalances at slow run," *International Journal of Mechanical Sciences*, vol. 183, Article ID 105786, 2020.

[13] B. Silwal, P. Rasilo, L. Perkkiö, A. Hannukainen, T. Eirola, and A. Arkkio, "Numerical analysis of the power balance of an electrical machine with rotor eccentricity," *IEEE Transactions on Magnetics*, vol. 52, no. 3, pp. 1–4, 2016.

[14] S. Liu and L. Qu, "A new field balancing method of rotor systems based on holospectrum and genetic algorithm," *Applied Soft Computing*, vol. 8, no. 1, pp. 446–455, 2008.

[15] Y. Liao, G. Lang, F. Wu, and L. Qu, "An improvement to holospectrum based field balancing method by reselection of balancing object," *Journal of Vibration and Acoustics*, vol. 131, no. 3, 2009.

[16] X. Yu, K. Mao, S. Lei, and Y. Zhu, "A new adaptive proportional-integral control strategy for rotor active balancing systems during acceleration," *Mechanism and Machine Theory*, vol. 136, pp. 105–121, 2019.

[17] D. J. Rodrigues, A. Champneys, M. Friswell, and R. Wilson, "Experimental investigation of a single-plane automatic balancing mechanism for a rigid rotor," *Journal of Sound and Vibration*, vol. 330, no. 3, pp. 385–403, 2011.

[18] M. Tiwari, K. Gupta, and O. Prakash, "Dynamic response of an unbalanced rotor supported on ball bearings," *Journal of Sound and Vibration*, vol. 238, no. 5, pp. 757–779, 2000.

[19] B. Li, C. Xie, B. Lang, S. Lu, and X. Zhang, "Effect analysis of rotor balancing under conditions of external forces," *Presented at the the 5th International Conference on Robotics*, Control and Automation, Seoul, 2021.

[20] C. Y. Yu, Y. Li, B. Fei, and W. L. Li, "Blind source separation based x-ray image denoising from an image sequence," *Review of Scientific Instruments*, vol. 86, no. 9, pp. 093701–093771, 2015.

[21] J. Wodecki, P. Kruczek, A. Bartkowiak, R. Zimroz, and A. Wyłomańska, "Novel method of informative frequency band selection for vibration signal using Nonnegative Matrix Factorization of spectrogram matrix," *Mechanical Systems and Signal Processing*, vol. 130, pp. 585–596, 2019.

[22] P. O. Hoyer, "Non-negative matrix factorization with sparseness constraints," *Journal of Machine Learning Research*, vol. 5, 2004.

[23] Y.-s. Yang, A.-b. Ming, Y.-y. Zhang, and Y.-s. Zhu, "Discriminative non-negative matrix factorization (DNMF) and its application to the fault diagnosis of diesel engine," *Mechanical Systems and Signal Processing*, vol. 95, pp. 158–171, 2017.

[24] B. Li, X. Zhang, and J. Wu, "New procedure for gear fault detection and diagnosis using instantaneous angular speed," *Mechanical Systems and Signal Processing*, vol. 85, pp. 415–428, 2017.

[25] Z. Wu and N. E. Huang, "Ensemble empirical mode decomposition: a noise-assisted data analysis method," *Advances in Adaptive Data Analysis*, vol. 1, no. 1, pp. 1–41, 2009.

[26] F. Jiang, Z. Zhu, W. Li, G. Chen, and G. Zhou, "Robust condition monitoring and fault diagnosis of rolling element bearings using improved EEMD and statistical features," *Measurement Science and Technology*, vol. 25, no. 2, Article ID 025003, 2013.

[27] Y. Lei, Z. He, and Y. Zi, "Application of the EEMD method to rotor fault diagnosis of rotating machinery," *Mechanical Systems and Signal Processing*, vol. 23, no. 4, pp. 1327–1338, 2009.

[28] S. Zhou, S. W. Dyer, K.-k. Shin, J. Shi, and J. Ni, "Extended influence coefficient method for rotor active balancing during acceleration," *Journal of Dynamic Systems, Measurement, and Control*, vol. 126, no. 1, pp. 219–223, 2004.

Hindawi
Shock and Vibration
Volume 2022, Article ID 1546622, 19 pages
https://doi.org/10.1155/2022/1546622

*Research Article*

# Three-Level SOC Equalization Control Strategy for MMC-BESS Based on Feedforward Sliding Window Integral Method

**Yuan Cheng,[1,2] Hui Zhang ,[1] Xiaohui Wei,[3] and Wenquan Shao[2]**

[1]*School of Electrical Engineering, Xi' an University of Technology, Xi' an 710048, China*
[2]*School of Electronics Information, Xi'an Polytechnic University, Xi'an 710048, China*
[3]*Xi'an Electric Power Supply Company of State Grid Shaanxi Electric Power Company, Xi'an 710032, China*

Correspondence should be addressed to Hui Zhang; zhangh@xaut.edu.cn

Received 10 December 2021; Revised 31 May 2022; Accepted 2 June 2022; Published 20 September 2022

Academic Editor: Liu Jing



The modular multilevel converter of the battery energy storage system (MMC-BESS) not only is suitable for the large-scale energy storage and dispatching of AC and DC grids, but also has a strong ability to suppress power fluctuations caused by the new energy output or grid failures. When an asymmetric voltage or a sudden change in DC load occurs in the AC grid, in order to compensate for the power difference between AC and DC sides, the energy storage submodule of the MMC-BESS will have a large unbalanced charging and discharging current, destroying the equalization state of SOC and seriously affecting energy storage capacity utilization and battery service life. In order to deal with the above problems, in this paper, the characteristics of the power difference between the MMC-BESS phase unit and the upper and lower bridge arms are analyzed. It is found that when considering the fluctuation of the submodule capacitor voltage, the phase unit power has the fundamental frequency AC circulating current component, and the power difference between the upper and lower bridge arms has the DC circulating current component. Therefore, the three-level SOC equalization correction control strategy is proposed based on interphase, upper and lower bridge arms, and submodules, and the feedforward sliding window integral method is introduced into the SOC equalization correction control layer of upper and lower bridge arms, so as to achieve the purpose of more balanced and accurate power distribution among phases and among upper and lower bridge arms of each phase. The simulation results show that the MMC-BESS has effective compensation ability when there is a large power difference in the AC and DC power grid. Under the unbalanced working conditions of the three-phase power grid, the three-phase AC current can quickly reach equalization, and the total harmonic content is 1.38%, and the unbalance degree is 2.4%. Under the same operating conditions, compared with the traditional optimal one-third average method, the SOC equalization correction control strategy proposed in this paper has smaller submodule capacitor voltage fluctuation rate, harmonic distortion rate, and three-phase system circulating current. And the SOC of each phase has a faster equalization convergence speed.

## 1. Introduction

In recent years, with the large-scale access of new energy resources, the randomness of its power flow has brought severe challenges to the safe and stable operation of the power grid [1]. In the case of power quality problems mainly due to voltage sag [2] caused by uneven output of new energy sources or sudden load changes in the AC and DC grids, the energy storage system, as a balance medium between power and time scale, can not only buffer the power fluctuation caused by new energy power generation, but also effectively improve the power quality of the power grid [3–5].

Modular multilevel converters are currently widely used in high-voltage DC transmission, new energy power generation, and other medium-high-voltage and large-capacity occasions due to their highly modular structure, low harmonic content of AC output, and strong redundancy [6, 7]. Combining the MMC with the lithium battery, which has high energy density, high power density, and high energy conversion efficiency [8], can give full play to the ability of the MMC-BESS to adjust power quality and smooth power

fluctuation output in medium and high power occasions [9–11].

In AC and DC power grids, the unbalanced grid-side voltage of the three-phase or the large sudden change of AC and DC load makes the system bus voltage unstable and increases the system circulating current, which causes damage to electrical products, misoperation of power grid protection, and reduces the service life of distribution grid operation equipment, etc. [12, 13]. The use of the large-capacity MMC-BESS can supplement the power difference between the AC and DC sides, smooth power fluctuations, and improve the system power quality [14, 15]. However, when the battery in the MMC-BESS is in use, long-term unbalanced high current charging and discharging will affect its SOC equalization state and energy storage capacity utilization, resulting in a decrease in battery life [16].

Therefore, it is essential to carry out the research on the SOC equalization control of the MMC-BESS. Literature [17] used zero-sequence voltage and fundamental frequency circulating current injection to achieve the SOC balance among phases and among upper and lower bridge arms, but the calculation principle is complicated. Literature [18] introduced the energy storage MMC system in which the energy storage battery was directly connected to the submodules. The DC circulating current and the fundamental frequency circulating current were extracted and corrected to balance the power among the phases and the upper and lower bridge arms. This method is more complicated in the extraction process and requires an additional DC circulating current suppressor. Literature [19] introduced an MMC energy management system based on the EV battery, which adopted a two-level SOC equalization correction control strategy of phase unit and upper and lower bridge arms to achieve the SOC equalization of each energy storage submodule, but the upper and lower bridge arm equalization correction control of PR control was not considered. Due to the bandwidth limitation, the equalization correction control can only complete the zero-static-error tracking of signals with fixed frequency and cannot guarantee the accuracy of the energy equalization of the upper and lower bridge arms. In literature [20], under the condition of the unbalanced grid-side voltage, DC circulation injection is used to achieve the SOC equalization, but the SOC equalization of upper and lower bridge arms was not considered. Literature [21] used the three-level SOC equalization correction control to achieve the SOC equalization of each energy storage submodule under the unbalanced three-phase power grid, but the SOC equalization correction control layer of the upper and lower arms did not perform signal processing on the output correction. Harmonic signals of different frequencies caused fluctuations in the power difference between the upper and lower bridge arms. Literature [22] introduced that the energy storage battery was connected to the MMC submodule system through a Bi-directional DC-DC, and the SOC control was realized. In the upper and lower bridge arm balance control layer, only the three-phase SOC correction was averaged, and the accuracy of the correction was slightly deficient.

Based on the above, this paper proposes an improved three-level SOC equalization correction control strategy for the MMC-BESS based on analyzing the characteristics of the difference between the phase unit power and the bridge arm power. Feedforward is used in the SOC equalization correction control layer of upper and lower bridge arms. The sliding window integral method is used to process the harmonic signals of the correction value, so as to realize the accurate equalization of the power of the upper and lower arms of each phase unit, which can make the SOC of each energy storage submodule more quickly balanced and converged.

In Section 1, the operating state of the MMC-BESS, the main circuit topology, and the principle of the energy storage submodule are analyzed, and the voltage/current switching function model of phase unit bridge arm is established. Based on this, the internal characteristics of phase unit and bridge arm unit are analyzed. When not considering the capacitor voltage fluctuation of the submodule, the phase unit power is composed of the DC component, the double frequency AC component, and the AC output. The power difference between the upper and lower bridge arms is composed of the fundamental frequency component and the fundamental frequency AC output. If the capacitor voltage fluctuation of the submodule is considered, the phase unit power will increase the fundamental frequency circulating current component, and the power difference between the upper and lower bridge arms will increase the DC circulating current component. The results show that the AC fundamental frequency/double frequency circulation and DC circulation have an important influence on the average power distribution of the phase unit and the accurate power distribution of upper and lower bridge arms.

Section 2 constructs its double closed-loop control system based on the mathematical model of the MMC-BESS single-phase equivalent circuit and introduces the principle and stability analysis of the double closed-loop control system of the Bidirectional DC-DC converter applied to the energy storage submodule. A three-level SOC control system model is constructed based on interphase, upper and lower bridge arms, and each submodule. In the upper and lower bridge arm equalization control [23], the correction factor and the feedforward sliding window integral method are introduced [24, 25]. Compared with the traditional optimal one-third average method, which only distributes the DC circulation bias to three phases evenly, the feedforward sliding window integral method completely suppresses the DC circulation bias.

In Section 3, the lithium battery of energy storage submodule is continuously discharged, and the three-level SOC equalization correction controller is started under the conditions of sudden change of DC load/50% drop of two-phase voltage of the three-phase AC power grid. The results show that the DC bus voltage is stable at 20 kV under both working conditions. When the two-phase voltage drops, the three-phase AC current can be effectively compensated and balanced. Compared with the one-third average method, the three-level SOC equalization correction control strategy

proposed in this paper makes the capacitor voltage of the submodule stable at 5000 V under the condition of high current discharge, and the fluctuation rate and total harmonic distortion rate are smaller. The three-phase circulating current suppression effect of the system is better, so the phase unit power distribution is more balanced, and the upper and lower bridge arm power distribution is more accurate. Through comparative analysis, the SOC equalization correction control proposed in this paper makes the SOC of three-phase lithium battery have faster equalization convergence speed and better consistency.

## 2. Basic Principle of Energy Storage MMC

*2.1. MMC-BESS Operating Status Analysis.* The AC/DC grid system structure is shown in Figure 1. On the AC bus side, the MMC-BESS can be used as a power conversion and energy storage system for wind power generation units, and it can also be connected to a higher voltage grid. On the DC bus side, the MMC-BESS can complete DC energy interaction with photovoltaic power generation units, electric vehicles, energy feedback systems, etc. On the energy storage unit side, if the input/output power of the AC bus side and the DC bus side are equal, the MMC-BESS can be used as an AC/DC power converter. Therefore, the MMC-BESS can be equivalent to a three-port grid for power transmission among the AC bus side, the DC bus side, and the lithium battery energy storage system. There are 12 operating conditions in total. The working conditions simulated in this paper are DC load sudden change and two-phase voltage drop of three-phase network side voltage by 50%. The Bidirectional DC-DC converter of MMC-BESS energy storage system works in boost mode, and the lithium battery is continuously discharged.

*2.2. MMC-BESS Topology.* As shown in Figure 2, the MMC-BESS has the same three-phase structure and is connected in parallel to the DC bus side. Each phase can be divided into upper and lower bridge arms. Each bridge arm is composed of N energy storage submodules containing lithium batteries in series with the bridge arm inductor $L_{\mathrm{em}}$ and the bridge arm equivalent resistor $R_{\mathrm{em}}$.

where $u_{px}$ and $u_{nx}$ represent the output voltage of the upper and lower bridge arm of energy storage submodules of phase $X$, respectively; $i_{px}$ and $i_{nx}$ represent the currents flowing through upper and lower bridge arms of phase $X$, respectively; $e_x$ and $i_x$ represent the x-phase voltage and current of the AC bus side, respectively. The number of phases $x = a, b,$ c. $L_s$ is the balanced filter inductor between the AC bus and the AC output port of the MMC-BESS. $U_{\mathrm{dc}}$ represents the DC bus voltage.

*2.2.1. Energy Storage Submodule.* As shown in Figures 3 and 4, the energy storage submodule is composed of a half-bridge submodule and an energy storage system. By controlling the switching states of the half-bridge submodules $VT_1$ and $VT_2$, the charging and discharging of the capacitor $C_{\mathrm{m}}$ are changed to maintain the stability of the DC voltage of each phase. The energy storage system includes the Bidirectional DC-DC, energy storage filter inductor $L_{\mathrm{bat}}$ and the lithium battery. When the Bidirectional DC-DC converter operated in the Buck mode, the half-bridge submodule capacitor charged the lithium battery. The capacitor voltage of the half-bridge submodule was greater than its ideal value, $VT_3$ was turned on, and the half-bridge submodule discharged to the lithium battery. The capacitor voltage of half-bridge submodule was equal to or less than its ideal value, $VD_4$ was turned on, and there was no energy interaction between them. When the Bidirectional DC-DC operated in the Boost mode, the lithium battery charged the capacitor of the half-bridge submodule. The capacitor voltage of the half-bridge submodule was less than its ideal value, $VD_3$ was turned on, and the lithium battery charged the capacitor of the half-bridge submodule. The capacitor voltage of the half-bridge submodule was equal to or greater than its ideal value, $VT_4$ was turned on, and there was no energy interaction between them. From the above Bidirectional DC-DC working mode analysis, it can be seen that the lithium battery of the energy storage system operated in a low-voltage condition, and the charging and discharging current had a high degree of controllability (Table 1).

*2.2.2. Bridge Arm Voltage/Current Switching Function Model.* During the stable operation of the MMC-BESS, the capacitor of the energy storage submodule not only flows through the bridge arm current for energy interaction with AC and DC sides, but also flows the charging and discharging current of the lithium battery in the energy storage system. Taking one phase as an example, the switching function $s$ of its energy storage submodule is defined as

$$s = \begin{cases} 1, & \mathrm{VT}_1\,(\mathrm{on}), \mathrm{VT}_2\,(\mathrm{off}), \\ 0, & \mathrm{VT}_1\,(\mathrm{off}), \mathrm{VT}_2\,(\mathrm{on}). \end{cases} \tag{1}$$

Thus, the output voltage of the energy storage submodule port of phase unit bridge arm is expressed as

$$\begin{cases} u_{ixk} = s_{ixk} U_{smk}, \\ \\ C_m \dfrac{\mathrm{d}U_{\mathrm{smk}}}{\mathrm{d}t} = s_{ixk} i_{ix} + i_{Lbk}, \end{cases} \tag{2}$$

where $u_{ixk}$ is the output voltage value of the k-th submodule in the upper or lower bridge arm of one phase, $U_{smk}$ is the capacitor voltage of the submodule, and $s_{ixk}$ is the switching function; $i_{ix}$ is the current of the upper or lower bridge arm of one phase, and $i_{Lbk}$ is charging and discharging current of the lithium battery of the energy storage system. In equation (2), $i = p$ (upper bridge arm) or $n$ (lower bridge arm), the number of phases $x = a, b,$ c; $k = 1 \sim N$ representing the number of submodules of the same bridge arm.

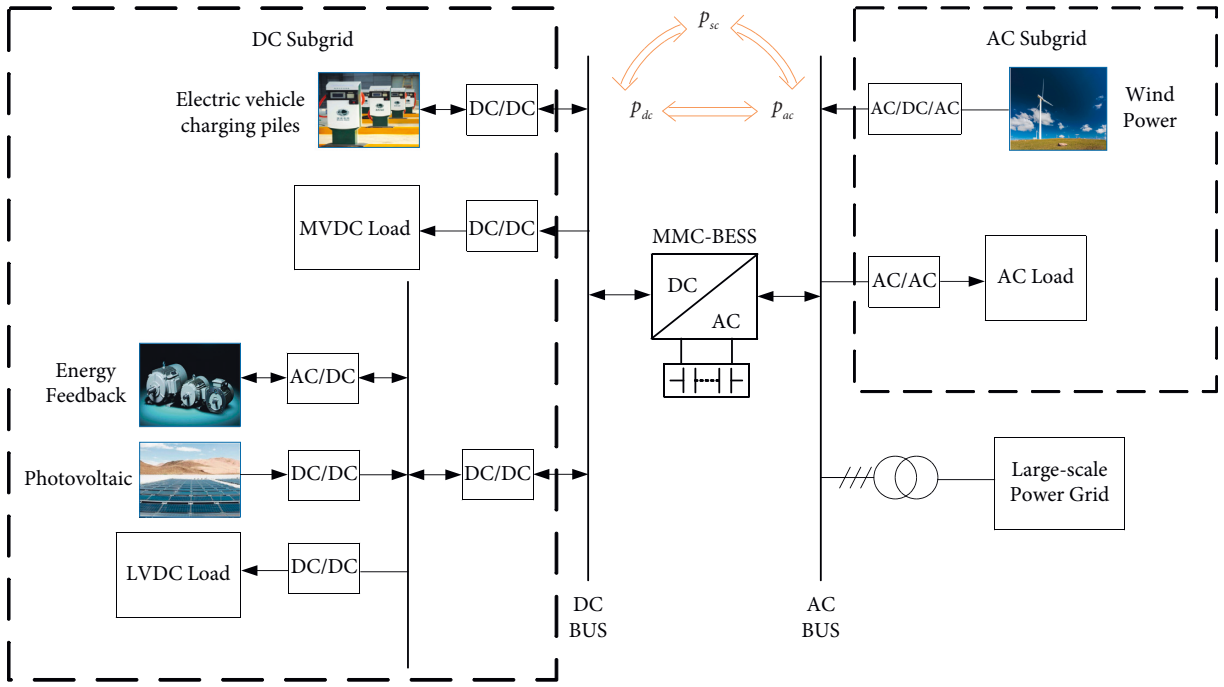


Figure 1: AC/DC grid system structure.

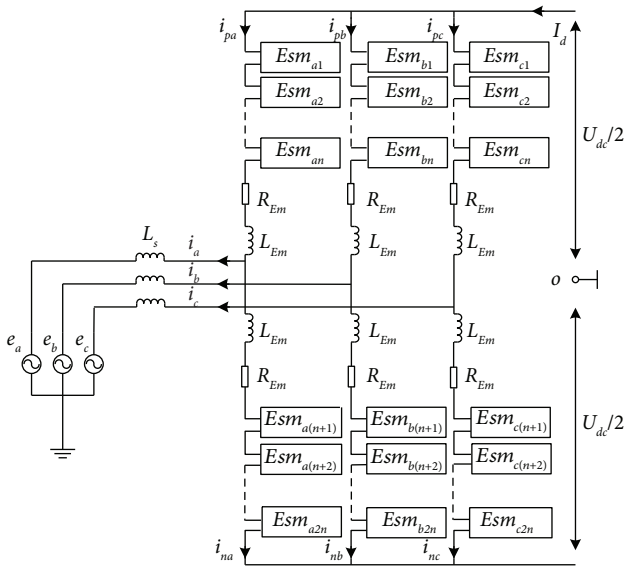


Figure 2: MMC-BESS main circuit topology.

Therefore, the bridge arm output voltage $u_{ix}$ and output current $i_{ix}$ can be expressed as

$$\begin{cases} u_{ix} = \sum_{k=1}^{N} s_{ixk} U_{smk}, C_m \dfrac{d\sum_{k=1}^{N} s_{ixk} U_{smk}}{dt} = i_{ix} + \sum_{k=1}^{N} s_{isk} i_{Lbk}. \end{cases} \tag{3}$$

Ignoring the equivalent impedance of the bridge arm, the KVL equation for the upper and lower bridge arms is expressed as follows:

$$\begin{cases} u_{px} = \dfrac{1}{2} U_{dc} - E_a \sin(\omega t), \\ u_{nx} = \dfrac{1}{2} U_{dc} + E_a \sin(\omega t), \end{cases} \tag{4}$$

where $u_{px}$ and $u_{nx}$ are the upper and lower arm voltages of the $x$-th phase, respectively; $E_a$ is the peak value of the AC voltage; $U_{dc}$ is DC-side voltage.

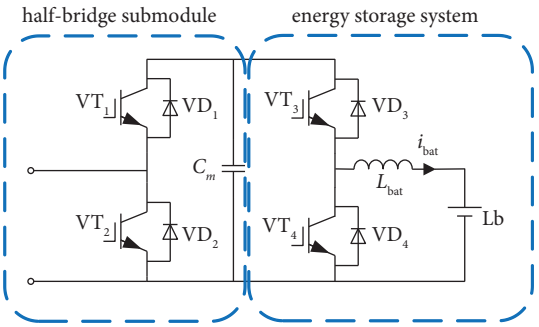


Figure 3: Energy storage submodule.

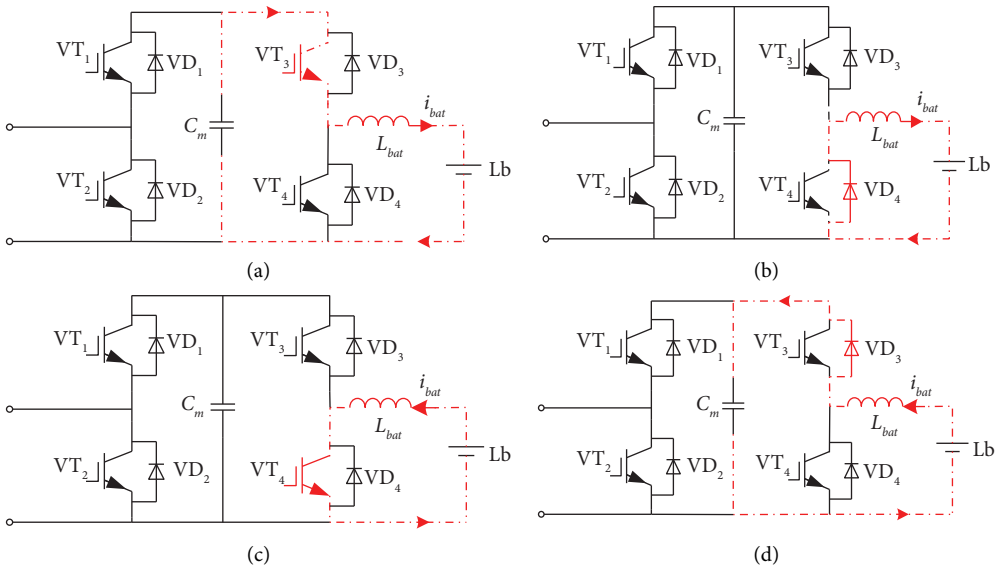


Figure 4: Energy interaction status of the lithium battery in the buck and boost working modes. (a) In the buck mode, with energy interaction. (b) In the buck mode, without energy interaction. (c) In the boost mode, without energy interaction. (d) In the boost mode, with energy interaction.

*2.2.3. Analysis of Internal Characteristics of Phase Unit and Bridge Arm Unit.* In order to achieve a better control effect and master the control law of the MMC-BESS, the internal characteristics of the phase unit and the bridge arm unit are analyzed. According to equations (4), the following equations are obtained:

$$\begin{cases} u_{px} = \dfrac{\sum_{k=1}^{N} U_{\text{smk}}}{2} - \dfrac{\sum_{k=1}^{N} mU_{\text{smk}} \sin(\omega t)}{2}, \\ u_{nx} = \dfrac{\sum_{k=1}^{N} U_{\text{smk}}}{2} + \dfrac{\sum_{k=1}^{N} mU_{\text{smk}} \sin(\omega t)}{2}, \end{cases} \tag{5}$$

where $m$ is the modulation ratio, and $U_{\text{smk}}$ is the capacitor voltage of the energy storage submodule, which is put into operation in the x-th phase. Based on the single-phase equivalent circuit, the KAL equation of the upper and lower bridge arms is obtained as follows:

$$\begin{cases} i_{px} = \dfrac{1}{3} I_{dc} + \dfrac{I_x \sin(\omega t - \varphi)}{2}, \\ i_{nx} = \dfrac{1}{3} I_{dc} - \dfrac{I_x \sin(\omega t - \varphi)}{2}, \end{cases} \tag{6}$$

where $i_{px}$ and $i_{nx}$ are the currents flowing through the upper and lower bridge arms, $I_{\text{dc}}$ is the DC output current, $I_x$ is the peak value of the phase AC current, and $\varphi$ is the impedance angle. From (5) and (6), the power of phase unit and upper and lower bridge arms can be obtained expressed as (7) and (8) (without considering the capacitor voltage of the submodule):

Table 1: MMC-BESS interaction status and energy storage system working mode.

| MMC-BESS interaction status | DC-DC working mode | Lithium battery charge/discharge status | $VT_3$ | $VT_4$ | Submodule capacitor voltage status | Circuit |
|---|---|---|---|---|---|---|
| $p_{bat} = 1$ (absorbed power) | Buck mode | Charge | PWM | 0 | $U_{sm} > U_{smref}$<br>$U_{sm} < U_{smref}$ | Figure 4(a)<br>Figure 4(b) |
| $p_{bat} = 1$ (output power) | Boost mode | Discharge | 0 | PWM | $U_{sm} > U_{smref}$<br>$U_{sm} < U_{smref}$ | Figure 4(c)<br>Figure 4(d) |

*Note.* $U_{sm}$ represents the actual value of the submodule capacitor voltage; $U_{smref}$ represents the ideal value of the submodule capacitor voltage.

$$p_x = \underbrace{\frac{I_{dc}\sum_{k=1}^{N} U_{smk}}{3}}_{\text{DC component}} + \underbrace{\frac{I_x\sum_{k=1}^{N} mU_{smk}\cos 2\omega t}{4}}_{\text{double frequency AC component}} - \underbrace{\frac{I_x\sum_{k=1}^{N} mU_{smk}\cos\varphi}{4}}_{\text{AC output}}, \tag{7}$$

$$\Delta p_x = \underbrace{\frac{I_{dc}\sum_{k=1}^{N} mU_{smk}\sin\omega t}{3} + \frac{I_x\sum_{k=1}^{N} U_{smk}\cos\omega t\sin\varphi}{2}}_{\text{fundamental frequency AC component}} - \underbrace{\frac{I_x\sum_{k=1}^{N} U_{smk}\sin\omega t\cos\varphi}{2}}_{\text{AC output}}, \tag{8}$$

where $p_x$ represents the power of the phase unit, and $\Delta p_x$ represents the power difference of upper and lower bridge arms.

When considering capacitor voltage fluctuation of the submodule, $p_x$ and $\Delta p_x$ are, respectively, expressed as (9) and (10):

$$p_x = \underbrace{\frac{I_{dc}\sum_{k=1}^{N} U_{smk}}{3}}_{\text{DC component}} + \underbrace{\frac{I_x\sum_{k=1}^{N} mU_{smk}\cos 2\omega t}{4}}_{\text{double frequency AC component}} - \underbrace{\frac{I_x\sum_{k=1}^{N} mU_{smk}\cos\varphi}{4}}_{\text{AC output}} + \underbrace{\left|\frac{I_{dc}\sum_{k=1}^{N} m\Delta U_{smk}\sin\omega t}{6}\right|}_{\substack{\text{Fundamental frequency AC} \\ \text{circulating current component}}}, \tag{9}$$

$$\Delta p_x = \underbrace{\frac{I_{dc}\sum_{k=1}^{N} mU_{smk}\sin\omega t}{3} + \frac{I_x\sum_{k=1}^{N} U_{smk}\cos\omega t\sin\varphi}{2}}_{\text{fundamental frequency AC component}} - \underbrace{\frac{I_x\sum_{k=1}^{N} U_{smk}\sin\omega t\cos\varphi}{2}}_{\text{AC output}} + \underbrace{\left|\frac{I_{dc}\sum_{k=1}^{N} \Delta U_{smk}}{6}\right|}_{\substack{\text{DC circulating} \\ \text{current component}}}. \tag{10}$$

By comparing (7) with (9), it can be seen that when considering the fluctuation of the capacitor voltage of the submodule, the phase unit power will increase the fundamental frequency AC circulating current component. By comparing (8) with (10), it can be seen that when considering the fluctuation of the capacitor voltage of the submodule, the power difference between upper and lower bridge arms will increase the DC circulating current component. Figures 5 and 6 are the power difference curves between the phase unit and the upper and lower bridge arms, which are drawn according to the actual parameters of the system. In Figure 5, the green curve includes the DC component and AC output. The blue curve includes the DC component, the double frequency AC component, and AC output. The red curve includes DC component, the double frequency AC component, the fundamental frequency circulation component, and AC output. It shows that the fundamental frequency circulating current component formed by the capacitor voltage fluctuation of the submodule caused uneven power distribution of the phase unit.

In Figure 6, the blue curve includes the AC component, the fundamental frequency, and AC output. The red curve includes the fundamental frequency AC component, AC output, and the DC circulation component. It shows that the DC circulating current caused by the capacitor voltage fluctuation of the submodule caused the inaccurate power distribution of the upper and lower bridge arms.

Therefore, the essential reason for constructing the three-level SOC equalization correction control is to suppress the fundamental frequency circulation of phase unit and the DC circulation of upper and lower bridge arms caused by the fluctuation of capacitor voltage of submodule.

## 3. MMC-BESS Hierarchical Control System

The MMC-BESS hierarchical control is shown in Figure 7, which is mainly composed of the main control system, the three-level SOC equalization correction control, and the Bidirectional DC-DC converter control system based on PI control. The main control system collected the active and

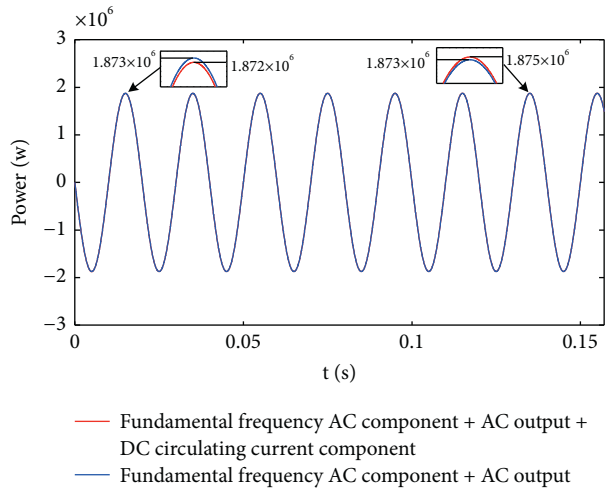


Figure 5: Phase unit power.

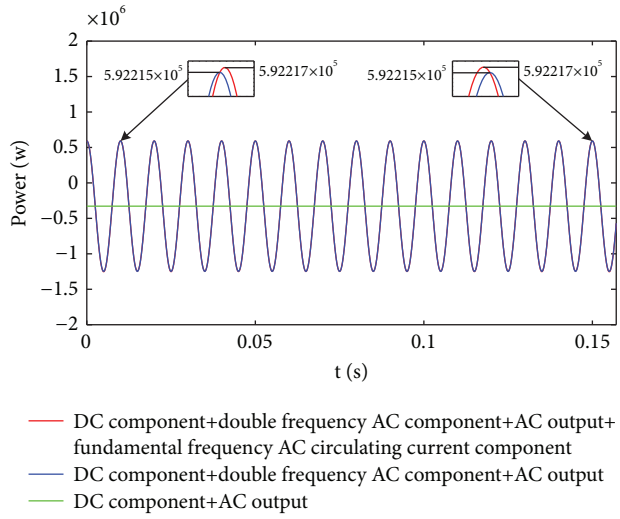


Figure 6: Power difference between upper and lower bridge arms.

reactive power of the main circuit of the MMC, adjusted it by the PI controller, and generated the three-phase sinusoidal modulation wave after feedforward decoupling. The generated three-phase sinusoidal modulation wave was sent to the carrier phase-shifting modulation through the correction of the three-level SOC equalization control and worked with the submodule capacitor voltage quicksort algorithm to generate the triggering pulse of the power switch of each half-bridge submodule of the MMC-BESS main circuit. The Bidirectional DC-DC converter adopted the double closed-loop control system structure of the outer loop voltage and inner loop current based on the PI controller to realize the energy interaction between the MMC and the lithium battery of the energy storage submodule.

### 3.1. MMC-BESS Main Control System

*3.1.1. MMC-BESS Mathematical Model of Single-Phase Equivalent Circuit.* Based on the analysis of the internal characteristics of the phase unit and the bridge arm unit, in order to achieve effective control and interaction of the AC and DC-side energy, the MMC-BESS phase unit was used as a "bridge" to establish the AC and DC-side voltage/current relationship. The single-phase equivalent circuit is shown in

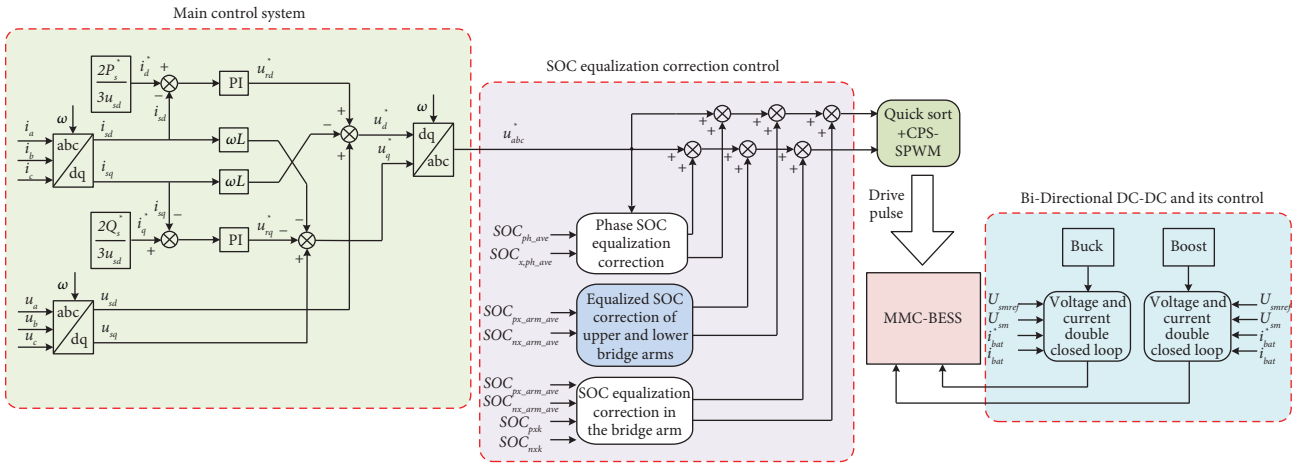


Figure 7: MMC-BESS hierarchical control system.

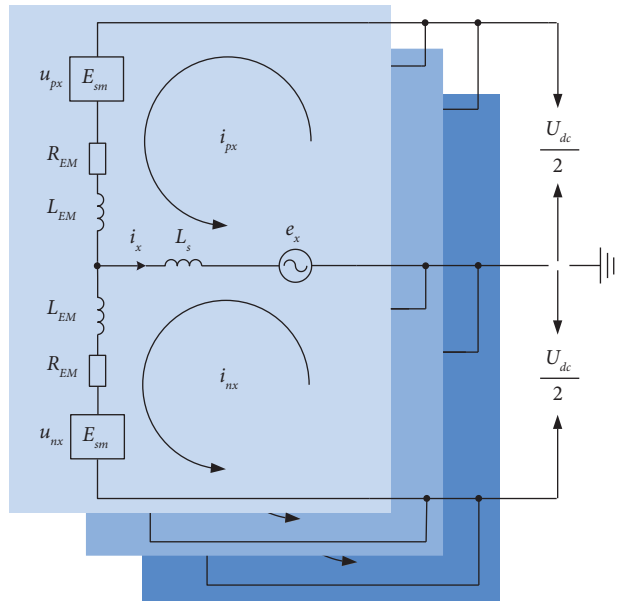


Figure 8: MMC-BESS single-phase equivalent circuit model.

Figure 8, taking phase A as an example for description. The expressions are as follows:

$$\begin{cases} L_{Em}\dfrac{\mathrm{d}i_{pa}}{\mathrm{d}t} + R_{Em}i_{pa} + L_s\dfrac{\mathrm{d}i_a}{\mathrm{d}t} = \dfrac{U_{\mathrm{dc}}}{2} - e_a - u_{pa}, \\ L_{Em}\dfrac{\mathrm{d}i_{na}}{\mathrm{d}t} + R_{Em}i_{na} - L_s\dfrac{\mathrm{d}i_a}{\mathrm{d}t} = \dfrac{U_{\mathrm{dc}}}{2} + e_a - u_{na}, \end{cases} \tag{11}$$

$$\begin{cases} i_{pa} = \dfrac{I_{dc}}{3} + \dfrac{i_a}{2}, \\ i_{na} = \dfrac{I_{dc}}{3} - \dfrac{i_a}{2}. \end{cases} \tag{12}$$

From equations (11), the following equation can be obtained:

$$\left(L_s + \frac{L_{Em}}{2}\right)\frac{\mathrm{d}i_a}{\mathrm{d}t} + \frac{R_{Em}}{2}i_a = \frac{u_{na} - u_{pa}}{2} - e_a. \tag{13}$$

According to (13), the AC-side current can be changed by controlling the bridge arm voltage difference.

In order to facilitate the design of the control system, (13) can be extended to the three-phase expression, which can be transformed by $abc/\mathrm{d}q$ transformation matrix $M(\theta)_{abc\text{-}\mathrm{d}q}$ from the three-phase static coordinate system to the two-phase rotating coordinate system. Thus, the following equations can be obtained:

$$\begin{cases} P_s^* = \dfrac{3}{2}Ei_d^*, \\ \\ Q_s^* = -\dfrac{3}{2}Ei_q^*. \end{cases} \tag{14}$$

*3.1.2. Structure and Principle of Main Control System.* The main control system of the MMC-BESS is shown in Figure 9. Firstly, according to the instantaneous active/reactive power theory, the active/reactive power reference values $P_S^*$ and $Q_S^*$ are transformed to obtain the current reference values of axes $d$ and $q$, namely, $i_d^*$ and $i_q^*$.

Secondly, the three-phase AC currents $i_a$, $i_b$ and $i_c$ are transformed by abc/dq coordinates to realize the separation of active and reactive power, and then, $i_{sd}$ and $i_{sq}$ are obtained. The reference value voltages $u_{rd}^*$ and $u_{rq}^*$ of axes $d$ and $q$ are obtained after making the difference with the actual value based on the PI control. According to (14), in order to accelerate the operation of the system and remove the voltage/current coupling on AC side of axes $d$ and $q$, a feedforward decoupling is added. The three-phase AC voltages $u_a$, $u_b$ and $u_c$ were transformed by $abc/\mathrm{d}q$ coordinates to obtain $u_{sd}$ and $u_{sq}$, which were combined with coupling currents of $u_{rd}^*$ and $u_{rq}^*$ of axes $d$ and $q$ to complete the feedforward decoupling to obtain the ideal voltage value of $u_d^*$ and $u_q^*$ of axes $d$ and $q$. Finally, the three-phase AC voltage modulation waveform was obtained through $\mathrm{d}q/abc$ inverse coordinate transformation.

*3.2. The Bidirectional DC-DC Converter and Its Control.* The energy storage system consists of the energy storage battery and the Bidirectional DC-DC converter. The Bidirectional DC-DC converter adopted PI-based double closed-loop control of outer loop voltage/inner loop current. The actual value of the inner loop current was the inductor current of the Bidirectional DC-DC converter, which was controlled to stabilize the power balance of each energy storage submodule. The actual value of the outer loop voltage was the capacitor voltage of the energy storage submodule, which was controlled to stabilize the capacitor voltage of the submodule.

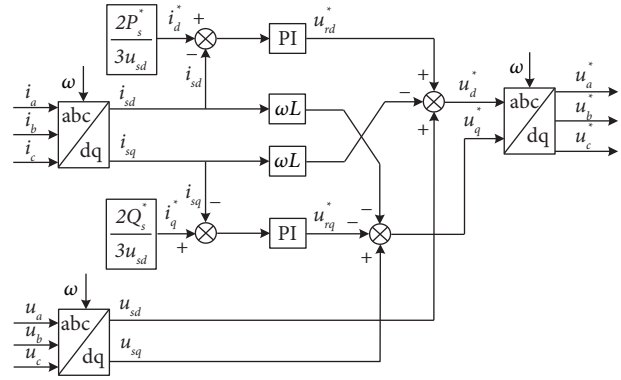


Figure 9: MMC-BESS main control system.

The structure of the Bidirectional DC-DC converter control system is shown in Figure 10. The difference between the reference value $U_{\mathrm{smref}}$ and the actual value $U_{\mathrm{sm}}$ of each phase of the energy storage submodule capacitor voltage is obtained after PI tracking control, thus obtaining the reference value of the inductor current of the energy storage system. Then, the difference is made with the actual value $i_{\mathrm{bat}}$. The loop PI is adjusted and compared with the carrier to generate the PWM pulse signals. The switching between the Buck and the Boost mode needs to set conditions. In the control system, when the reference value of inductor current is multiplied by −1, the Bidirectional DC-DC works in the Boost mode.

Taking Boost as an example, the stability analysis of the control system is carried out, and the constructed double closed-loop transfer function is

$$G(s) = \frac{G_{PI_1}(s).G_{PI_2}(s)}{1 + G_{PI_1}(s)\cdot G_{PI_2}(s) + G_{PI_2}(s)\cdot C_m s + L_{\mathrm{bat}}C_m s^2}. \tag{15}$$

The transfer function structure and the system Bode diagram of the double closed-loop control system of the outer loop voltage and inner loop current based on PI control are shown in Figures 11 and 12, respectively.

In the transfer function, $P_1$, $P_2$ and $P_3$ are the forward channel loop composed of the half-bridge submodule capacitor voltage $U_{\mathrm{sm}}$, the filter inductor current of energy storage system $i_{\mathrm{bat}}$ and the difference between the lithium battery voltage $U_{\mathrm{bat}}$ and $U_{\mathrm{sm}}$. The specific expressions are as follows:

$$\begin{cases} P_1 = -G_{PI_1}(s)\cdot G_{PI_2}(s)\cdot \dfrac{1}{L_{\mathrm{bat}}C_m s^2}, \\ \\ P_2 = -G_{PI_2}(s)\cdot \dfrac{1}{L_{\mathrm{bat}}s}, \\ \\ P_3 = -\dfrac{1}{L_{\mathrm{bat}}C_m s^2}. \end{cases} \tag{16}$$

In (15) and (16) and Figure 11, the expressions of $G_{PI_1}(s)$ and $G_{PI_2}(s)$ in frequency domain are $k_{p1} + k_{i1}/s$ and $k_{p2} + k_{i2}/s$. In this paper, $k_{p1} = 10$, $k_{i1} = 0.5$, $k_{p2} = 5$ and

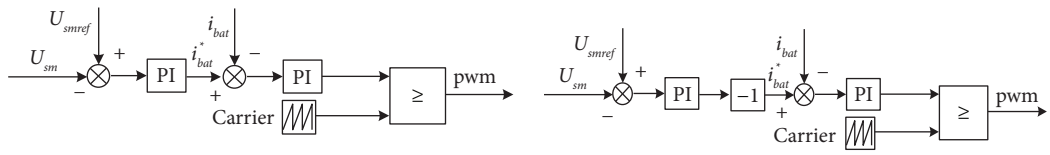


Figure 10: Bidirectional DC-DC control system.

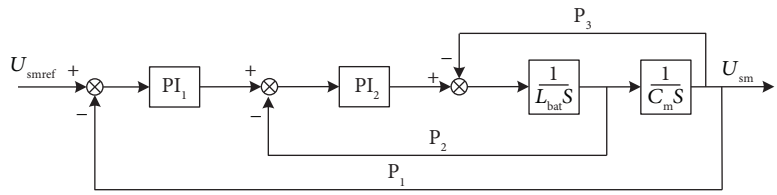


Figure 11: Transfer function structure of the bidirectional DC-DC double closed-loop control system.

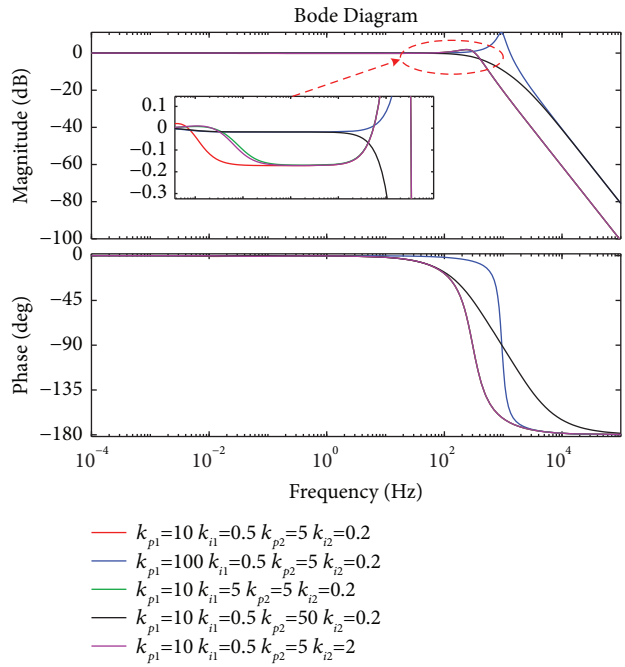


Figure 12: Comparison of amplitude phase frequency characteristics of bidirectional DC-DC double closed-loop control system.

$k_{i2} = 0.2$ are taken as basic variables. One variable is changed and expanded by 10 times each time, and the other three variables remain unchanged. A group of system Bode diagram curves are drawn, as shown in Figure 12. After analysis and comparison, $k_{p1} = 100$, $k_{i1} = 0.5$, $k_{p2} = 5$ and $k_{i2} = 0.2$ are finally selected. The resonant peak frequency of the double closed-loop control system constructed by this group of variables is about 3184 Hz, and the switching frequency of the Bidirectional DC-DC converter in this paper is 10 kHz. It shows that the switching frequency signal greater than the resonant peak frequency is well suppressed under the high current and rapid charge and discharge condition of the lithium battery in the energy storage system, and the capacitor voltage signal of the submodule less than the resonant peak frequency will complete the zero static error tracking of its ideal input value after passing through the control system.

*3.3. SOC Equalization Correction Control.* The essence of the SOC equalization correction control of the MMC-BESS is to perform power correction on the three phases, upper and lower bridge arms, and their submodules, respectively. Firstly, through the analysis of the three-level SOC equalization control process, the feedforward sliding window integral method was introduced into the upper and lower bridge arm control layer to form a more accurate equalization correction, so as to make full use of the lithium battery capacity of the energy storage submodule.

*3.3.1. Phase-To-Phase SOC Equalization Correction Control.* In order to effectively correct the DC current components in the three-phase MMC-BESS, during the SOC balance correction control of the phase unit, the PI adjustment method is used to realize the zero-static-error tracking of the average

SOC of each-phase submodule to the average SOC of the three-phase submodule.

The specific phase equalization control structure is shown in Figure 13. The average SOC of lithium battery of each energy storage submodule in phase $X$ is $\mathrm{SOC}_{x,\ \mathrm{ph\_ave}}$, and the average SOC of lithium battery of the three-phase energy storage submodule is $\mathrm{SOC}_{\mathrm{ph\_ave}}$. The mathematical expression is as follows:

$$\begin{cases} \mathrm{SOC}_{x,ph\_\mathrm{ave}} = \dfrac{\sum_{k=1}^{2N} \mathrm{SOC}_{x,k}}{2N}, \\ \mathrm{SOC}_{ph\_\mathrm{ave}} = \\ \dfrac{\mathrm{SOC}_{a,ph\_\mathrm{ave}} + \mathrm{SOC}_{b,ph\_\mathrm{ave}} + \mathrm{SOC}_{c,ph\_\mathrm{ave}}}{3}. \end{cases} \tag{17}$$

*3.3.2. SOC Equalization Correction Control of Upper and Lower Bridge Arms Based on Feedforward Sliding Window Integral*

$$\begin{cases} \mathrm{SOC}_{px\_\mathrm{arm\_ave}} = \dfrac{\sum_{k=1}^{N} \mathrm{SOC}_{pxk}}{N}, \\ \mathrm{SOC}_{nx\_\mathrm{arm\_ave}} = \dfrac{\sum_{k=1}^{N} \mathrm{SOC}_{nxk}}{N}. \end{cases} \tag{18}$$

It can be seen from formula (18) that the DC circulating current has the same effect on the power of the upper and lower bridge arms, and the power flow can be adjusted among the three phases. In order to obtain more accurate power distribution of the power of the upper and lower bridge arms, the upper and lower bridge arm correction factor $h_{\mathrm{cps}\_x}$ and the feedforward sliding window integral are introduced. As shown in Figure 14, the correction factor $h_{\mathrm{cps}\_x}$ contains the DC component, the fundamental frequency AC component, and other frequency AC components, which are multiplied by $e_{aref}$ and go through the sliding window integral to obtain the equalization correction of the upper and lower bridge arms $U^{*}_{\mathrm{arm\_cps}}$ containing only the fundamental frequency and a small amount of AC component of other frequencies. The filtering integral process is as follows:

$$\int_{t}^{t+T} \sin(\omega t) \cdot \left[ A\sin(\omega t) + \sum_{k'=2}^{\infty} B_{k'} \cdot \sin\left(k'\omega t + \varphi_{k'}\right) \right] dt. \tag{19}$$

Both $T$ in (19) and $Z^{-N}$ in Figure 14 represent the delay, with the delay time being 0.2 s, and the minimum filtering frequency is 5 Hz.

*3.3.3. SOC Equalization Correction Control in Bridge Arms.* The SOC equalization correction control of the lithium battery of each submodule in the bridge arms is the same as the interphase SOC equalization correction control. Making the difference between the average value of the SOC of the lithium battery of the upper and lower bridge arm energy storage submodule and the actual value of the lithium battery of each submodule, the zero-static-error tracking of both through the PI controller was realized. When the MMC-BESS is in discharging condition, the Bidirectional DC-DC worked in the Boost mode. If the SOC value of the lithium battery was large, the discharging current would increase; if the SOC value was small, the discharging current would decrease. Under charging conditions, the Bidirectional DC-DC is switched to the Buck mode, and if the SOC value of the lithium battery was small, the charging current would increase; if the SOC was large, the charging current would be reduced.

Eventually, the working state modulation commands of each submodule of the MMC-SCESS were modified and acted on each of the three-phase bridge arms and their submodules, respectively, so that the phase-to-phase power and the power of upper and lower bridge arms was corrected, and then it was combined with the quicksort algorithm of the submodule capacitor voltage, thus quickly balancing the capacitor voltage of each phase submodule. Based on this, the double frequency circulating current among phases was suppressed, and the system loss was reduced, as shown in Figure 15.

## 4. Simulation

In order to verify the effectiveness of the proposed three-level SOC equalization correction control strategy based on the feedforward sliding window integral method, a three-phase five-level MMC-BESS model was constructed in the Matlab/Simulink environment. The parameters are shown in Table 2. Due to the limitation of the computer system performance, the number of submodules of the upper and lower bridge arms was set to 4 in the simulation verification. In practical applications, due to the scalability of the MMC-BESS, more input submodules could jointly withstand the DC voltage of 20 kV on the DC side of each phase unit. This paper focuses on the following three aspects under the discharging state of lithium battery energy storage system: (1) the sudden change of DC-side load, aiming at stabilizing the DC bus voltage; (2) the two-phase drop of the three-phase grid-side voltage and the three-phase current balance compensation capability; (3) a faster equalization convergence speed of the SOC of each phase of the proposed three-level SOC equalization correction control strategy under the above two working conditions.

As shown in Figures 16–18, in the first working condition, the DC load increased suddenly at 0.5 s after the system was started. In order to quickly stabilize the DC bus voltage and maintain power balance, the MMC-BESS input the lithium battery and the three-level SOC balance correction controller. The Bidirectional DC-DC of the MMC-BESS energy storage system worked in the Boost mode, and the lithium battery continued to discharge. When the load changed suddenly, the DC voltage was 19800 V and finally stabilized at 20 kV. In the second working condition, after the first working condition lasted for 0.5 s, at 1 s, the DC load recovered, the three-phase grid-side voltages $B$ and $C$

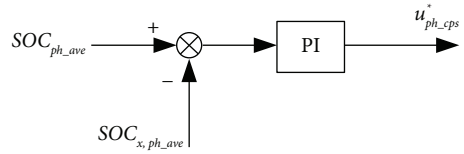


Figure 13: Phase-to-phase SOC equalization correction control.

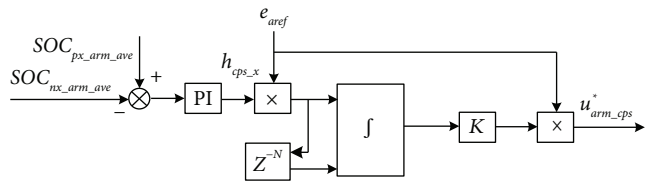


Figure 14: Equalization correction control of upper and lower bridge arms.

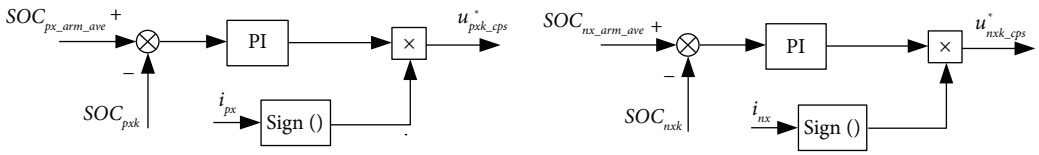


Figure 15: SOC equalization correction control of submodules in bridge arms.

Table 2: System simulation parameters.

| Parameters | Value |
|---|---|
| The number of bridge arm submodules of each phase n | 4 |
| Rated capacity $S$/MVA | 5 |
| Grid phase voltage $E_j$/kV | 5.7 |
| DC-side voltage $U_{dc}$/kV | 20 |
| Bridge arm filter inductor $L_{Em}$/mH | 2 |
| Submodule capacitor $C_m$/mF | 4.7 |
| Grid-side filter inductor $L_S$/mH | 4 |
| DC/DC inductor $L_{bat}$/mH | 3 |
| Switching frequency $f$/Hz | 1000 |

dropped by 50%, and the peak phase voltage changed from 8000 V to 4000 V. The Bidirectional DC-DC of the MMC-BESS energy storage system still worked in the Boost mode, and the lithium battery continued to discharge to compensate for the difference of the three-phase power, so that the three-phase grid-side current increased and balanced. The DC bus voltage was stable at about 20 kV, the maximum variable was 1500 V, and the steady-state error was 7.5%. The maximum peak value of the three-phase current was 231.9 A, the effective value of the three-phase average current was 160.96 A, and the unbalance degree was 0.024. The parameters are shown in Table 3. The total harmonic distortion rate of the three-phase current is shown in Figure 19. Five power frequency cycles after 5.66 s were selected for measurement, and the total harmonic distortion rate was 1.38%.

The MMC-BESS acted as a bridge for energy conversion between the AC side, the DC side, and the energy storage battery. The stability of the capacitor voltage of submodule of each phase could prove the stability of the power input and output during the energy conversion period. The stability of the submodule capacitor voltage could not only reduce the double frequency circulation formed by the pressure difference between the phases of the MMC-BESS, but also reduce the circulating current in the upper and lower bridge arms formed by the fluctuation of the submodule capacitor voltage in the bridge arms of each phase.

Under the same operating condition, when the three-phase grid-side voltage dropped by 50%, the maximum capacitor voltage of the submodule of the $c$-phase upper and lower bridge arm before the improvement by using the one-third average method was 5009 V, and the minimum was 4991 V. The maximum capacitor voltage of the submodule of the improved c-phase upper bridge arm was 5008 V, and the minimum was 4992 V. In the range of 0.5 s to 9 s, the SOC equalization correction control strategy proposed in this paper and the three-stage SOC equalization correction control strategy using one-third average method were compared and analyzed with the total harmonic distortion rate of capacitor voltage of each submodule of phase $C$ with 50 Hz as the fundamental frequency. It could be seen from the comparative analysis of Figure 20 and Table 4 that the total harmonic distortion rate of capacitor voltage of the submodule of c-phase lower bridge arm with the two methods is less than that of the upper bridge arm. For the same submodule, the total harmonic distortion rate of the capacitor voltage of the submodule using the method proposed in this paper is less than that of the same submodule using the one-third average method. It indirectly proved that the MMC-BESS using the SOC equalization correction control strategy proposed in this paper has more average phase-to-phase power distribution and more accurate power distribution of upper and lower bridge arms.

It can be seen from (10) and (11) that when the capacitor voltage fluctuation and total harmonic distortion rate of the submodule were smaller, the difference between the phase-

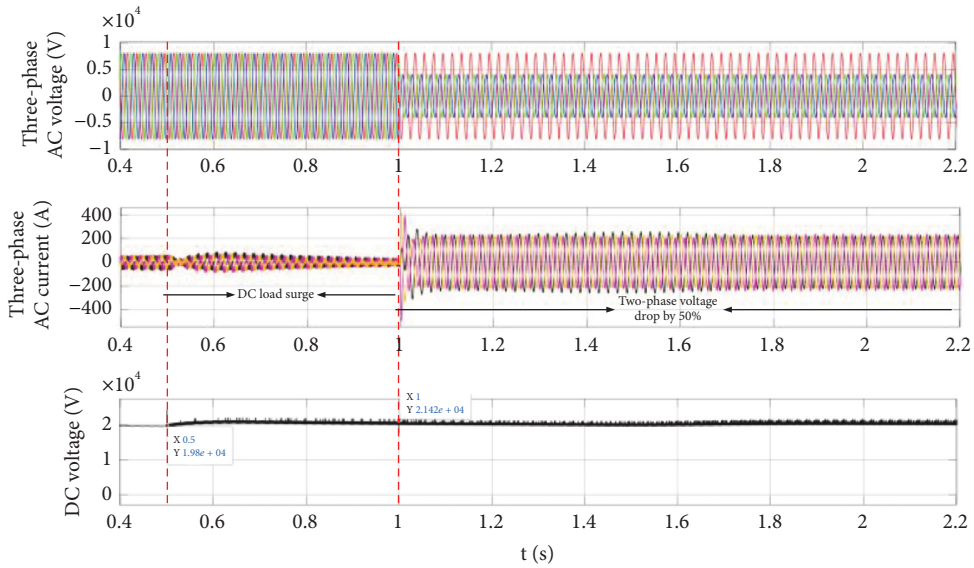


Figure 16: System three-phase voltage/current and DC voltage at 0.4 ~ 2.2 s.

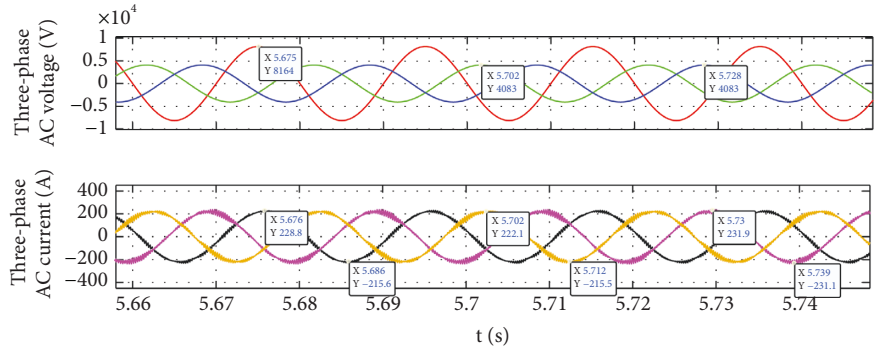


Figure 17: Three-phase AC voltage and current at 5.66 s ~ 5.76 s.

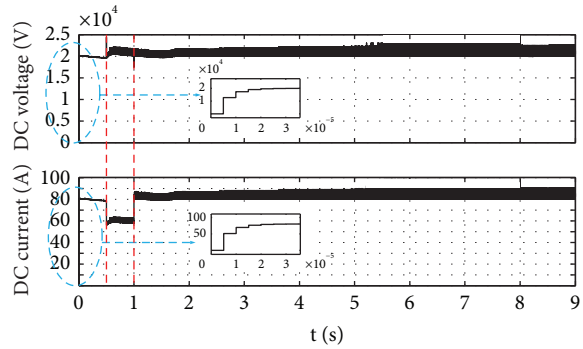


Figure 18: DC-side voltage and current at 0 ~ 9 s.

to-phase power of the system and the power of the upper and lower bridge arms of each phase should be smaller, so the three-phase circulating current should also be smaller. The reduction of the three-phase circulating current of the system was helpful in improving the efficiency of the MMC-BESS. Figure 21 shows the three-phase circulating current of the system using the two methods. The results showed that after the system was stable, under the working conditions with the load sudden change and two-phase voltage drop, the two methods could effectively suppress the three-phase circulating current, but the effect of using feedforward sliding window integral method on circulating current suppression was more obvious, and the peak value of circulating current was smaller. The maximum peak values of

Table 3: Unbalance degree parameters of three phases.

| Phases $x$ | Current peak of three phases (A) | Current effective value of three phases (A) | Average value of effective value of three-phase current (A) | Differential phase current (effective value of phase current - average value of effective value of three-phase current) (A) | Three-phase current unbalance degree (max effective value of differential phase current divided by average value of effective value of three-phase current) |
|---|---|---|---|---|---|
| $A$-phase | 228.8 | 161.81 | 160.96 | 0.85 | 2.4% |
| $B$-phase | 222.1 | 157.07 | | 3.89 | |
| $C$-phase | 231.9 | 164.00 | | 3.04 | |

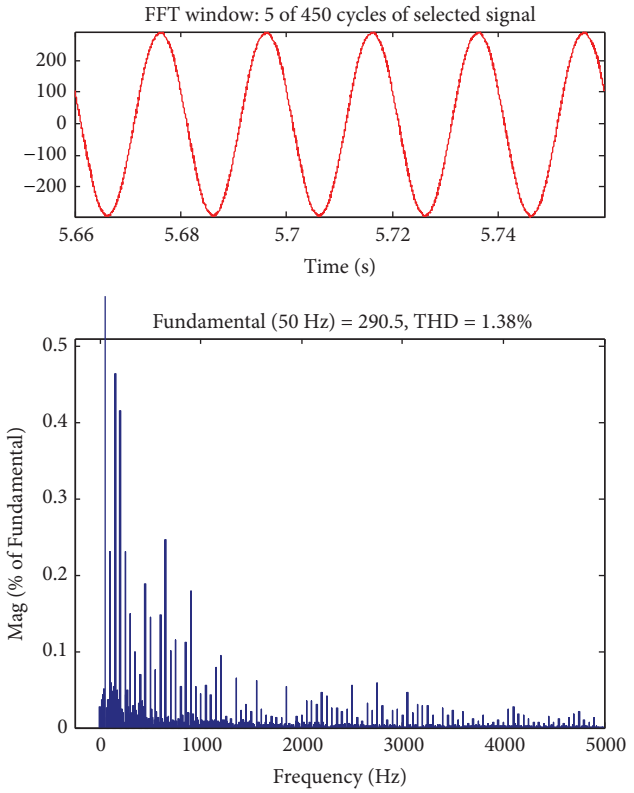


Figure 19: Three-phase grid-side current THD at 5 s.

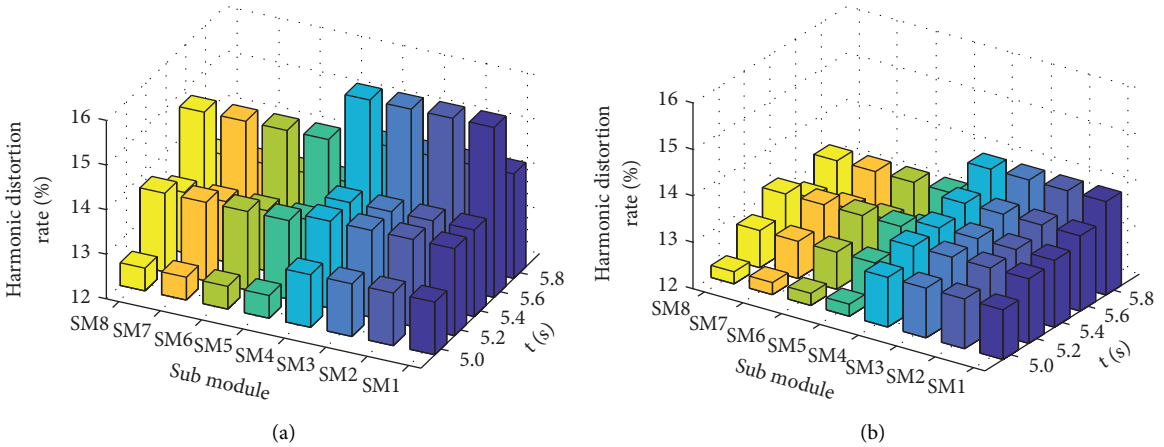


Figure 20: Analysis of harmonic distortion rate of capacitor voltage of $c$-phase submodule. (a) Harmonic distortion rate of each submodule using one-third average method. (b) Harmonic distortion rate of each submodule of sliding window integral method.

Table 4: Capacitor voltage distortion rate of *c*-phase submodule using one-third average method and sliding window integral method.

| Harmonic distortion rate of capacitor voltage of submodule | | | | | |
|---|---|---|---|---|---|
| One-third average method: | | | | | |
| | 5 s | 5.2 s | 5.4 s | 5.6 s | 5.8 s |
| Upper bridge arm of phase *C* (sm1 ~ sm4) | 13.18% | 13.95% | 13.94% | 15.81% | 14.34% |
| Lower bridge arm of phase *C* (sm5 ~ sm8) | 12.51% | 13.76% | 13.35% | 14.72% | 13.34% |
| Sliding window integral method: | | | | | |
| | 5 s | 5.2 s | 5.4 s | 5.6 s | 5.8 s |
| Upper bridge arm of phase *C* (sm1 ~ sm4) | 13.07% | 13.39% | 13.49% | 13.62% | 14.01% |
| Lower bridge arm of phase *C* (sm5 ~ sm8) | 12.26% | 12.80% | 13.24% | 12.81% | 13.26% |

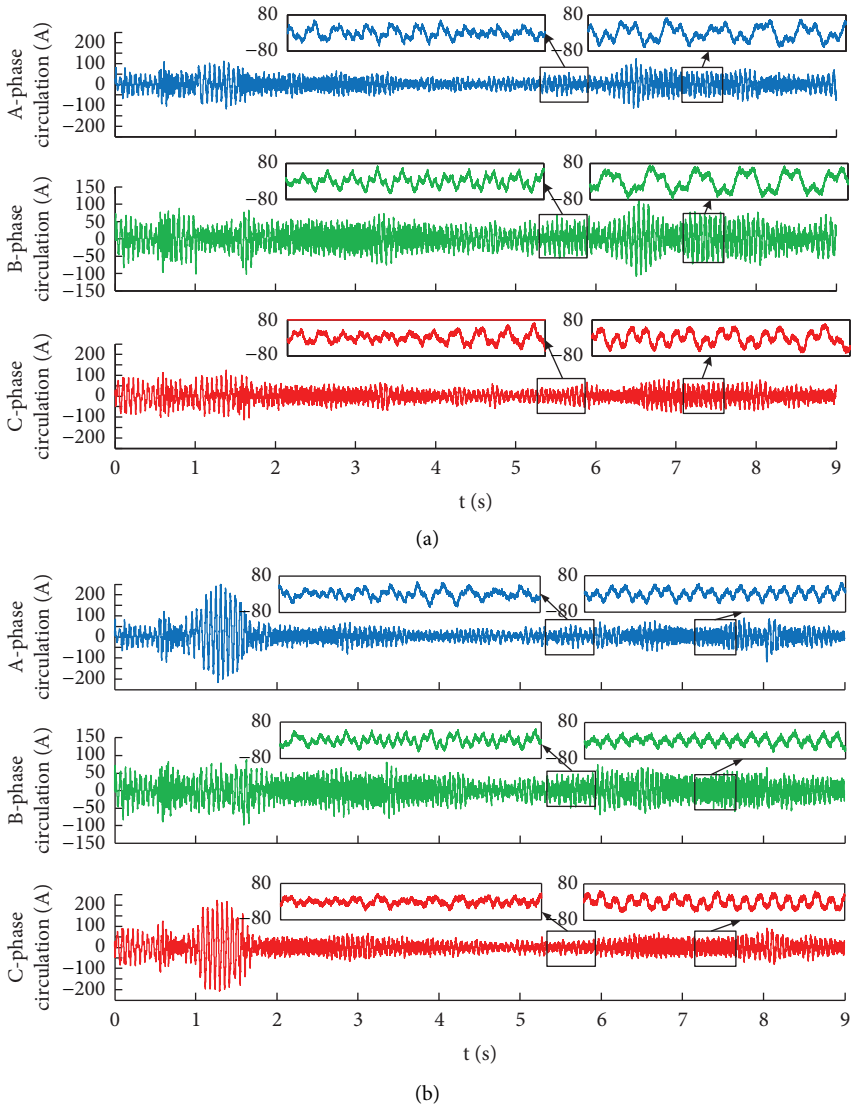


Figure 21: MMC-BESS three-phase circulation. (a) One-third average method, MMC-BESS three-phase circulation. (b) Sliding window integral method, MMC-BESS three-phase circulation.

three-phase circulation of *A*, *B*, and *C* using one-third average method were 123.3 A, 107.7 A, and 81.2 A, respectively. After the improvement, the maximum peak values of the three-phase circulation of *A*, *B*, and C using feedforward sliding window integral method were 85.83 A, 73.91 A, and 70.01 A, respectively.

Figure 22 shows the output power of three-phase battery: the DC load increased suddenly at 0.5 s. With the goal of stabilizing the DC bus voltage, the battery is discharged rapidly, and the maximum output power of the battery is $7.5 \times 10^6$ W. When the three-phase grid-side voltage was unbalanced, in order to compensate for the power difference

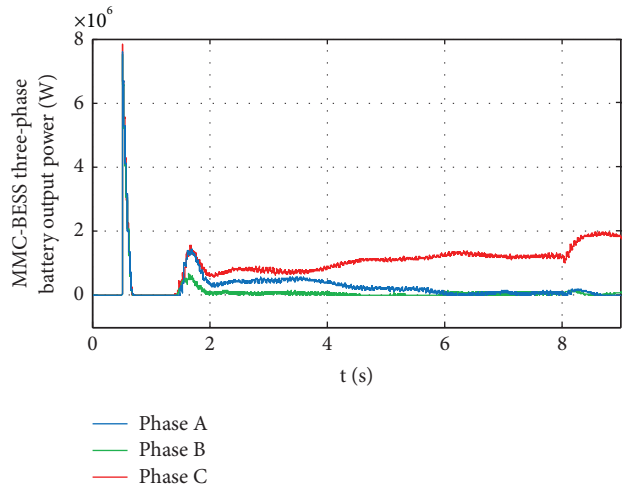


Figure 22: MMC-BESS three-phase battery output power.

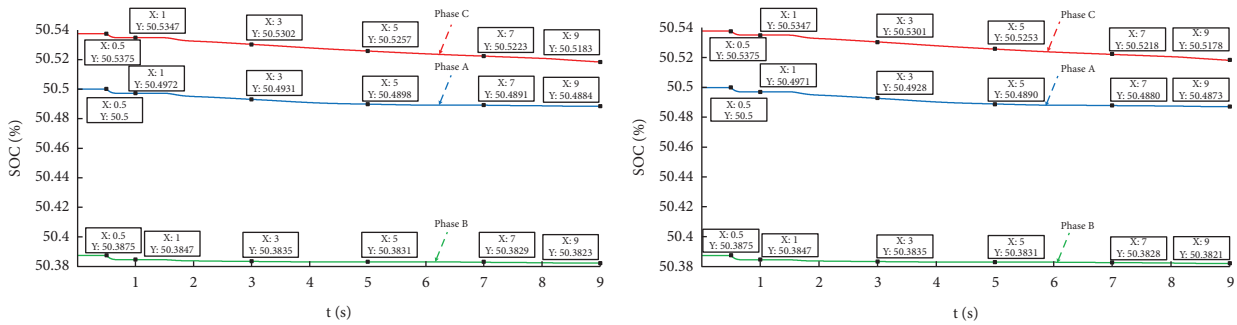


Figure 23: MMC-BESS three-phase SOC average. (a) One-third average method, three-phase SOC average. (b) Sliding window integral method, three-phase SOC average.

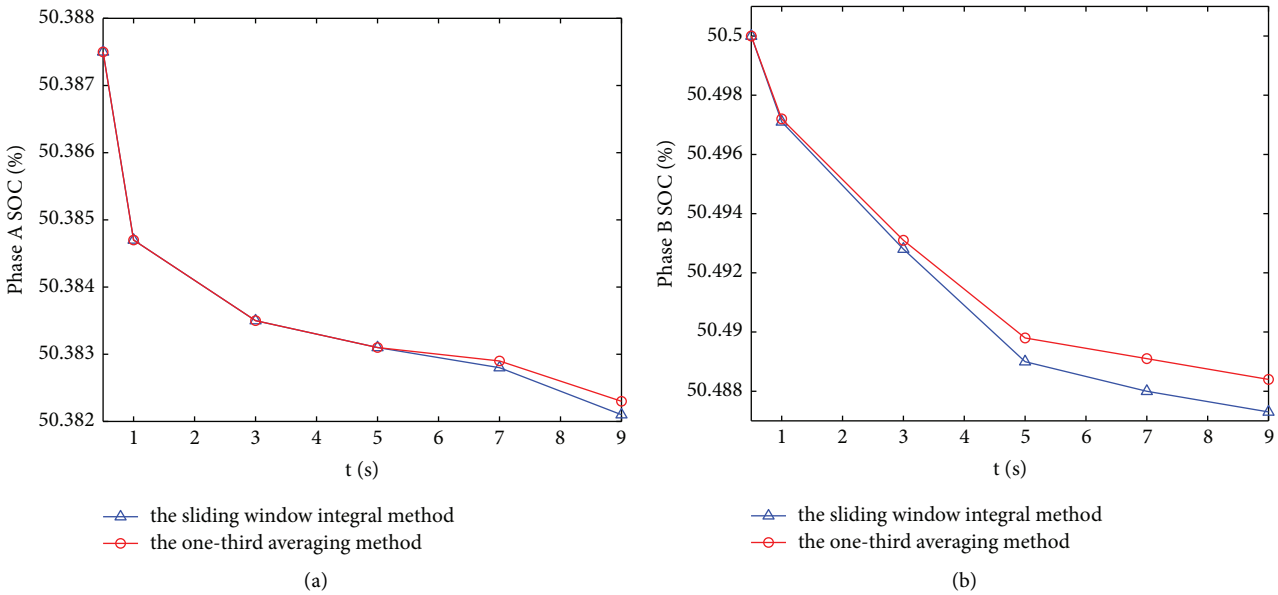


Figure 24: Continued.

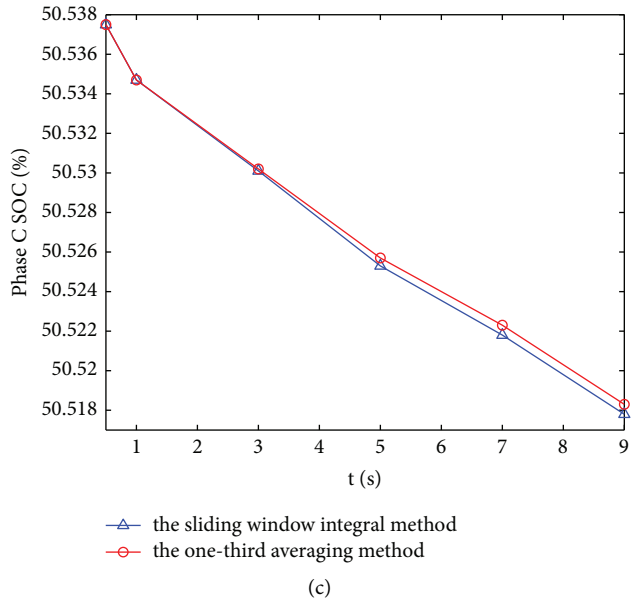


(c)

Figure 24: SOC average value of three phases of the MMC-BESS. (a) Sliding window integral method of phase *A*, SOC average using one-third average method. (b) Sliding window integral method of phase *B*, SOC average using one-third average method. (c) Sliding window integral method of phase *C*, SOC average using one-third average method.

Table 5: Comparison of SOC data between one-third average method and sliding window integral method.

| Comparison of SOC data | | | | | | |
|---|---|---|---|---|---|---|
| One-third average method: | | | | | | |
| | 0.5 s | 1 s | 3 s | 5 s | 7 s | 9 s |
| Phase *A* | 50.5000 | 50.4972 | 50.4930 | 50.4898 | 50.4891 | 50.4884 |
| Phase *B* | 50.3875 | 50.3847 | 50.3834 | 50.3831 | 50.3829 | 50.3823 |
| Phase *C* | 50.5375 | 50.5347 | 50.5302 | 50.5257 | 50.5223 | 50.5183 |
| Sliding window integral method: | | | | | | |
| | 0.5 s | 1 s | 3 s | 5 s | 7 s | 9 s |
| Phase *A* | 50.5000 | 50.4971 | 50.4928 | 50.4890 | 50.4880 | 50.4873 |
| Phase *B* | 50.3875 | 50.3847 | 50.3835 | 50.3831 | 50.3828 | 50.3821 |
| Phase *C* | 50.5375 | 50.5347 | 50.5301 | 50.5253 | 50.5218 | 50.5178 |

among the three phases, the three-phase current can be quickly balanced. The lithium battery of the submodule of the MMC-BESS three-phase energy storage was continuously discharged, but the three-phase output was uneven. In order to quickly balance lithium battery of the SOC of each phase under the condition of uneven three-phase output and improve the utilization rate and service life of energy storage capacity, it was necessary to balance the SOC of the lithium battery of each energy storage submodule in the three phases of MMC-BESS.

In order to verify the effectiveness of the control strategy proposed in this paper, the system has been put into the three-level SOC equalization correction controller after a sudden change in DC load at 0.5 s. Figures 23 and 24 and Table 5 compare the equalization correction control proposed in this paper with the equalization correction control of the one-third average method. Under the same initial value of SOC, by comparing the results of the final SOC value of each phase at the same moment, it could be seen that the correction control proposed in this paper had a faster convergence and equalization speed. Using one-third average method, the initial values of the SOC of phases *A*, *B*, and *C* are 50.5000, 50.3875, and 50.5375, respectively; the final values of the SOC of phases *A*, *B*, and *C* are 50.4884, 50.3823, and 50.5183, respectively; the difference of the SOC of phases *A*, *B*, and *C* is 0.0116, 0.0052, and 0.0192, respectively. Using the sliding window integral method, the initial values of SOC of the phases *A*, *B*, and *C* are the same, and the final difference is 0.0127, 0.0054, and 0.0197, respectively.

## 5. Conclusion

In this paper, the characteristics of MMC-BESS phase unit power and the power difference between the upper and lower bridge arms are analyzed, a three-level SOC equalization correction control strategy is constructed, and a feedforward sliding window integral link is introduced into

the equalization correction control layer of the upper and lower bridge arms, so as to weaken the influence of the fundamental frequency AC circulating current and DC circulating current caused by the capacitor voltage fluctuation of the submodule on system. A three-phase 5-level MMC-BESS simulation model is built in the Matlab/Simulink environment. The results show that:

(1) When the DC load changes suddenly, or the three-phase network side voltage is unbalanced, the DC bus voltage has good stability, the maximum fluctuation is 1500 V, and the steady-state error is 7.5%;

(2) MMC-BESS has good compensation ability for three-phase network side current when the two-phase voltage drops by 50%. After compensation, the THD of three-phase current is 1.38%, and the unbalance degree is 2.4%. The system has strong robustness;

(3) The effectiveness of the three-stage SOC equalization correction control strategy with sliding window integral method proposed in this paper is verified, and the SOC of each phase lithium battery has a faster equalization convergence speed.

## Data Availability

The datasets used and analyzed during the current study are available from the corresponding author upon reasonable request.

## Conflicts of Interest

The authors declare that they have no conflicts of interest.

## Acknowledgments

This work was supported by the scientific research project of the Shaanxi Provincial Department of Education, under Grant 17JK0337.

## References

[1] Z. Y. He, "Discussion on harmonic hot issues of distributed new energy integration into power grid," *Southern Power Grid Technology*, vol. 10, no. 03, pp. 47–52+5, 2016.

[2] X. W. Ma, H. C. Xu, X. Liu et al., "A test method for the fast frequency response function of new energy stations in the northwest transmission-end large power grid," *Power grid technology*, vol. 44, no. 04, pp. 1384–1391, 2020.

[3] X. S. Tang and H. Y. Lu, "The influence of wind power flexible DC grid connection and frequency modulation control on power angle stability of power system," *Proceedings of the Chinese Society for Electrical Engineering*, vol. 37, no. 14, pp. 4027–4035+4281, 2017.

[4] J. L. Li, X. D. Yuan, Z. G. Yu, and L. Ge, "A review of research on using energy storage systems to improve power quality of power grids," *Automation of Electric Power Systems*, vol. 43, no. 08, pp. 15–24, 2019.

[5] N. Mukherjee Mukherjee and D. Strickland Strickland, "Analysis and comparative study of different converter modes in modular second-life hybrid battery energy storage systems," *IEEE Journal of Emerging and Selected Topics in Power Electronics*, vol. 4, no. 2, pp. 547–563, 2016.

[6] S. Wang, L. Jing, X. Z. Wu, J. Li, W. Wu, and J. Jiang, "Distributed control strategy for modular multi-level energy storage converters," *Automation of Electric Power Systems*, vol. 42, no. 12, pp. 113–121, 2018.

[7] L. Guo, H. Liang, and W. G. Zhang, "State-of-charge control strategy of battery energy storage system based on modular multilevel converter," *Power System Technology*, vol. 41, no. 08, pp. 2688–2697, 2017.

[8] I. Trintis, S. Munk-Nielsen, and R. Teodorescu, "A new modular multilevel converter with integrated energy storage," *IEEE Transactions on Industrial Electronics*, vol. 62, no. 2, pp. 1034–1046, 2011.

[9] Y. Chen, H. Wang, M. Zhu, M. Liu, J. Ma, and X. Cai, "Three-port modular multilevel converter based on hybrid sub-modules and full-leg inductance: simplified modeling and grid interconnection control strategy," *China Electrical Engineering Journal*, vol. 42, no. 5, 2021.

[10] S. Y. Li, T. Wu, B. Ren, Y. Xu, and C. Yuan, "Overview of energy storage systems based on modular multilevel converters," *Power System Protection and Control*, vol. 43, no. 16, pp. 139–146, 2015.

[11] A. A. Taffese, A. G. Endegnanew, S. D'Arco, and E. Tedeschi, "Power oscillation damping with virtual capacitance support from modular multilevel converters," *IET Renewable Power Generation*, vol. 14, no. 5, pp. 897–905, 2020.

[12] Q. Song, J. W. Meng, Y. B. Zhou, S. Xu, L. Yang, and K. Wang, "MMC's capacitor voltage ripple effect and its influence on the optimal design of converters [J/OL]," *Power Grid Technology*, vol. 45, no. 11, 2021.

[13] Q. Fan, X. B. Zhao, C. Y. Zhao, and J. Xu, "Adaptive fault current limiting control strategy for modular multilevel converters," *Automation of Electric Power Systems*, vol. 45, no. 17, pp. 126–133, 2021.

[14] Q. F. Yang, Y. B. Huang, M. X. Shi, J. Zhou, X. Chen, and J. Wen, "Distributed control method of multi-group optical storage units in DC microgrid based on consensus algorithm," *Proceedings of the Chinese Society for Electrical Engineering*, vol. 40, no. 12, pp. 3919–3928, 2020.

[15] Q. Chen, L. H. Zhang, Y. J. Wu, D. Gao, and Y. Zou, "Research on SOC equalization strategy of energy storage MMC converter," *Electrical Measurement and Instrumentation*, vol. 57, no. 05, pp. 37–43, 2020.

[16] N. Li, F Gao, T. Hao, Z. Ma, and C. Zhang, "SOH balancing control method for the MMC battery energy storage system," *IEEE Transactions on Industrial Electronics*, vol. 65, no. 8, pp. 6581–6591, 2018.

[17] J. I. Y. Ota, T. Sato, and H. Akagi, "Enhancement of performance, availability, and flexibility of a battery energy storage system based on a modular multilevel cascaded converter (MMCC-SSBC)," *IEEE Transactions on Power Electronics*, vol. 31, no. 4, pp. 2791–2799, 2016.

[18] T. Soong and P. W. Lehn, "Assessment of fault tolerance in modular multilevel converters with integrated energy storage," *IEEE Transactions on Power Electronics*, vol. 31, no. 6, pp. 4085–4095, 2016.

[19] M. Mao, Y. Ding, L. Chang et al., "Multi-objective power management for EV fleet with MMC-based integration into smart grid," *IEEE Transactions on Smart Grid*, vol. 10, no. 2, pp. 1428–1439, 2019.

[20] S. Wang, L. Jing, X. Z. Wu, and X. Zhao, "MMC-based SOC balance control of energy storage system," *Power Electronics*, vol. 50, no. 11, pp. 60–62+90, 2016.

[21] L. Zhang, F. Gao, and N. Li, "Control strategy of MMC battery energy storage system under asymmetrical grid voltage condition," *Chinese Journal of Electrical Engineering*, vol. 2, no. 2, pp. 76–83, 2016.

[22] H. B. Tao, X. F. Yang, Z. J. Li, Q. Zheng, X. You, and P. Kobrle, "MMC-based supercapacitor energy storage system and its improved SOC balance control strategy in electric energy routers," *Power System Technology*, vol. 43, no. 11, pp. 3970–3978, 2019.

[23] J. G. Li, W. B. Yang, Q. Song, Y. Huang, and W. Liu, "Distributed equalization control method of modular multilevel converter capacitor voltage," *Automation of Electric Power Systems*, vol. 40, no. 17, pp. 197–203, 2016.

[24] Y. L. Yu, Y. H. Xu, and X. B. Liu, "Harmonic current detection method of sliding window iterative DFT," *Power System Protection and Control*, vol. 39, no. 13, pp. 78–82+90, 2011.

[25] Y. N. Wang, C. Y. Guo, S. Yang, B. Pang, and X. Lin, "Non-monotonic variation characteristics and mechanism analysis of MMC system stability margin with inner loop current control bandwidth," *Proceedings of the Chinese Society for Electrical Engineering*, vol. 42, no. 10, 2021.

Hindawi
Shock and Vibration
Volume 2022, Article ID 1236971, 11 pages
https://doi.org/10.1155/2022/1236971

*Research Article*

# A Composite Method of Marine Shafting's Fault Diagnosis by Ship Hull Vibrations Based on EEMD

**Xiaofei Wen**,[1] **Wenjie Meng**,[1] **Xiaoxiao Sun**,[2] **and Ruiping Zhou**[3]

[1]*School of Naval Architecture and Maritime, Zhejiang Ocean University, Zhoushan, China*
[2]*State Key Laboratory of Navigation and Safety Technology, Shanghai Ship and Shipping Research Institute, Shanghai, China*
[3]*School of Naval Architecture Ocean and Energy Power Engineering, Wuhan University of Technology, Wuhan, China*

Correspondence should be addressed to Xiaofei Wen; wenxiaofei@zjou.edu.cn

Received 10 February 2022; Revised 27 February 2022; Accepted 4 March 2022; Published 30 March 2022

Academic Editor: Liu Jing



The fault diagnosis is always a key issue in the security field of marine propulsion system. There are obvious problems like the unsteady working of sensors, distortion of original data, and ambivalent feature information from marine shafting's vibration or motion. It is therefore critical to develop a more effective method to identify the fault information so that the safety of marine propulsion system can be pre-estimated. Hence, a composite method which is based on the ensemble empirical mode decomposition (EEMD) and coupled with the autocorrelation method (AM), the fast Fourier transform (FFT), is mixed and applied to identify the fault information of marine shafting during its operating by hull vibration. The contrastive analysis of the three methods and fault feature study are then conducted to assess the effectiveness of the proposed method thoroughly and validated by the author previously. The research indicates that the composite method is available to fault diagnosis of marine shafting by hull vibration which coupled the shafting vibration with fault feature.

## 1. Introduction

As indispensable "links" of ship propulsion torque and thrust transmissions, the ship propulsion shafting system is the key part of a ship. Marine propulsion shafting mainly consists of propeller, intermediate shaft, intermediate bearing, thrust shaft, thrust bearing, stern tube, stern tube bearing and other devices as shown in details in Figure 1. Ship propulsion shafting are affected by some external loads or periodic excitations, such as propeller excitation [1], main engine excitation, wave loads, engine room environmental vibration loads, and so on. During ship navigating, it perhaps happens that the bearings serious wear phenomena derived from the oscillations and whirl of the oil film. The shafting vibration coupled fault information can be transferred constantly to ship hull by the oil film of bearings. The effective extracting fault information is the key work that has drawn much attention of many researchers all around the world. In 2010, Jayaswal P., Verma S. N. et al. [2] investigated the fault diagnosis methods for vibration signals by combining wavelet transform with neural networks and fuzzy logic. In 2016, Khang H. V. et al. [3] used windowed Fourier transform to clearly identify fault characteristic frequencies in time spectrums. Especially, Huang N. E. Reference [4], Zhaohua W. [5], et al. proposed an Empirical Mode Decomposition (EMD) method and ensemble empirical mode decomposition (EEMD), which are now widely used in fault diagnosis. Then the methods were combined and applied to identify the preset bearing failure modes of benches [6], to extract fault features from vibration signals [7], to reduce noise [8] and analyze fault diagnosis of rotating machinery [9] or rolling bearing [10–16]. In 2011, Zhou T. T. [17] proposed a method of partial ensemble empirical mode decomposition (PEEMD) for fault diagnosing of marine shafting for the first time. Then Chen Y [18] and He Y [19] used the envelope analysis method with spectrum kurtosis (SK) to identify marine shafting vibrations. And the above methods certainly are available in fault diagnosing, but the signal is usually limited to vibration sources such as the bearings or shaft, not the hull. Therefore

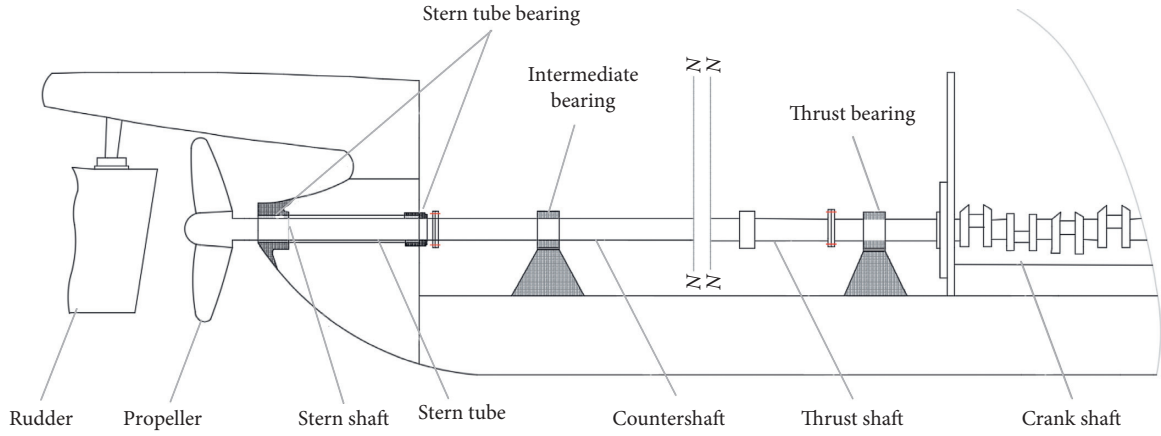


Figure 1: Diagram of marine propulsion shafting.

a Composite method is proposed and applied to identify the marine shafting's fault from the hull vibration, and some simulations and real ship tests are carried out in this paper.

## 2. Methodology

*2.1. Empirical Mode Decomposition.* EMD methods can be applied to decompose the signal adaptively to the series of intrinsic mode functions (IMF) of the frequency components which distributes from high frequency to low frequency. Each IMF component contains different characteristic in time domain which can represent the real physical information of the signals. The two IMF conditions need to meet during decomposing process [20]: the number of extreme value is equal to zero value in the original signal, and the up-envelope curve and down-envelope curve is symmetrical to time axis in whole time domain. The decomposing process is shown as follows:

*Step 1.* The cubic spline curve is adopted to draw the up-envelope curve and down-envelope curve of vibration signal, then the maximum and minimum of them are extracted to calculate the mean $m_1$. The first IMF component is restructured as follows.

$$h_1 = x(t) - m_1. \tag{1}$$

Here, $h_1$ is the first IMF component, $x(t)$ is the original vibration signal, $m_1$ is the mean value of s1 and s2 which are respectively the up-envelope curve and down-envelope curve of the vibration signal drawn by connecting the local maximum point and local minimum point with a cubic spline curve.

*Step 2.* If $h_1$ does not meet the IMF conditions, smoothing process will be done and $h_1$ will be used as the original data as following. $h_{12}$ is the result of repeating the second smoothing process.

$$h_{12} = h_1 - m_{11}. \tag{2}$$

Here, $m_{11}$ is the mean of up-envelope curve and down-envelope curve of $h_1$. The smoothing step will be done continually until the result meet the IMF conditions. So the $h_{1k}$ can be got finally, which becomes the first IMF component and is denoted by $c_1$ .

$$c_1 = h_{1k} = h_{1(k-1)} - m_{1(k-1)}, \quad (k > 1 \text{ and } k \in N), \tag{3}$$

where $k$ is the times of repeating smoothing process.

*Step 3.* When $c_1$ is separated from the original signal, the first residual function $r_1$ is left as equation (4).

$$r_1 = x(t) - c_1. \tag{4}$$

Then the similar smoothing process will be used to get the next residual function until the final residual function is a monotonic function as (4).

$$r_n = r_{n-1} - c_{n-1}, \quad (n > 1, n \in N). \tag{5}$$

Lastly, the signal can be expressed as following function by EMD method.

$$x(t) = \sum_{i=1}^{n} c_i + r_n. \tag{6}$$

*2.2. Ensemble Empirical Mode Decomposition.* EMD methods can decompose original signals into a series of intrinsic mode functions (IMF) and a residual component, and which has the adaptability, orthogonality and completeness. Otherwise EMD method still has some theoretical problems like endpoint effecting, mean curve construction, and mode mixing. Hence, EEMD method was composite to curb modal aliasing phenomena. A flow chart of the EEMD method is illustrated in Figure 2, and the details are as follows:

(i) Step 1: add the random Gaussian white no ise $n_i(t)$ to the original vibration signal $x(t)$, so the noise-added signal $x_i(t)$ can be obtained as follows:

$$x_i(t) = x(t) + n_i(t) i = 1, 2, \ldots, M, \tag{7}$$

where the subscript **i** is the serial number, $M$ is the ensemble number.

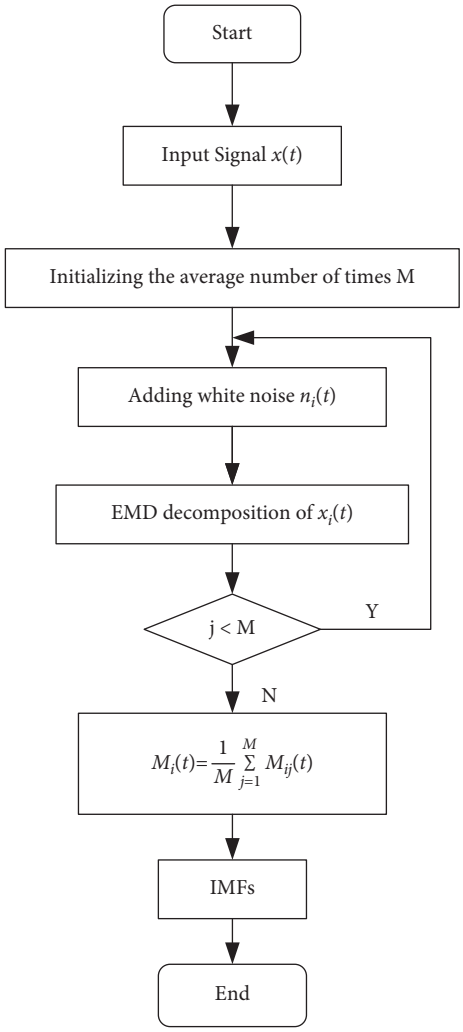


Figure 2: Decomposing process of EEMD.

(ii) Step 2: according to equation (7), the matrix of noise-added signal can be expressed as $[x_1(t), x_2(t), \ldots, x_M(t)]$ $(i = 1, 2, \ldots, M)$,. Then the EMD is adopted to decompose the noise-added signal $x_i(t)(i = 1, 2, \ldots, M)$ and the IMF components are obtained which can be described as $\{x_{1,i}(t), x_{2,i}(t), \ldots, x_{n,i}(t)\}^T$. So the matrix $M$ with $j$ time of Gaussian white noise can be expressed as equation (8).

$$M = \begin{bmatrix} x_{1,1}(t), & x_{1,2}(t), & \ldots & x_{1,M}(t), \\ x_{2,1}(t), & x_{2,2}(t), & \ldots & x_{2,M}(t), \\ \vdots & \vdots & \vdots & \vdots \\ x_{n,1}(t), & x_{n,2}(t), & \ldots & x_{n,M}(t), \end{bmatrix}. \quad (8)$$

(iii) Step 3: the ensemble means of the corresponding IMF components then is calculated by the equation (9), so the final result of that signal can be obtained more effectively.

$$M_j(t) = \frac{1}{M}\sum_{i=1}^{M} M_{ij}(t), \quad i = 1, 2, \ldots, n; \; j = 1, 2, \ldots, m. \quad (9)$$

*2.3. Autocorrelation Method.* The autocorrelation functions describe the dependence of the same sample functions of random vibrations between different instantaneous amplitudes. The expressions of the autocorrelation functions of discrete random vibration signals can be derived as follows:

$$R_{xx}(t) = \frac{1}{N}\sum_{i=1}^{N-k} x(i)x(i+k), \quad (k = 0, 1, 2, \ldots), \quad (10)$$

where $R_{xx}(t)$ represents the autocorrelation function, $x(i)$ is the sample function, $k$ is the serial number which belong to the natural number. And the autocorrelation function is described in (10).

$$R_{xx}(k\Delta t) = R_{xx}(\tau). \quad (11)$$

Here, $\tau$ is value of the time domain, $\Delta t$ denotes the interval time of sampling. For the autocorrelation functions, the maximum value is $R_{xx}(0)$ when $\tau = 0$ and the minimum approaches to zero when $\tau \longrightarrow \infty$. So the value of autocorrelation function is limited in the range of zero and $R_{xx}(0)$.

Autocorrelation functions are one of the important parameters of stochastic vibration signal analysis. They also reflect the degrees of smoothness and steepness of a waveform. Therefore, autocorrelation functions are often used to detect periodic vibration components from a random vibration signal contains in the practical engineering project. The autocorrelation functions of periodic components will maintain the original periodic without attenuation and it can be applied to qualitatively analyze the fault features of marine shafting from hull vibration which is also periodic.

*2.4. Method Developing.* In fact, the fault signals of marine shafting system are characterized with periodicity and can easily be overwhelmed by strong background noise, so it is difficult to identify fault information accurately in measured signals. The composite method combines the ensemble empirical mode decomposition (EEMD) innovatively, the autocorrelation method (AM), and the fast Fourier transform (FFT), which is abbreviated as EEAF. The EEAF has displayed good adaptability, orthogonality, and completeness in our research. In its analysis process, the measured signals are first decomposed by the EEMD method and the original signals with some strong background noise are decomposed to a series of IMF components. That also improves effectively the ratio of signal-to-noise for the periodic components. Then, autocorrelation analysis is done for obtaining the autocorrelation function of each IMF component, which is applied to determine the periodicity of IMF components. Finally, the frequencies and amplitudes of the periodic signals can be effectively extracted from the IMF components with periodic signals by filtering, excluding and spectrum analysis. The process of EEAF is shown in Figure 3 and is divided into the following steps.

(i) Step 1: the decomposing of the measured original signal by EEMD is performed, which is presented in Chapter 2.2 previously. And the IMF components are obtained.

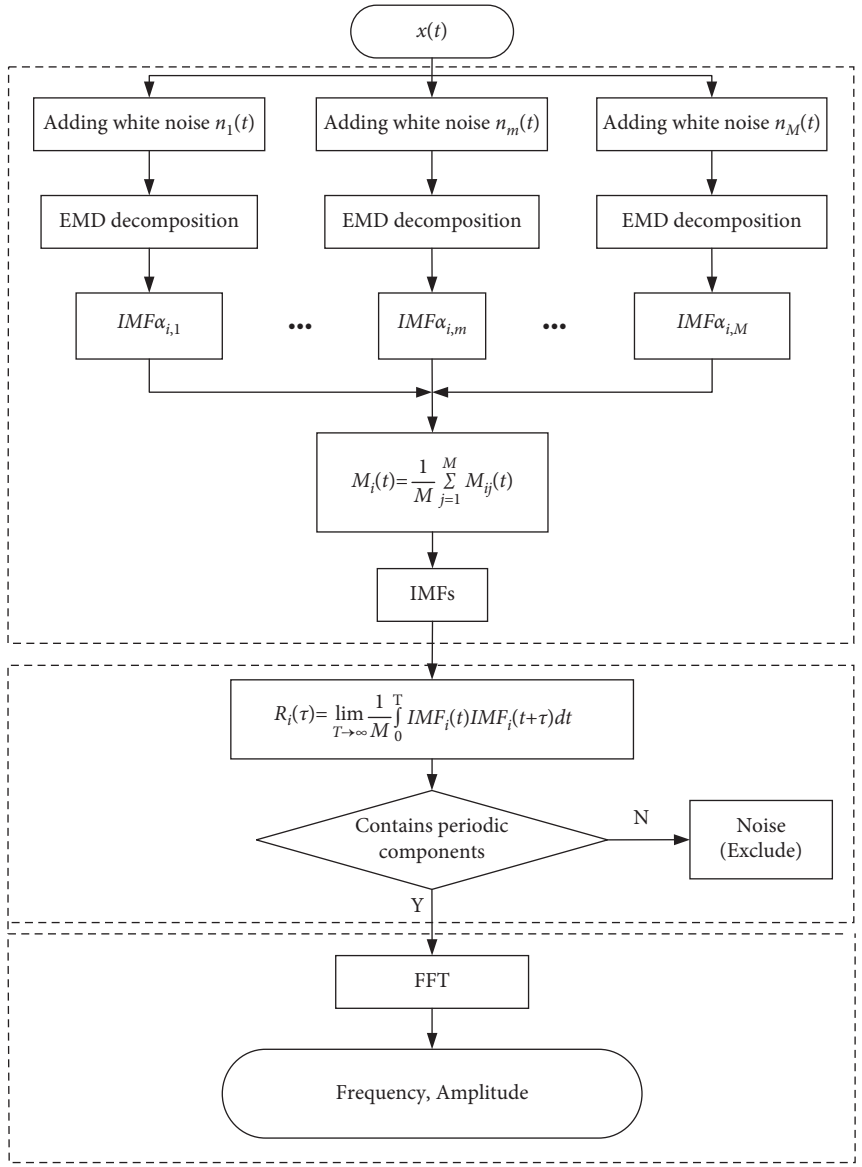


Figure 3: Decomposing process of the EEAF.

(ii) Step 2: to construct the autocorrelation function $R_i(\tau)$ of the IMF components as equation (12).

$$R_i(\tau) = \lim_{T\longrightarrow\infty} \frac{1}{T}\int_0^T x_i(t)x_i(t+\tau)dt\ , \tag{12}$$

where $T$ is the period time of IMF component. For discrete signals, (11) can be transformed into the following:

$$R_i(n\Delta t) = \frac{\sum_{i=0}^{N-n} x_i(t_i)x(t_i+n\Delta t)}{N-n}, \tag{13}$$

where $N$ represents the length of the related data, $n$ denotes the number of delays, $i$ is the time serial number; $\tau$ indicates the delay timed. The $R_i(n\Delta t)$ can be used to eliminate the random disturbance noise with aperiodic features, and identify the IMF components with periodic features.

(iii) Step 3: the IMF components with periodicity are extracted by FFT analysis. The periodic component characteristic quantities in the IMF components such as frequencies and amplitudes, can be obtained.

## 3. Numerical Verification

The followed case is done to verify the EEAF method. The designated signal is composed of the periodic components and random environmental noise, which can be expressed as the following equation.

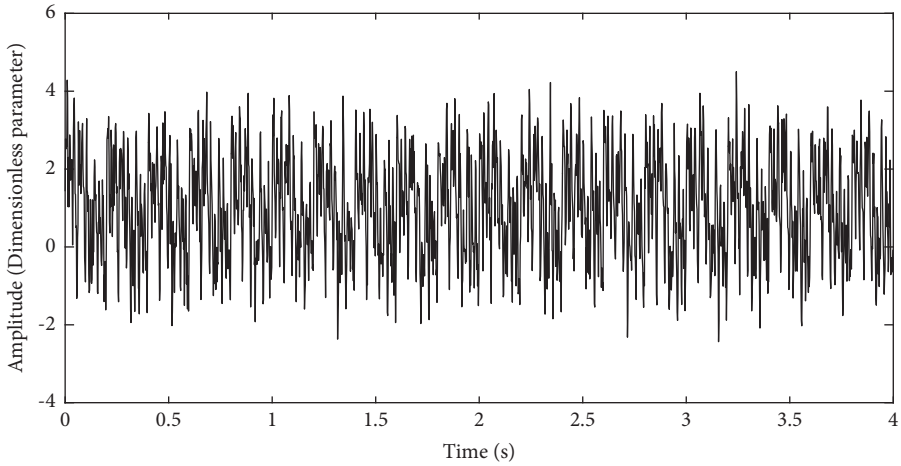


Figure 4: The waveform of the designated signal in time domain.

$$\begin{cases} s = s_1 + s_2 + s_3 + s_4 + s_5 + s_0, \\ s_1 = 0.6\ \sin(10\pi t), \\ s_2 = 0.6\ \sin(30\pi t), \\ s_3 = 0.8\ \sin(60\pi t), \\ s_4 = \sin(100\pi t), \\ s_5 = 0.6\ \sin(200\pi t), \end{cases} \tag{14}$$

where $s_0$ is the random Gaussian white noise, $s_1$, $s_2$, $s_3$, $s_4$ and $s_5$ are five different periodic functions. The random Gaussian white noise has an amplitude standard deviation of 0.2, and the ensemble number is set as $M = 100$. So the waveform of the designated signal is shown in Figure 4.

Through the EEMD method, the modes and residual components are extracted and shown in Figure 5. The designated signal has been decomposed to nine IMF components and one residual component. Then select the IMF component with periodic feature to avoid confusion, the autocorrelation analysis of nine IMF components are conducted. The results are shown in Figure 6. In Figure 6, the autocorrelation functions of IMF1, IMF2, IMF3, IMF4, and IMF5 are periodic obviously, and they have retained the original periodicity without attenuation. Subsequently, they are retained and used for the further analysis. However, the autocorrelation function waveforms of the remaining components have obvious periodicity, but disordered. The effect of Gaussian white noise plays a main factor of the result, and it should be eliminated.

Finally, the five IMF components with periodicity, IMF1, IMF2, IMF3, IMF4, and IMF5, are transformed by the fast Fourier transform. The feature quantities of IMF component such as frequency and amplitude are extracted. The frequency domain of the five IMF components is presented in Figure 7, in which the preset frequencies (100 Hz, 50 Hz, 30 Hz, 15 Hz and 5 Hz) are successfully recognized. Furthermore, the amplitudes corresponding to the five frequencies are obtained, those are 0.62162, 0.986, 0.7856, 0.5932, and 0.5829 respectively. To compare the data of Table 1, the extracted frequencies are exactly the same as the preset frequencies, but there are little changes in amplitude observed with the values for both within a 3% error range because of the slight confusion. In summary, the EEAF method is available to extract the periodic component with fault feature through the case study.

## 4. Test and Discussion

In actual ship, the complexity of the hull vibrations are much greater than that of the analog signals. The test is done in a 64000DWT bulk carrier, whose total length is 199.90 m, the length between perpendicular lines is 194.5 m, the molded width is 32.26 m, and the molded depth is 18.50 m. In addition, its design draft, deadweight and design speed are 11.30 m, 63,800 ton, 15.60 knot respectively. During sea trial of this ship, the temperature of the stern bearings rises rapidly to 87°C, and a high temperature alarm is raised (Note: the alarm value is set at 60°C). So the abnormal wear of the stern bearings occurs. For analyzing the reason of the fault, the test is done. In the test of hull vibration, test datum of eight steady operating conditions (33.0 r/min, 41.1 r/min, 42.0 r/min, 49.1 r/min, 50.0 r/min, 51.0 r/min, 55.1 r/min, and 56.0 r/min) are collected in consequence. The sampling frequency of the measuring instrument is set at 512 Hz, and the sampling time is 60 seconds. The eight sensors of vibration are arranged on the tail seal plate and the stiffening plates on both sides, as illustrated in Figure 8. No.3 sensor and No.4 sensors are used to gather the longitudinal vibrations of hull, No.7 sensor and No.10 sensors are applied to collect the transverse vibrations of hull, other sensors are for hull's vertical vibrations.

*4.1. Vertical Vibration.* In the current study, the vertical vibration test data of the hull stern structure are collected by four vibration sensors, namely the No. 5, 6, 8, and 9 observation points, as shown in Figure 9. The four sensors of hull vertical vibration are symmetrically arranged on the stiffening plates of two hull sides. So the vibration data

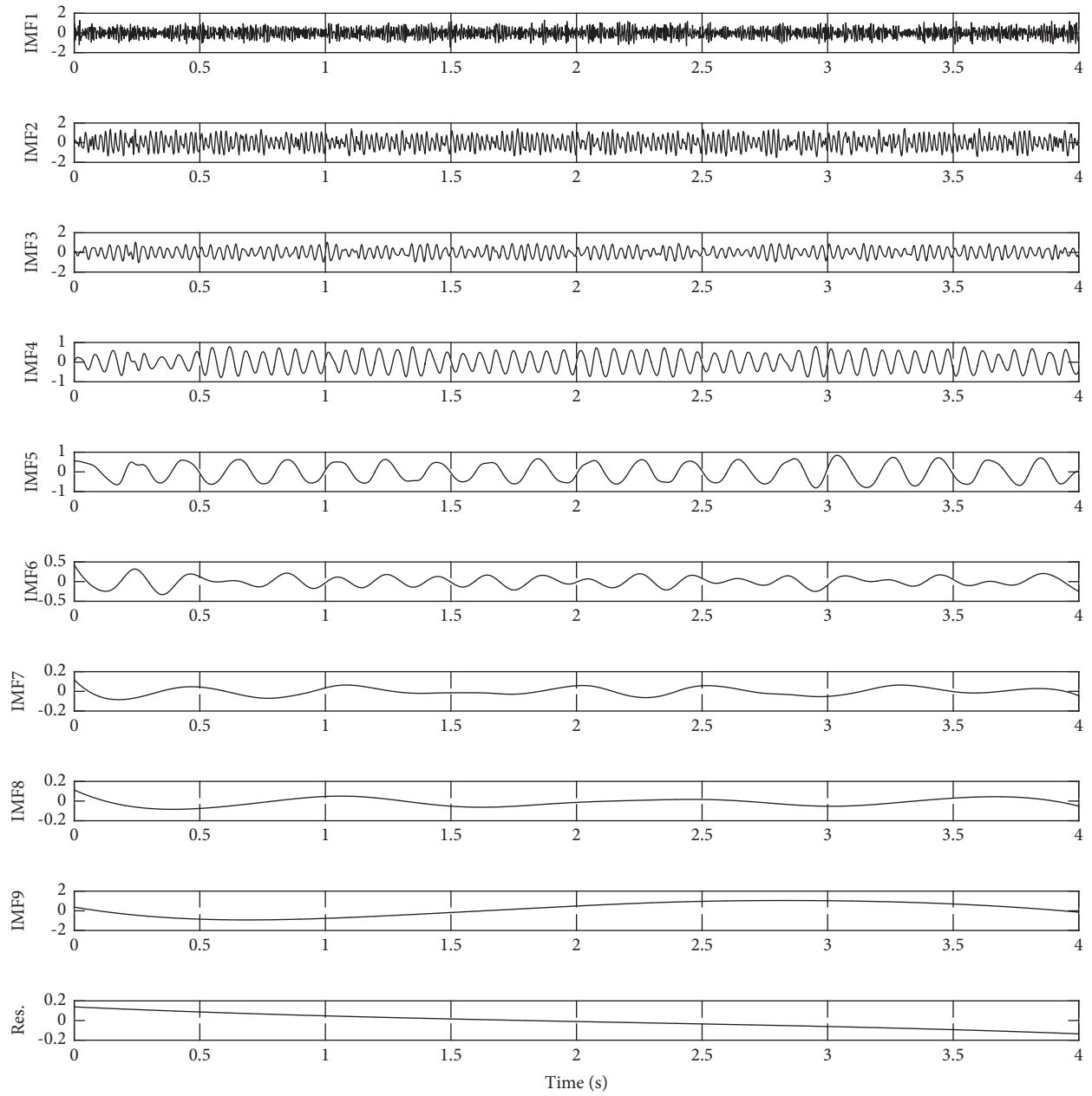


Figure 5: Waveforms of IMF components and residual components.

of the No. 5 and No. 6 are analyzed through the EEAF method. The main quantities coupled in the hull vertical vibrations with periodicity are obtained, as detailed in Table 2. The data show that there are slight differences in the frequencies of the vibration data collected from the two measuring points. However, the deviations are less than 5%. Furthermore the data of Table 2 are used to draw the curves of frequency and amplitude in Figure 9. In Figure 9(a), the frequencies of hull vertical vibrations are distributed mainly in 5th order line and 2nd order trend line. The amplitudes of hull vertical vibrations are shown in Figure 9(b), and the amplitudes of the 5th order vibration signals present a trend of increasing, decreasing and then increasing again. The phenomena happens in some ships with misalignments of marine propulsion shafting. That is to say, the amplitude of hull vertical vibration in 5th order increases with the increase of the shaft speed. Therefore, it indicates that the propulsion shafting of this ship is misaligned.

*4.2. Longitudinal Vibration.* The data from the sensors of No. 3 and No. 4 are the signals of hull longitudinal vibration. Similar to the aforementioned processes, an EEAF method is

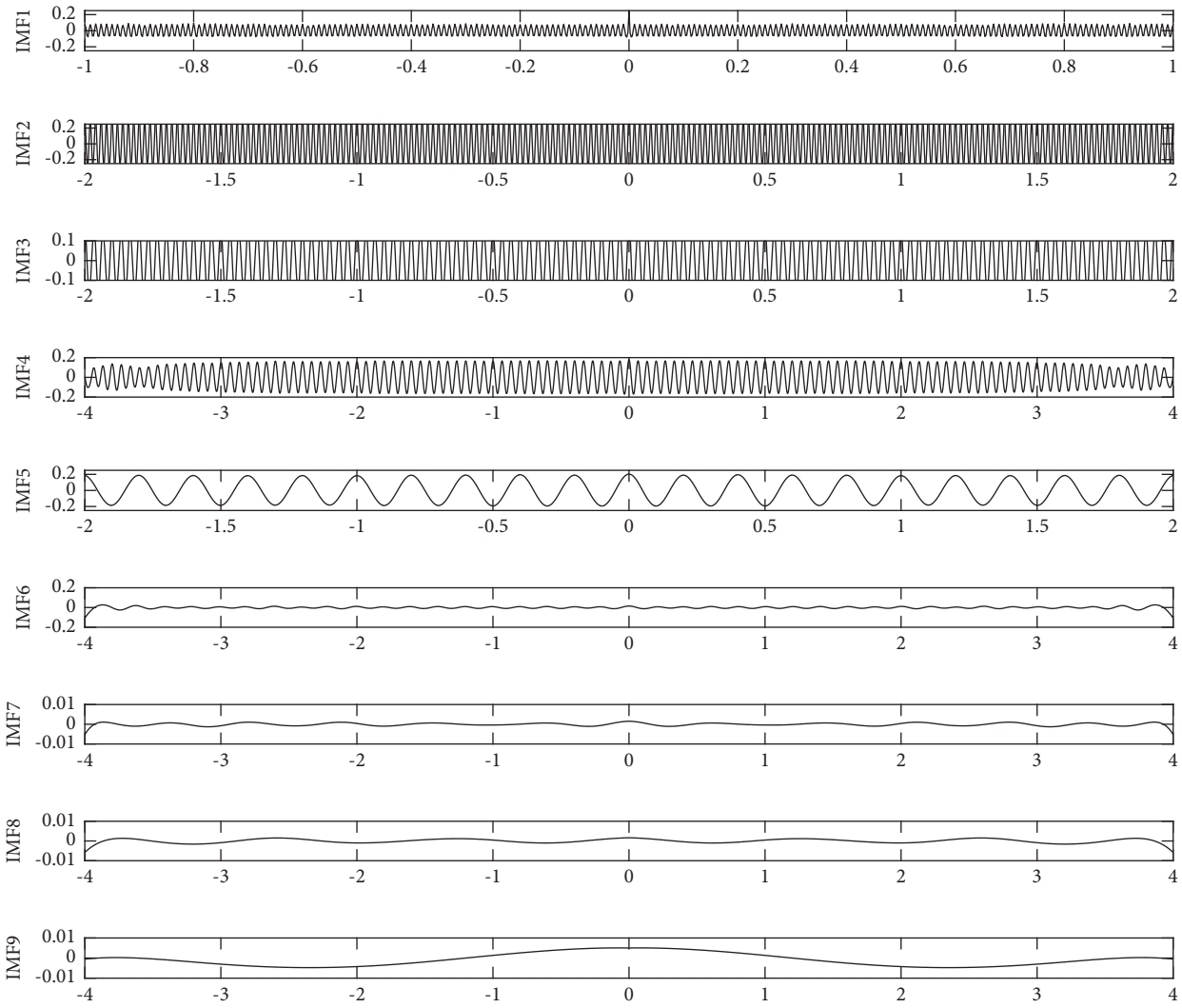


Figure 6: Autocorrelation functions of all IMF components.

used to analyze the test data and the main parameters of the extracted information from periodic longitudinal vibration are obtained, as detailed in Table 3.

In Figure 10(a), the frequencies are mainly distributed in the 5th order trend line. As shown in Figure 10(b), the amplitudes increase with the increasing of the shaft speed until the tail bearing failure occurs. The corresponding peak speed of the 5th order curve is observed to be extremely close to the resonance speed of this marine shaft torsional vibration and longitudinal vibration.

*4.3. Transverse Vibration.* The transverse vibrations of hull come from the sensors of No. 7 and No. 8 in Figure 8. Through the EEAF method, the transverse vibrations of the hull are extracted and the main data filled in Table 4.

Figure 11 shows the characteristics of the periodic components in the hull longitudinal vibration under the different operating conditions which are presented in Table 4. As shown in Figure 11(a), the extracted frequencies are mainly distributed on the line of the 5th order vibration. Similar to the aforementioned processes, the amplitudes of

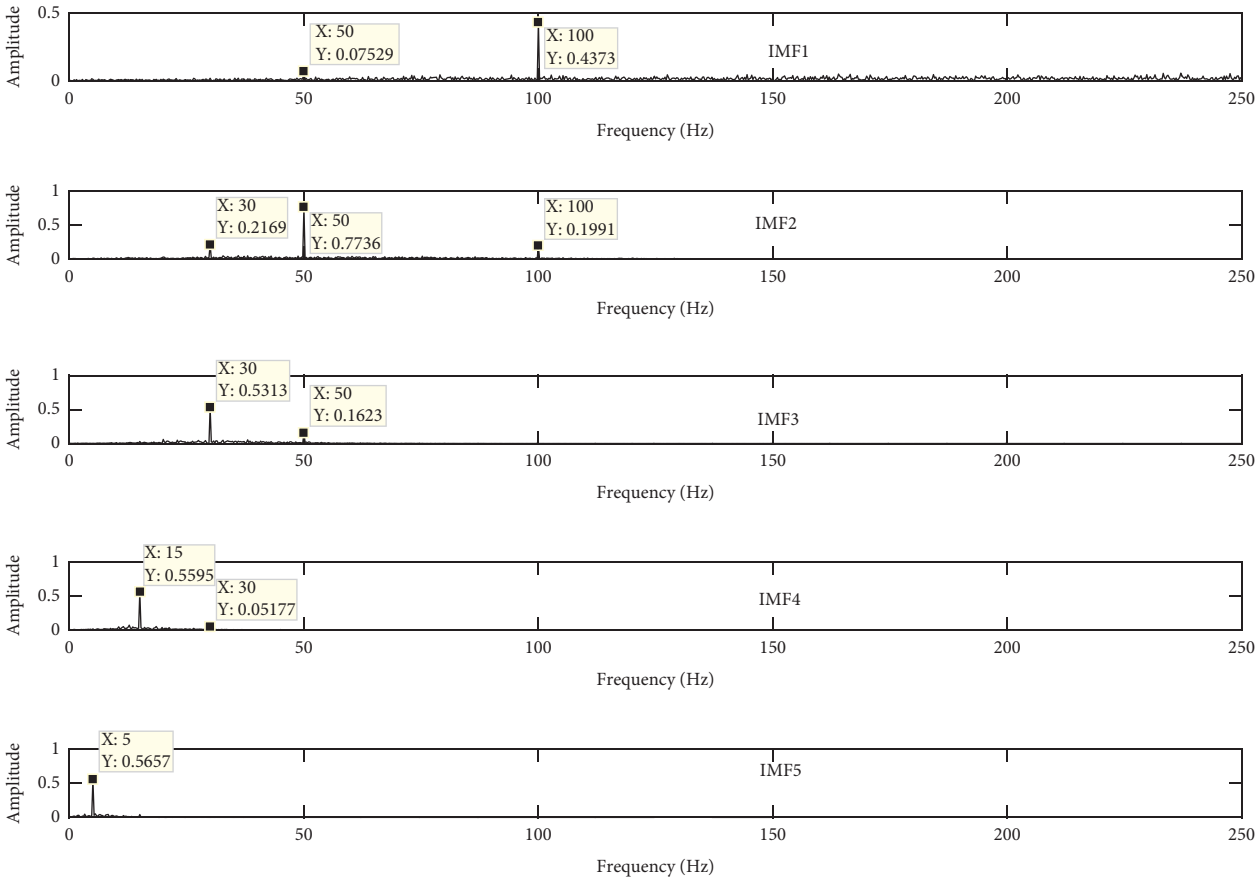


Figure 7: Frequency spectrum of $IMF_1$, $IMF_2$, $IMF_3$, $IMF_4$, and $IMF_5$.

Table 1: Main datum of EEAF method and designated signal.

| Parameters | SN | | | | |
|---|---|---|---|---|---|
| | 1 | 2 | 3 | 4 | 5 |
| Setting frequency | 100 Hz | 50 Hz | 30 Hz | 15 Hz | 5Hz |
| Extracting frequency | 100 Hz | 50 Hz | 30 Hz | 15 Hz | 5Hz |
| Error | 0 | 0 | 0 | 0 | 0 |
| Setting amplitude | 0.6 | 1 | 0.8 | 0.6 | 0.6 |
| Extracting amplitude | 0.6162 | 0.986 | 0.7856 | 0.5932 | 0.5829 |
| Error | 2.7% | 1.4% | 1.8% | 1.133% | 2.85% |

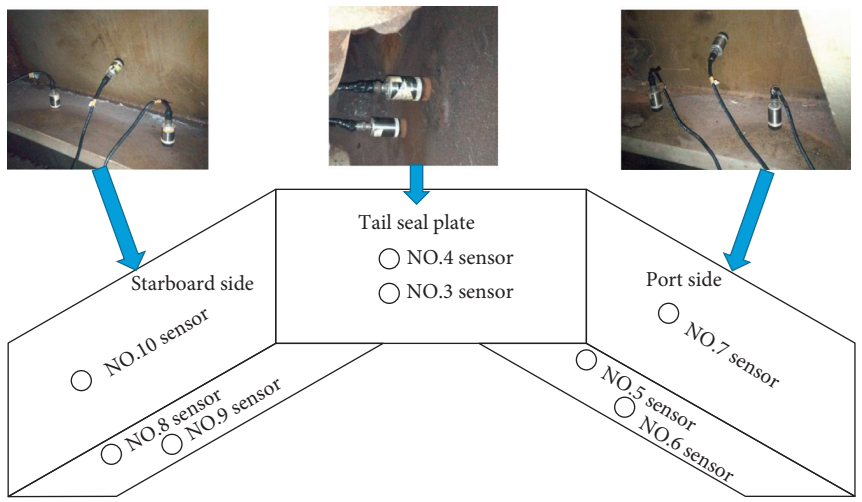


Figure 8: Arrangement of sensors during hull vibration test.

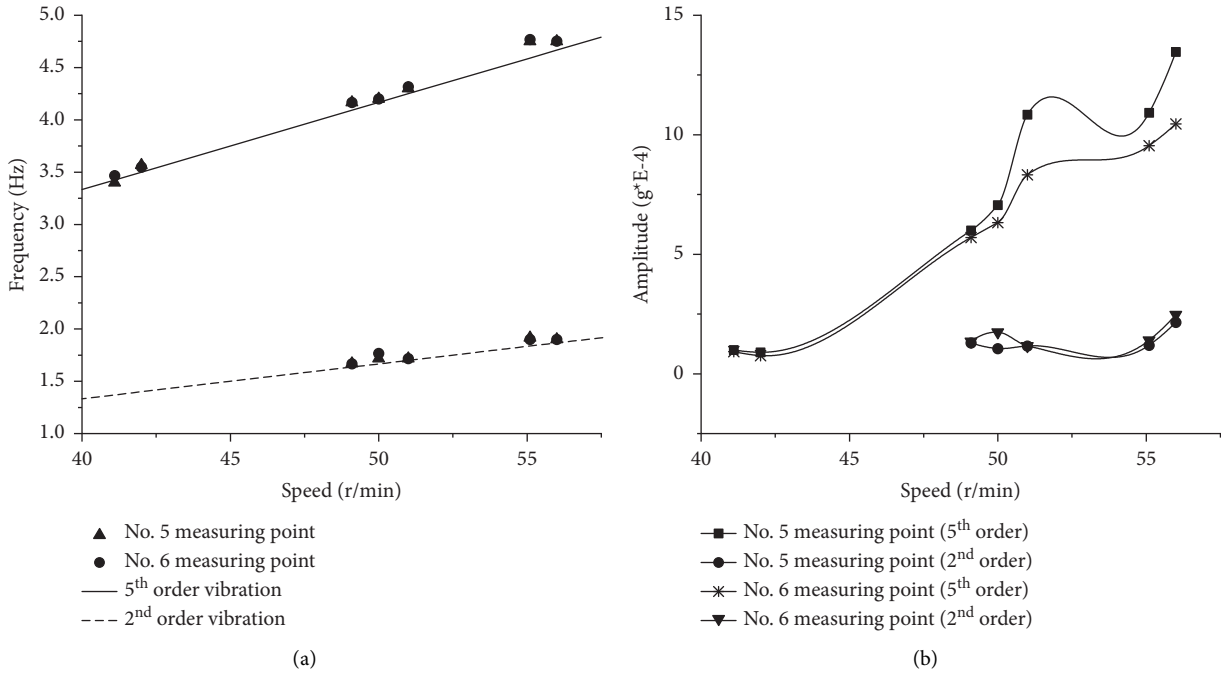


Figure 9: Main parameters of hull vertical vibrations. (a) Frequency (b) Amplitude.

Table 2: Main datum of hull vertical vibrations.

| Speed | Point | | | |
|---|---|---|---|---|
| | No. 5 | | No. 6 | |
| | Frequency (Hz) | Amplitude ($g \bullet 10^{-4}$) | Frequency (Hz) | Amplitude ($g \bullet 10^{-4}$) |
| 33 r/min | — | — | — | — |
| 41.1 r/min | 3.400 | 0.9989 | 3.467 | 0.9301 |
| 42 r/min | 3.567 | 0.8932 | 3.550 | 0.756 |
| 49.1 r/min | 1.670 | 1.297 | 1.667 | 1.355 |
| | 4.167 | 5.994 | 4.167 | 5.696 |
| 50.0 r/min | 1.717 | 1.060 | 1.767 | 1.743 |
| | 4.200 | 7.055 | 4.200 | 6.325 |
| 51.0 r/min | 1.717 | 1.168 | 1.717 | 1.161 |
| | 4.300 | 10.840 | 4.317 | 8.326 |
| 55.1 r/min | 1.917 | 1.196 | 1.900 | 1.399 |
| | 4.750 | 10.920 | 4.767 | 9.544 |
| 56.0 r/min | 1.900 | 2.157 | 1.900 | 2.474 |
| | 4.750 | 13.460 | 4.750 | 10.450 |

Table 3: Main data of hull longitudinal vibrations.

| Speed | Point | | | |
|---|---|---|---|---|
| | No. 3 | | No. 4 | |
| | Frequency (Hz) | Amplitude ($g \bullet 10^{-4}$) | Frequency (Hz) | Amplitude ($g \bullet 10^{-4}$) |
| 33 r/min | 2.333 | 1.044 | 2.333 | 1.276 |
| 41.1 r/min | 3.483 | 2.988 | 3.483 | 2.411 |
| 42 r/min | 3.550 | 4.136 | 3.55 | 3.008 |
| 49.1 r/min | 4.167 | 9.697 | 4.167 | 9.435 |
| 50.0 r/min | 4.217 | 7.567 | 4.217 | 7.608 |
| 50.0 r/min | 4.300 | 11.550 | 4.300 | 11.87 |
| 55.1 r/min | 4.767 | 9.442 | 4.767 | 11.01 |
| 56.0 r/min | 4.750 | 11.340 | 4.750 | 12.96 |

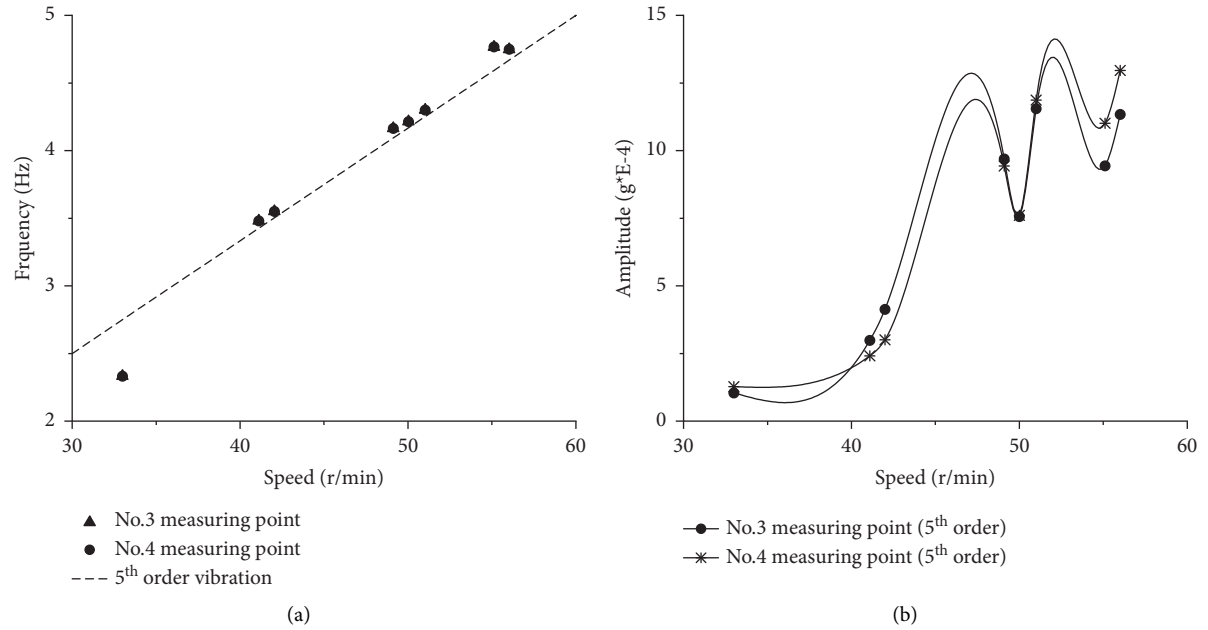


Figure 10: Main parameters of hull longitudinal vibrations. (a) Frequency (b) Amplitude.

Table 4: Main data of Hull Transverse Vibrations.

| Speed | Point No. 10 measuring point | |
|---|---|---|
| | Frequency (Hz) | Amplitude ($g \bullet 10^{-4}$) |
| 33 r/min | 2.817 | 3.904 |
| 41.1 r/min | 3.517 | 5.179 |
| 42 r/min | 3.550 | 5.407 |
| 49.1 r/min | 4.167 | 6.524 |
| 50.0 r/min | 4.217 | 8.956 |
| 50.0 r/min | 4.283 | 5.721 |
| 55.1 r/min | 4.767 | 6.681 |
| 56.0 r/min | 4.750 | 6.823 |

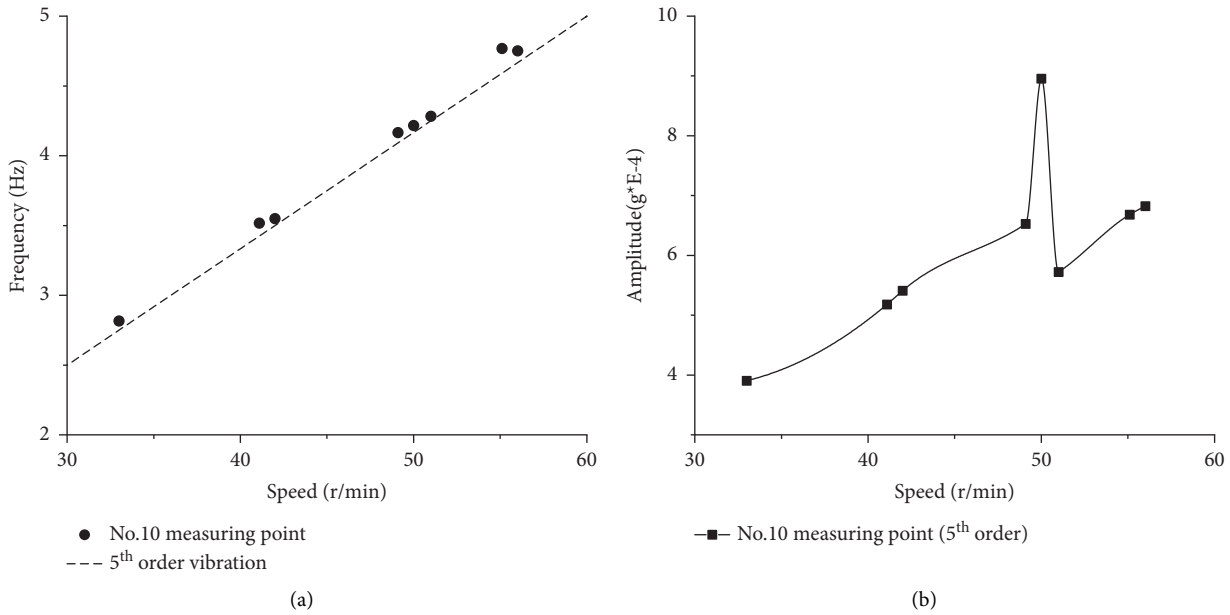


Figure 11: Main parameters of hull transverse vibrations. (a) frequency (b) amplitude.

these frequencies in the 5th harmonics increase firstly and then decrease with the increase of the shaft speed. When the tail bearings are in fault, the amplitudes are observed to increase once again.

## 5. Conclusions

In this study, a novel method of extracting periodic fault information of marine propulsion shafting by the hull vibrations is proposed, which is referred to as the EEAF method. Through the numerical verification, test and discussion, the EEAF method is available to extract the useful frequencies and amplitudes connected with marine shafting's fault. In addition, this method has alleviated the modal aliasing problems successfully, and can decompose and extract the periodic feature quantities which characterize the fault features of marine shafting from the measured signals more accurately. The fault features extracted from the hull vibrations are similar with the phenomena of marine shafting misalignment. So the fault information obtained by EEAF method from hull vibrations can be used to pre-estimate the operating condition of marine shafting qualitatively. However, there should be more experiments and tests to develop the effectiveness and quantitative of the fault diagnosis of the EEAF method.

## Data Availability

The test data used to support the findings of this study are available from the corresponding author upon request.

## Conflicts of Interest

The authors declare that they have no conflicts of interest.

## Acknowledgments

This work was partly funded by the National Natural Science Foundation of China (51479154) and the Natural Science Foundation of Zhejiang Province (LY16E090003).

## References

[1] Y. Qiang, W. Lei, and L. Wei, "Transmission characteristics of propeller excitation for naval propulsion shafting," *Chinese Journal of Ship Research*, vol. 10, no. 6, pp. 81–86, 2015.

[2] P. Jayaswal, S. N. Verma, and A. K. Wadhwani, "Application of ANN, Fuzzy Logic and Wavelet Transform in machine fault diagnosis using vibration signal analysis," *Journal of Quality in Maintenance Engineering*, vol. 16, no. 2, pp. 190–213, 2010.

[3] H. Khang, H. R. Karimi, and K. G. Robbersmyr, "Bearing fault detection based on time-frequency representations of vibration signals," in *Proceedings of the International Conference on Electrical Machines & Systems*, IEEE, Chiba, Japan, November 2016.

[4] N. E. Huang, Z. Shen, S. R. Long et al., "The empirical mode decomposition and the Hilbert spectrum for nonlinear and non-stationary time series analysis," *Proceedings of the Royal Society of London. Series A: Mathematical, Physical and Engineering Sciences*, vol. 454, no. 1971, pp. 903–995, 1998.

[5] W. Zhaohua and E. Norden, "Ensemble empirical mode decomposition: a noise-assisted data analysis method," *Advances in Adaptive Data Analysis*, vol. 1, no. 01, pp. 1–41, 2009.

[6] M. N. Keshtan and M. Nouri Khajavi, "Bearings fault diagnosis using vibrational signal analysis by EMD method," *Research in Nondestructive Evaluation*, vol. 27, no. 3, pp. 155–174, 2016.

[7] J. Zhao, R. Jia, H. Wu, K. Dong, and J. Dang, "Extraction of vibration signal features based on Fast ICA-EEMD," *Journal of Hydroelectric Engineering*, vol. 36, no. 3, pp. 63–70, 2017.

[8] L. Jinming, *Research on Dynamic Influencing Factors of Ship Propulsion Shafting System and EMD Fault Diagnosis Method*, Shanghai Jiao Tong University, China, 2013.

[9] L. Wang, Z. Liu, Q. Miao, and X. Zhang, "Time-frequency analysis based on ensemble local mean decomposition and fast kurtogram for rotating machinery fault diagnosis," *Mechanical Systems and Signal Processing*, vol. 103, pp. 60–75, 2018.

[10] C. Mganb, A. Tmh, and A. Om, "An adaptive variational mode decomposition based on sailfish optimization algorithm and Gini index for fault identification in rolling bearings[J]," *Measurement*, vol. 173, pp. 1–20, 2021.

[11] Z. Wang, L. Yao, G. Chen, and J. Ding, "Modified multiscale weighted permutation entropy and optimized support vector machine method for rolling bearing fault diagnosis with complex signals," *ISA Transactions*, vol. 114, no. 12, 2021.

[12] S. N. Chegini, A. Bagheri, I. Amirmostofian, M. Manjili, and B. Ahmadi, "New bearing slight degradation detection approach based on the periodicity intensity factor and signal processing methods," *Measurement*, vol. 170, p. 170, 2020.

[13] F. Meng, W. Du, X. Gong, H. Li, and G. Xie, "Rolling bearing fault identification based on particle swarm optimization least squares support vector machine," *Bearing*, vol. 493, no. 12, pp. 43–50, 2020.

[14] Q. Chen, S. Dai, and X. Bi, "Fault diagnosis of rolling bearing based on EEMD," *Computer Simulation*, vol. 38, no. 02, pp. 361–364+369, 2021.

[15] H. Su, M. Song, and Z. Xiong, "Bearing fault diagnosis method based on EEMD and adaptive redundant lifting scheme packet," *Vibroengineering PROCEDIA*, vol. 34, no. 1, pp. 14–19, 2020.

[16] P. Zou, B. Hou, J. Lei, and Z. Zhenji, "Bearing fault diagnosis method based on EEMD and LSTM," *International Journal of Computers, Communications & Control*, vol. 15, no. 1, pp. 1–14, 2020.

[17] T. T. Zhou, X. M. Zhu, C. J. Wu, and W.-C. Peng, "Marine propulsion shaft system fault diagnosis method based on partly ensemble empirical mode decomposition and SVM," *Journal of Vibroengineering*, vol. 17, no. 4, pp. 1783–1795, 2015.

[18] Y. Chen and B. Han, "Ship shafting fault detection based on improved envelope analysis," *China Navigation*, vol. 42, no. 02, pp. 22–26+41, 2019.

[19] Y. He, X. Wang, and J. Dong, "A method for feature extraction of ship shafting faults based on empirical wavelet transform and spectral kurtosis," *Chinese Ship Research*, vol. 15, no. S1, pp. 98–106, 2020.

[20] J. Zhang, *Mechanical Fault Diagnosis Technology*, Mechanical Industry Press, Beijing, China, 2nd edition, 2014.

Hindawi
Shock and Vibration
Volume 2022, Article ID 4334398, 12 pages
https://doi.org/10.1155/2022/4334398

*Research Article*

# Vibration Transmission Characteristics and Measuring Points Analysis of Bearing Housing System

**Wenbing Tu,[1] Jinwen Yang,[1] Ya Luo,[1,2] Lianbao Jiang,[3] Jin Xu,[4] and Wennian Yu[3]**

[1]*School of Mechanotronics and Vehicle Engineering, East China Jiaotong University, Nanchang 330013, China*
[2]*State Key Laboratory of Performance Monitoring and Protecting of Rail Transit Infrastructure, East China Jiaotong University, Nanchang 330013, China*
[3]*College of Mechanical and Vehicle Engineering, Chongqing University, Chongqing 400044, China*
[4]*China North Vehicle Research Institute, Beijing 100081, China*

Correspondence should be addressed to Wennian Yu; wennian.yu@cqu.edu.cn

Received 2 December 2021; Accepted 7 February 2022; Published 27 February 2022

Academic Editor: Liu Jing



The vibration transmission characteristics of the bearing housing system are crucial for the system fault diagnosis based on vibration signals collected at various measuring points. To study its vibration transmission characteristics, a dynamic model of the rolling bearing housing system based on the elastic interface is established. The interference fit between the bearing outer ring and the bearing housing is modelled by contact pairs. The proposed model is verified by the experimental results, which demonstrate that the interference fit can be better simulated by contact pairs. Based on the comparisons between the vibration signals obtained from the defect point and the measuring points on the bearing surface, the transmission mechanism of the defect excitation and the generation mechanism of the bearing housing structural vibration are clarified. The change law of defect excitation through an interface and the effects of bearing operational conditions (load and speed) on the vibration signals of measuring points are summarized. The results show that the optimal measuring point on the bearing housing surface is the location that is closest to the defect when the bearing housing system is working under light loads or high speeds. However, when under low speeds, the preferred measuring points are the positions where the rigidity of the bearing housing structure is weak. The analysis results provide a theoretical basis for the sensor arrangement and improvement of fault diagnosis accuracy under different operating conditions.

## 1. Introduction

Rolling bearings are one of the most eventful components in machinery and equipment. The acquisition and analysis of vibration signals are important to monitor their internal operating status [1, 2]. To improve the accuracy of bearing fault diagnosis, it is important to study the vibration transmission mechanism caused by the bearing defect excitations. There has been plentiful research on it in the literature carried out by different scholars [3–5]. Singh et al. [6, 7] analyzed the dynamic contact force and vibration mechanism between the rolling elements and the outer race with the bearing spalling defect. Ahmadi et al. [8] included the mass of the rolling element in their model and studied the relationship between the vibration response and the internal force of the defect bearing. Patel et al. [9] studied the nonlinear vibration response of the bearing with a local defect on the race and investigated the contact relationship between the rolling element and fault. Liu et al. [10, 11] proposed a dynamic model of the planet roller bearing considering the cage crack to detect the initial cage crack failure in the planet roller bearing.

Although scholars have achieved a lot of progress in the study of the vibration mechanism of bearing with defects, the accuracy of fault diagnosis is still limited due to the shortcomings of signal acquisition methods. Traditional methods generally install the sensors on the outer surface of the bearing housing to collect the vibration signals of the

bearing. However, the collected signals cannot faithfully reflect the characteristics of bearing internal excitation due to the inevitable attenuation when the defect excitation transmits through contact interfaces between the bearing outer race and the bearing housing. Moreover, when the transmission route is long, it is difficult to accurately diagnose the fault status inside the bearing. Shao et al. [12] used the experimental methods to study the vibration transmission characteristics of rolling bearings and proposed the energy retention factor to describe the dissipation of vibration energy through multiple interfaces. However, since it is rather challenging to measure the bearing internal excitation, the transmission mechanism between the bearing internal excitation and the outer vibration response collected by the sensors cannot be experimentally investigated. Alian et al. [13] proposed to use the fiber-optic sensors to measure the strain of the rolling bearing for defect diagnosis, which can be mounted inside the bearing. However, most of the current signal processing algorithms are based on the vibration signal, and there are very few for the strain signal.

Therefore, it is necessary to investigate the vibration transmission mechanism along the interface between the outer race and housing for effective fault detection and diagnosis. White [14] took the flexibility of the housing into account and proposed a two-degree-of-freedom dynamic model to study the vibration transmission characteristics of the rolling element bearing. Lim and Singh [15] considered the coupling effect between the bearing and the housing and developed a five-degree-of-freedom dynamic model to investigate the vibration transmission through rolling element bearings. Gao et al. [16] assumed a rigid connection between the outer race and the housing and established a vibration model of the cylindrical roller bearing system, from which the influence of bearing housing deformation on the vibration characteristics was studied. Kraus et al. [17] and Fleming [18] included the flexibility of the bearing housing in their dynamic model and discussed the vibration transmission characteristics of a rotor-bearing housing system. Although the above work focused on the vibration transmission characteristics of the bearing-bearing system, a rigid connection is usually assumed between the outer race and the housing in their models, and the elasticity of the interfaces between them is ignored. These make it impossible to accurately describe the discrepancies between the vibration of the outer race and vibration of the housing caused by the bearing internal excitation.

To address this issue, Liu et al. [19–21] proposed a dynamic model to study the vibration transmission of a shaft-bearing housing system with a localized fault. In this model, elastic interfaces were considered, and the vibration transmission characteristics along multiple interfaces caused by the rolling bearing internal impact excitation were investigated. Xiao et al. [22] established an 8-DOF dynamic model for a gear-shaft-bearing housing system with elastic interfaces and studied the vibration transmission characteristics and energy dissipation characteristics of pulse excitation generated by gear fault passing through multiple interfaces. Although the above models considered the elastic interface relationship between the outer race and the housing, the elastic deformation of the bearing seat is ignored. In addition, the excessive rigidity of the structure will increase the amplitude of acceleration, which is usually neglected. In addition, existing dynamic models cannot reflect the actual interference fit relationship between interfaces. The fit clearance between the rolling bearing outer race and the housing plays a significant role in the vibration response, as argued by Chen and Qu [23]. Thus, the simulation signals obtained by the abovementioned models do not faithfully reflect the practical situations.

With the development of computer science, the finite element method provides an effective way to simulate the actual mechanical properties of the materials and the interference assembly relationship between the bearing and the housing with the elastic interfaces. Wang et al. [24] considered the elastic deformation of the materials and simulated the interference connection between the bearing and the housing using the common nodes. A finite element model for the bearing housing system was established. The transmission characteristics of the vibration signal between the bearing outer race and the housing were investigated to find the optimal position and direction for the measuring points on the housing. The bearing defect excitation was simulated by a periodic impact load in the model, which is quite different from the actual defect excitation. Cao et al. [25] and Xiang et al. [26] regarded the bearing outer race and the housing as a whole to simulate the interference connection of the interfaces. The vibration transmission of the gear-shaft-bearing housing system was investigated, and a structure optimization strategy was proposed to reduce the transmission error. However, the vibration transmission characteristics between the bearing and the housing were not specifically analyzed.

In summary, there are deficiencies in the existing analytical models as they cannot model the elastic deformation of the housing and the connection relationship of interfaces. Although the finite element model can consider the effect of the practical interference connection between the bearing and the housing on the vibration transmission characteristics, it generally uses the sharing nodes to simulate the interference fit of the interfaces, which cannot reflect the actual contact situation. Therefore, a rolling bearing housing system dynamic model still lacks that comprehensively considers the elastic interface, interference assembly relationship, and fault morphology. In addition, the difference between the vibration signals inside the bearing and outside the housing caused by the defect excitation and the distribution law of the optimal measuring points under different speed and load conditions are not sufficiently understood. In this article, a dynamic model of a rolling bearing housing system based on an interference interface and an elastic interface is established. The bearing defect is simplified to a rectangular shape. The interference assembly relationship between the bearing and the housing is modelled by sharing nodes and a contact pair between interfaces. The proposed model is verified by the experimental results, which overcomes the shortcomings of the current models that cannot accurately describe the difference of vibration characteristics between the outer

race and the housing. Based on the analysis of the vibration signals obtained from the defect point and various measuring points on the housing surface, the transmission mechanism of the defect excitation and the generation mechanism of the bearing housing structural vibration are clarified. The effects of load and speed on the defect excitation transmission and structural vibration are studied, which can provide a theoretical basis for optimal sensor placement under different operating conditions and improve the accuracy of bearing fault diagnosis.

## 2. Dynamic Model

*2.1. Problem Description.* In practice, the health condition of the rolling bearing during operation is generally monitored by collecting vibration signals through accelerometers that are mounted on the bearing housing (which is referred to as measuring points in the remainder of this article). Once a defect is generated inside the bearing (either inner race or outer race, balls, etc.), there will be significant periodic impacts in the vibration signals. These impacts are originated from collisions between components with defects and transmit from the interior bearing to the exterior bearing housing. Due to the variations of the vibration transmission path from the defect point to the measuring points, the signals collected at different measuring points caused by the same defect excitation are different, as shown in Figure 1(a). The vibration signal is weakened to varying degrees when it transmits from the excitation source to the surroundings. In addition, because the thickness of the bearing housing is uneven in the circumferential direction, the structural rigidity in each direction is different, and the structural vibration generated at different positions is also different, as shown in Figure 1(b). Therefore, the vibration signals collected by the sensors at different positions on the surface of the bearing housing will be greatly different due to the uncertainty of the defect excitation and the structure vibration.

To study the relationship of the vibration signals between the defect point and the measuring points at different positions on the bearing housing, it is necessary to investigate how the defect excitation is transmitted to the bearing housing and how the structural vibration is generated in the bearing housing. The optimal sensor installation position to obtain the most accurate bearing defect signal can thus be found. It is also noted that both the load and speed affect the defect excitation significantly. Therefore, the effects of the load and speed on the transmission of defect excitation and structural vibration are further studied, which can provide theoretical guidance for the arrangement of sensors and improve the bearing fault diagnosis under different operating conditions.

*2.2. Establishment of Model.* This study takes the cylindrical roller bearing NU306 as the research object. Its main geometric parameters are given in Table 1. The explicit dynamics software package, LS-DYNA, is used for finite element simulation.

Since the cross-section of the cylindrical roller bearing along its axis is the same and only the radial load is supported by the bearing, a two-dimensional model is built for the bearing to improve the computation efficiency. The 2D plane strain element SHELL163 is used as the solid structure for the bearing and the bearing housing in the model. Due to the nonlinearity of the internal contact of the bearing, the triangular mesh should be minimized to ensure the accuracy of the simulation results. Therefore, the bearing housing, the rings, the cage, and the rolling elements are all meshed by quadrangle elements. To obtain accurate dynamic responses, it is generally recommended that the wavelength of the transmission signal should be 20 times larger than the grid size of the structure for wave propagation studies. Considering the outer race as a thin plate, the speed of bending waves $C_b$ is given by [6]:

$$C_b = \sqrt{\omega}\left[\frac{ET^2}{12\,(1-\nu^2)\rho}\right]^{1/4}, \tag{1}$$

where $E$, $\rho$, $\upsilon$, $T$, and $\omega$ are the modulus of elasticity, density, Poisson's ratio, thickness, and angular frequency, respectively. Substituting their values into the above formula, and assuming the frequency is 40 kHz and the thickness of the thin plate is 19 mm, the bending wave velocity is about 2007.73 m/s, and the corresponding wavelength is about 0.0675 m. Thus, the maximum grid size should be smaller than 3.375 mm. To ensure the continuous contact between the rolling elements and the outer race and to minimize the vibration noise caused by the regular polygon effect of the grid, models with grid sizes of 1 mm, 0.5 mm, and 0.25 mm were established for trial calculation, respectively. By comparing the contact force curves between the rolling elements and the races, it was found that the contact force curve is discontinuous when the grid size is large, but it becomes smooth when the grid size is reduced to a certain value. Therefore, in this article, the mesh size of the components with contact behavior (including the races, rolling elements, and cage) is set to 0.25 mm, and the mesh size of the bearing housing without contact behavior is set to 1 mm. The defect studied in this article is located on the outer race. Thus, the mesh in the contacting area of the outer race is refined. There are about 77894 nodes and 75140 elements, which are shown in Figure 2. This article is concerned with the vibrations generated due to a local line spall in the outer raceway, and the defect is simplified into a fully penetrating rectangular recess. The defect is located directly at the bottom of the bearing, whose width and depth are both 1 mm.

The elastic materials are used for the bearing components to consider the influence of the elastic interface between the outer race and the bearing housing. The rolling elements and the races are modelled by the steel GCr15, whose material properties are as follows: density $\rho_1 = 7830\,\mathrm{kg\,m^{-3}}$, modulus of elasticity $E_1 = 206$ GPa, and Poisson's ratio $\nu_1 = 0.3$. The cage is modelled by the brass, whose material properties are as follows: density $\rho_2 = 8500\,\mathrm{kg\,m^{-3}}$, modulus of elasticity $E_2 = 105$ GPa, and Poisson's ratio $\nu_2 = 0.324$. The boundary conditions for the FE model are given as follows:

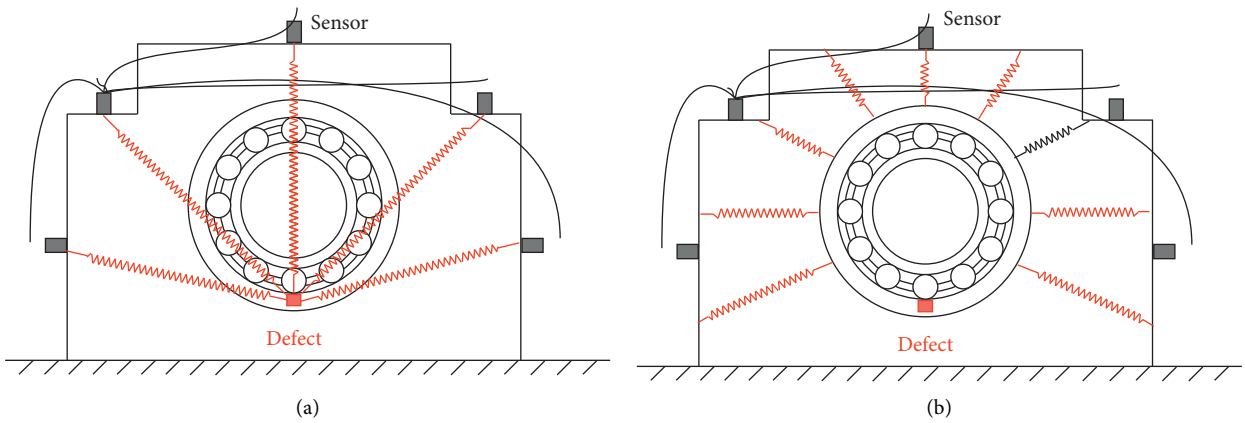


Figure 1: Schematic diagram of defect vibration transmission of the bearing housing system: (a) Defect excitation and (b) structure vibration.

Table 1: Geometric parameters of the cylindrical roller bearing NU306 [4].

| Geometric parameter | Value |
|---|---|
| Roller diameter ($D_r$, mm) | 11 |
| Bearing pitch circle diameter ($D_m$, mm) | 51.5 |
| Bearing inner diameter ($D_i$, mm) | 30 |
| Bearing outer diameter ($D_o$, mm) | 72 |
| Thickness of outer race ($T$, mm) | 19 |
| Contact angle ($\alpha$, °) | 0 |
| Roller number (Z) | 12 |
| Radial clearance between roller and races ($\varepsilon_1$, mm) | 0.01 |
| Cage pocket clearance ($\varepsilon_2$, mm) | 0.08 |

(1) Three different radial loads, i.e., 3000 N, 2000 N, and 1000 N, are applied to the inner surface of the inner race in the negative direction of the $Y$-axis.

(2) Four different speeds, i.e., 700 rpm, 1400 rpm, 2100 rpm, and 2800 rpm, are applied to the inner race in the counterclockwise direction.

(3) All degrees of freedom at the bottom of the bearing housing are constrained, as shown in Figure 2.

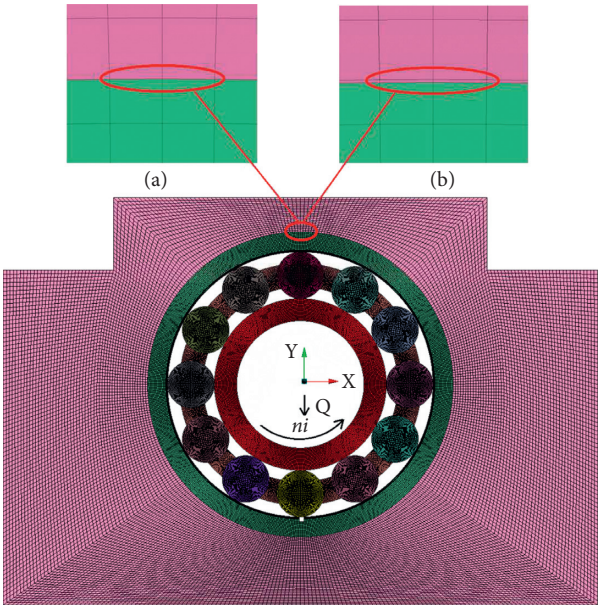


Figure 2: Two-dimensional finite element model of the bearing housing system: (a) common node model and (b) contact pair model.

The basic surface-to-surface contact type in 2D contact is used to simulate the contact situation during bearing operation. A penalty method is used to formulate the contact between two contact components. In this contact algorithm, the slave surface is checked for penetration through the master surface. As shown in Figure 3, in order to determine the positional relationship between two contact points $x^1(\xi^1, t)$ and $x^2(\xi^2, t)$, a gap parameter $g_n$ is defined by

$$g_n = \min \lambda \left\| x^1\left(\xi^1, t\right) - x^2\left(\xi^2, t\right) \right\|, \tag{2}$$

where $\lambda$ is a distance parameter, which is given by

$$\lambda = \begin{cases} 1\left(x^2 - x^1\right)\eta^1 \le 0 \\ -1\left(x^2 - x^1\right)\eta^1 > 0 \end{cases}, \tag{3}$$

where $\eta^1$ describes the normal vector for body #1, and $t$ is the time. In this algorithm, $g_n$ describes the position relationship between the two contact points, with $g_n > 0, = 0$, and $< 0$ representing the two points as in penetration, in contact, and out of contact, respectively. The normal contact force $F_c$ is given by

$$F_c = -\frac{g_n \alpha_f E_b S_b}{\max(\text{shell\_diagonal})} \tag{4}$$

where $\alpha_f$ is a scaling coefficient, whose value is usually considered as 1; $E_b$ is the bulk modulus, which is a function of Poisson's ratio and elastic modulus of the material; $S_b$ is the area of elements in contact.

The inner race, the outer race, and the cage are defined as the master segments, and the rolling elements are defined as the slave segments. Moreover, 36 contact pairs are established for the 12 rolling elements, and each has three contact pairs with the inner race, the outer race, and the cage,

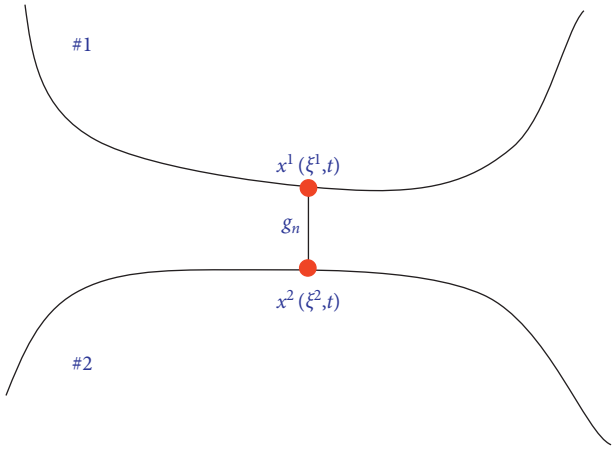


Figure 3: Contact relationship between the contact points.

respectively. The static friction factor is set to 0.01 and the dynamic friction factor is set to 0.005.

In practice, the interference fit is usually used between the outer race and the bearing housing. The interaction and contact deformation between the two interfaces will certainly affect the vibration transmission mechanism due to the bearing defect excitation. Thus, the influence of the elastic interfaces between the bearing outer ring and the housing must be considered. In previous work that uses the finite element model to simulate the interference connection between the outer race and the bearing housing, sharing node model was generally established for the outer race and the bearing housing [24, 27, 28] (i.e., mode #1), which means that the outer race and the bearing housing are considered as a whole body and there is no contact relationship between them, as shown in Figure 2(a). In this work, we use another model (i.e., mode #2) to simulate the interference connection. A contact pair between the outer race and the bearing housing is established, which sets a contact relationship between the interfaces and allows a small amount of penetration between them. To prevent the outer race from rotating, the static friction factor between the outer race and the bearing seat [7] is set to be 0.1, as shown in Figure 2(b).

## 3. Results and Discussion

*3.1. Experimental Verification.* A rolling bearing (NU306) experimental system was set up, as shown in Figure 4. To ensure the consistency between the test conditions and the FE modelling, a defect of size 1 mm × 1 mm (width × depth) was implemented on the outer race of the bearing, and an interference fit was achieved when mounting the bearing outer race on the bearing housing. A radial load of 3000 N was applied on the bearing housing by screwing a thrust device JL1086 and the load was instantaneously measured via a pressure strain gauge. The bearing inner race was driven by a servo motor at a speed of 2100 rpm. The accelerometers were placed on the top surface and side surface of the bearing housing, respectively. After the experimental bearing was running stably, the time-domain acceleration signals collected by the sensors were transmitted to a computer for preliminary analysis and data storage via a signal acquisition card NI USB-4431. The measured acceleration signals are directly compared with the simulation results based on the abovementioned two FE models, as shown in Figure 5. Figure 6 shows the corresponding envelope spectrums of the signals in Figure 5.

From Figure 5, it can be found that the periodic impacts due to the bearing defect are obvious in the simulated signal based on mode #2, which shows a good agreement with the experimental results in terms of the impact shape and amplitude, no matter on the top surface or the side surface of the bearing housing. However, they are very trivial in the simulated signal based on mode #1. From Figure 6, it can be found that the fault characteristic frequency of the simulated signal is approximate to that of the experimental signal. The slight relative error may be caused by the fluctuation of the rotation speed of the cage. This result proves the validity of the proposed model (model #2). In addition, compared with the spectrum based on mode #1, the outer race defect frequency and its harmonics can be more clearly identified in the spectrums based on mode #2 and experimental results. These demonstrate the accuracy of the proposed model in simulating the vibration transmission between interfaces of the bearing outer race and bearing house against the previous model (model #1). In fact, in mode #1, the outer race and the bearing housing are modelled as a whole, and the interaction force between the interfaces that will affect the vibration transmission is ignored. The proposed model #2 can accurately capture the interactions and thus yield consistent results with the experiment. Therefore, it is necessary and reasonable to simulate the interference fit using contact pairs in the finite element model, which can more closely simulate the real operation of the bearing. In the following sections, we will study the vibration transmission characteristics at several measuring points based on the proposed FE model.

*3.2. Vibration Transmission Characteristics of Bearing Housing System and Selection of Measuring Points.* In this section, the vibration transmission characteristics of the bearing housing system at various measuring points will be studied based on the proposed FE model. Since the bearing housing has a symmetrical structure, we consider eight evenly distributed measuring points (marked as points #1, #2, . . ., #8) on half of the bearing housing surface, as shown in Figure 7. The acceleration signal of measuring point #0 is considered as the defect excitation as it is directly located at the defect point. The root mean square (RMS) of the acceleration signals collected at the above points is calculated. The vibration transmission ratio can be expressed by the RMS value at each measurement point with respect to the RMS value of defect excitation. The transmission ratios in the $X$-direction and $Y$-direction are shown in Table 2.

In the actual signal acquisition process, the sensors at the measuring points #1, #2, and #4 are generally used to obtain the acceleration signals in the $Y$-direction, and the measuring points #3, #5, #6, #7, and #8 are used to obtain the acceleration signals in the $X$-direction. According to Table 2,

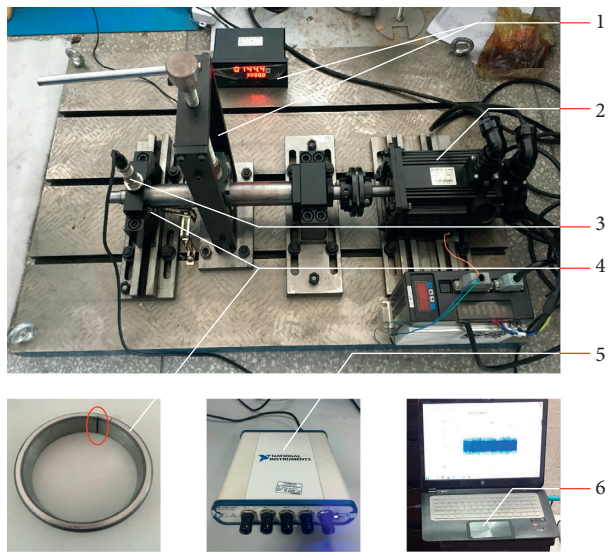


Figure 4: Rolling bearing experimental system (1, radial loading device; 2, servomotor; 3, accelerometer; 4, defect on the bearing outer race; 5, signal acquisition card; 6, computer).

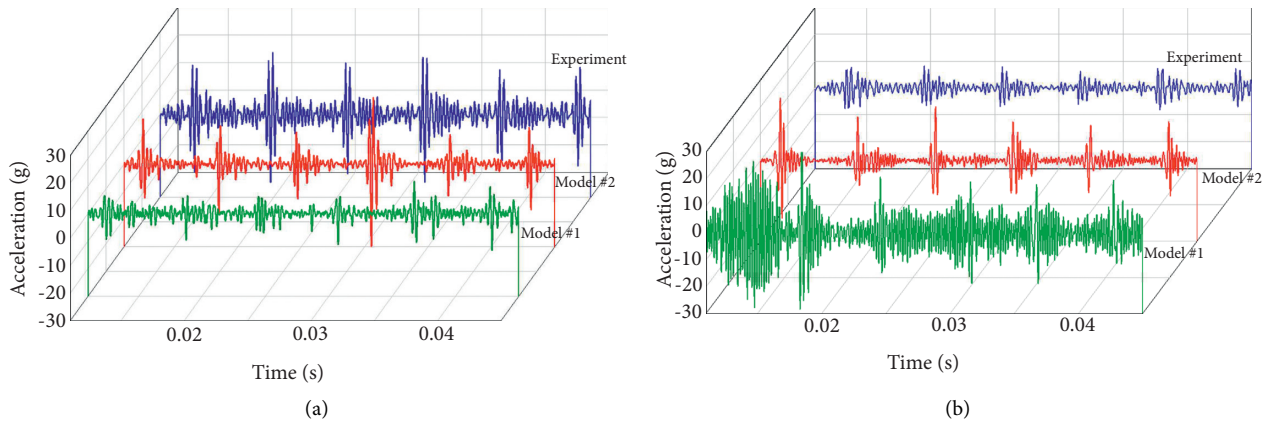


Figure 5: Time-domain acceleration signals from (a) the top surface of the bearing housing and (b) the side surface of the bearing housing.

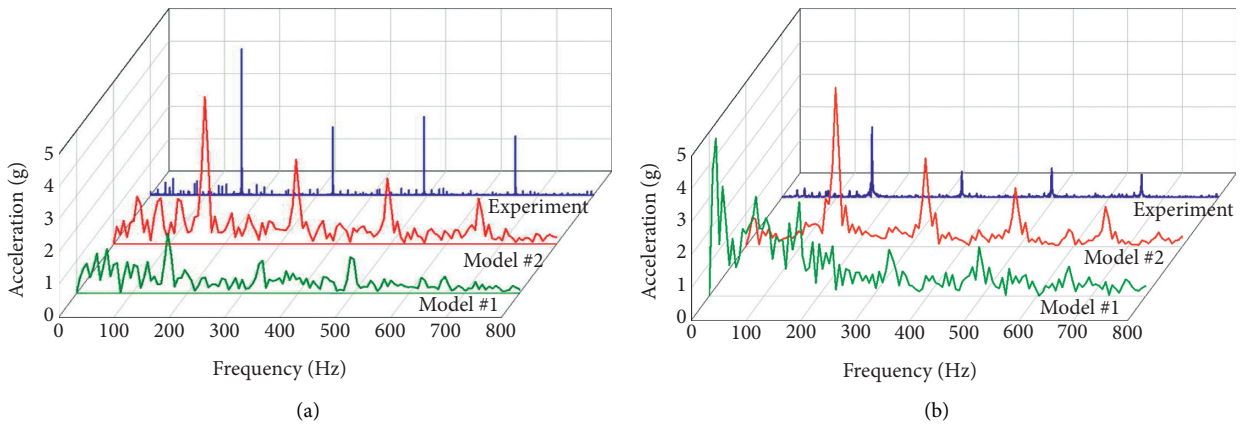


Figure 6: Envelope spectrum of the vibration signals from (a) the top surface of the bearing housing and (b) the side surface of the bearing housing.

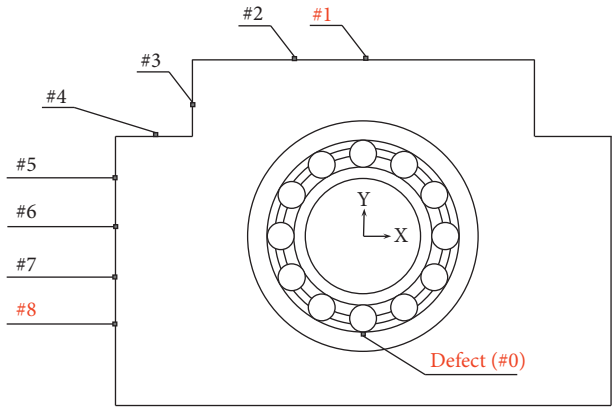


Figure 7: The location of the measuring points.

Table 2: The vibration mission ratio at different measuring points in the $X$- and $Y$-directions.

| Measuring point | Ratio ($X$-direction) | Ratio ($Y$-direction) |
|---|---|---|
| Point #1 | 24.89 | 47.38 |
| Point #2 | 25.63 | 35.22 |
| Point #3 | 24.34 | 40.87 |
| Point #4 | 36.92 | 35.30 |
| Point #5 | 25.84 | 49.08 |
| Point #6 | 27.64 | 30.08 |
| Point #7 | 27.03 | 34.02 |
| Point #8 | 31.23 | 36.85 |

it can be found that point #1 has the largest transmission ratio (47.38%) among the measuring points for acquiring the $Y$-direction signal, and point #8 has the largest transmission ratio (31.23%) among the measuring points for acquiring the $X$-direction signal. These indicate that the vibration energies at these two points are the largest among them all. The reason can be possibly explained by the deformation cloud diagram inside the bearing housing while a rolling element is passing through the defect, as shown in Figure 8. It should be noted that the larger transmission ratio of point #4 and point #5 in the nonvibration-measurement direction is possibly due to the special structure of the bearing housing. The elastic deformation of the bearing housing is considered and point #4 and point #5 are located in the place where the shape of the bearing housing changes sharply. The sharp corner is prone to stress concentration, which causes an abnormal increase in local vibration. Although the transmission ratio of point #4 in the $X$-direction is larger than that of point #8, point #4 is mainly used to obtain the vibration in the $Y$-direction, and the vibration transmission ratio of point #8 in the $X$-direction is still the greatest. Similarly, although the transmission ratio of point #5 in the $Y$-direction is larger than that of point #1, point #5 is mainly used to obtain the vibration in the $X$-direction, and the vibration transmission rate of point #1 is still the largest in the $Y$-direction.

According to Figure 8, as the rolling element passes through the defect, the deformation of the bearing housing gradually decreases from the contact area between the outer race and the bearing housing to the surroundings. It indicates that the vibration of the outer race caused by the defect will be transmitted from the contact area to the surface of the bearing housing. Since point #8 is the closest point to the bearing surface (except the bottom area of housing which is fixed), the vibration at this point is relatively large. In addition, it can be noticed that the deformation cloud near point #1 is always the largest when the rolling element is passing through the defect. Figure 9 shows the profile of bearing housing without and with the deformation (i.e., Figure 8(c)) with an enlarged scale of 200.

Due to the uneven thickness of the bearing housing around the bearing outer race, the structural stiffness around the outer race is different, and the magnitude of deformation is also different. Since the thickness of the housing upper part is the smallest, its structural rigidity is the smallest. In addition, the inner diameter of the bearing housing in the vertical direction is elongated due to the influence of load and defect. Thus, the deformation at the housing upper part near point #1 is the largest.

In conclusion, points #1 and #8 can better reflect the characteristics of the vibration signal due to the defect excitation. This is because that point #8 is the closest point to the defect, and the structural stiffness near point #1 is relatively small. Therefore, the best vibration-measurement point on the surface of the bearing housing should be at the location with a small structural stiffness or closest to the fault.

*3.3. Analysis of Vibration Signals at Measurement Points under Different Loads.* To further investigate the influence of load on the vibration attenuation from the interior defect point to the exterior measuring points, the vibration signals at the defect point and the measuring points are compared. The vibration signals in the $Y$-direction (i.e., the vertical direction) at the measuring point #1 and the defect point (i.e., point #0 as shown in Figure 7) under radial loads of 3000 N, 2000 N, and 1000 N are shown in Figure 10.

It can be seen from Figure 10 that the larger the load, the greater the amplitude of the impulses in the time-domain vibration signals for both points #0 and #1. This demonstrates that the defect characteristics become clearer as the load increases. Compared to point #0, the impact component in the vibration signals at point #1 is weaker, and the noise and other components are more obvious. This is due to the influence of energy dissipation and structural vibration when the vibration signal propagates from the defect source to the measurement point. In the case of a large load, the defect impact in the vibration signals at point #1 is obvious. As the load decreases, the impact components are submerged by noise. The defect characteristics become weaker as the load decreases, and it is gradually impossible to obtain the defect information from the vibration signals collected at point #1.

Figure 11 shows the acceleration signals in the $X$-direction at point #8 and point #0, respectively. It can be seen from Figure 11 that the vibration signals at point #8 are also affected by the load. When the load is large, the defect information can be clearly identified in the vibration signals of point #8. With the decrease of the load, the fault

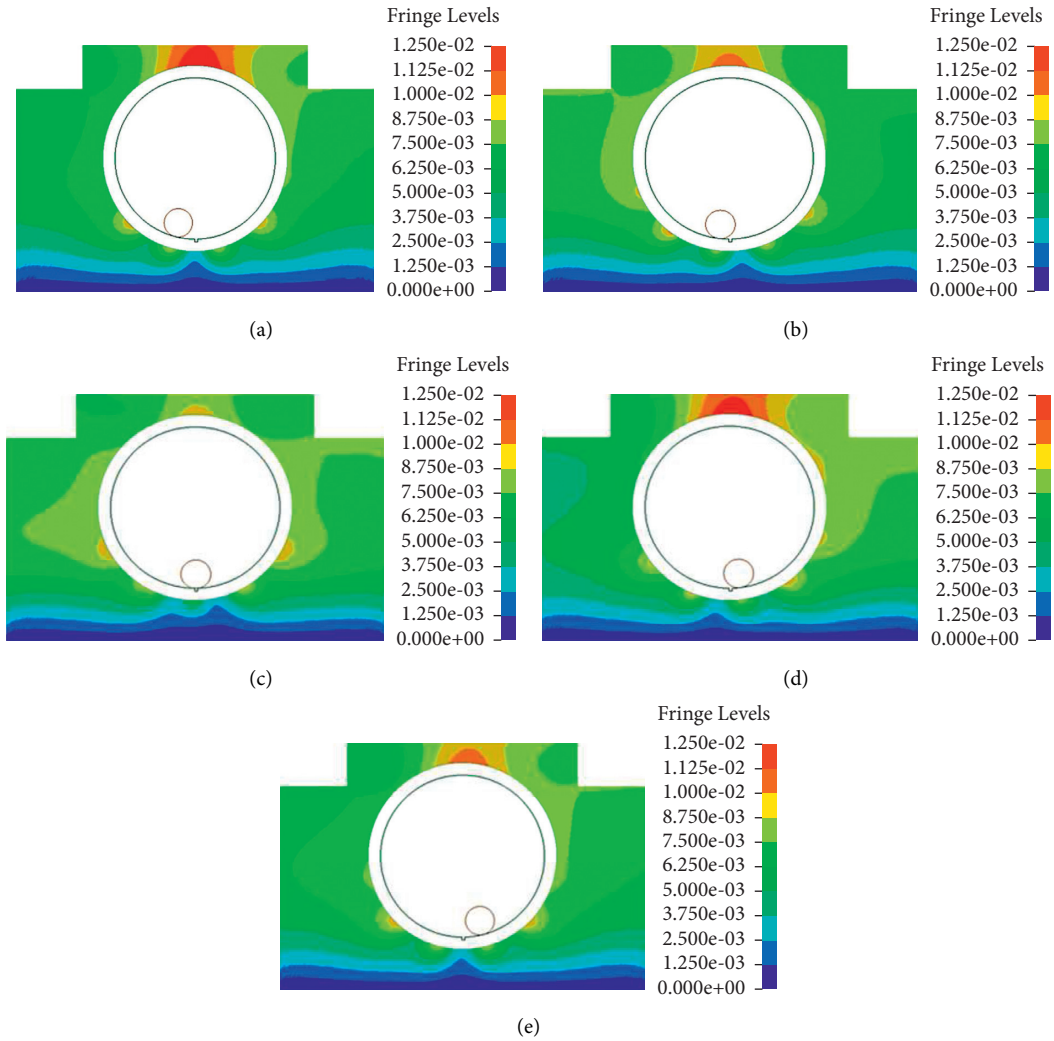


Figure 8: The deformation cloud diagram of the bearing housing while a rolling element is passing through the defect at different time instants: (a) 0.0697 s, (b) 0.0712 s, (c) 0.0727 s, (d) 0.0742 s, and (e) 0.0757 s.

characteristics are getting weaker. However, by comparing Figures 10(a) and 11(a), it is noted that the impact component in the vibration signal at point #8 under 2000 N load is more obvious than that at point #1.

In summary, as the load decreases, the defect characteristics contained in the vibration signals collected at points #1 and #8 become weaker. But under the same load condition, the vibration signal at point #8 is clearer than that at point #1. This is because the structural vibration of the bearing housing is greatly affected by the load, and the attenuation of vibration signal transmission is relatively less. Therefore, under the condition of light load, the sensor should be arranged at the position closest to the fault.

*3.4. Analysis of Vibration Signals at Test Points under Different Speeds.* The vibration signals in the $Y$-direction at measuring point #1 and the defect point #0 under rotational speeds of 2800 rpm, 2100 rpm, 1400 rpm, and 700 rpm are shown in Figure 12.

It can be seen from Figure 12 that the impact impulses due to the defect excitation are more obvious with the increase of speed. This is because the shorter the time interval between two adjacent rolling elements passing through the fault, the less the time required for the attenuation of impact vibration. As the speed decreases, the amplitudes of the vibration signals at points #0 and #1 decrease. The defect characteristics in the vibration signal are much more obvious at a speed of 1400 rpm. With the increase of the rotational speed, the vibration energy increases with the gradual appearance of noise. The impact components generated by the defect are gradually masked, and the defect characteristics in the vibration signals at point #1 become weaker. As the speed decreases, the vibration energy of the bearing decreases. The impact of the fault becomes slight, and the defect characteristics captured by the vibration signals at point #1 are limited.

Figure 13 shows the acceleration signals in the $X$-direction at point #8 and point #0, respectively. It can be seen from Figure 13 that when the speed is large, the vibration signals at

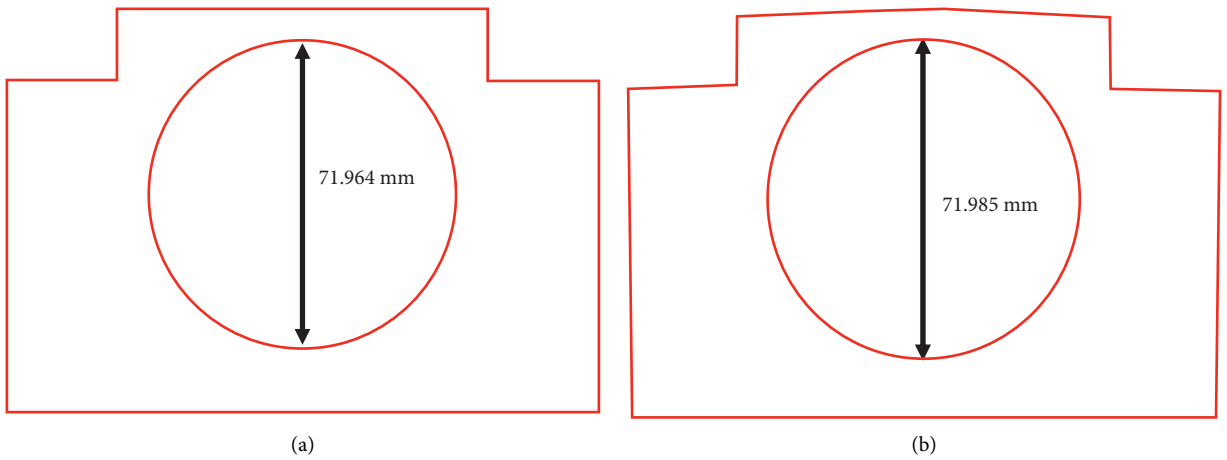


Figure 9: Deformation of bearing housing: (a) without deformation and (b) with deformation based on Figure 8(c) (note that the enlarged scale is 200).

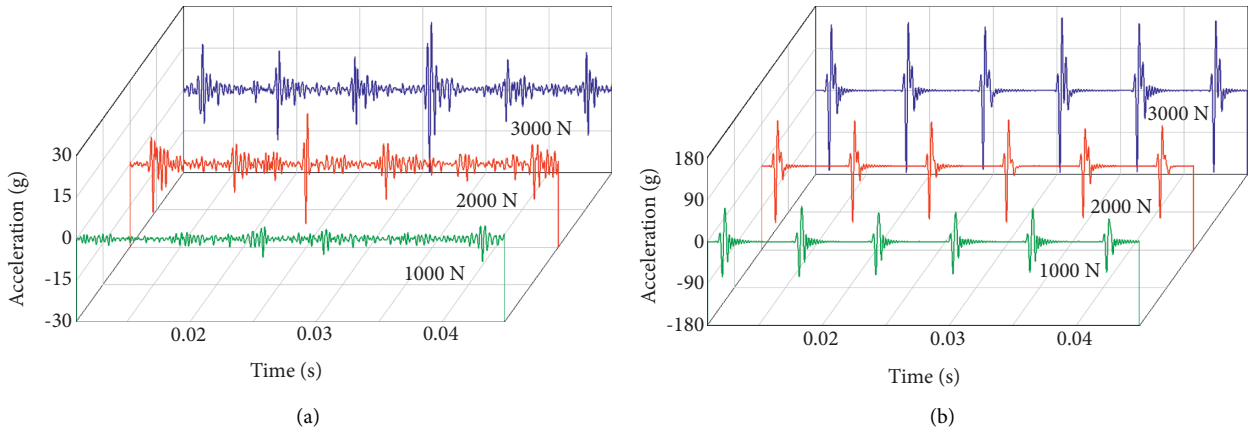


Figure 10: Acceleration signals under different loads at different points: (a) the measurement point #1 and (b) the defect point # 0.

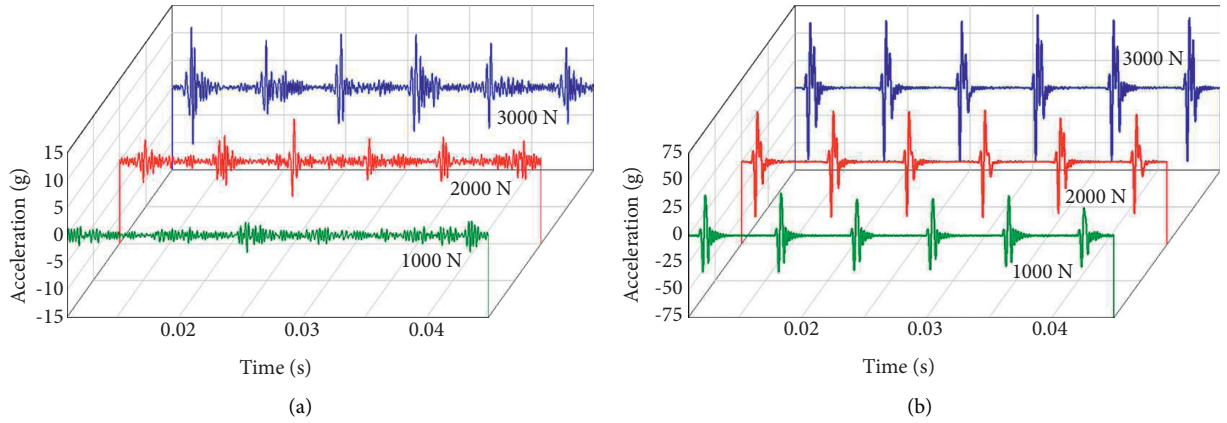


Figure 11: Acceleration signals under different loads at different points: (a) the measurement point #8 and (b) the defect point #0.

point #8 can clearly reflect the defect information. When the speed is small, the vibration signals at point #8 are greatly affected by the speed. When it decreases to a certain degree, it is almost impossible to obtain the defect information from the vibration signals at point #8. Comparing Figure 12(a) with Figure 13(a), it can be seen that when the rotation speed is large, the impact component in the vibration signal at point #8 is more obvious than that at point #1. When the rotation speed

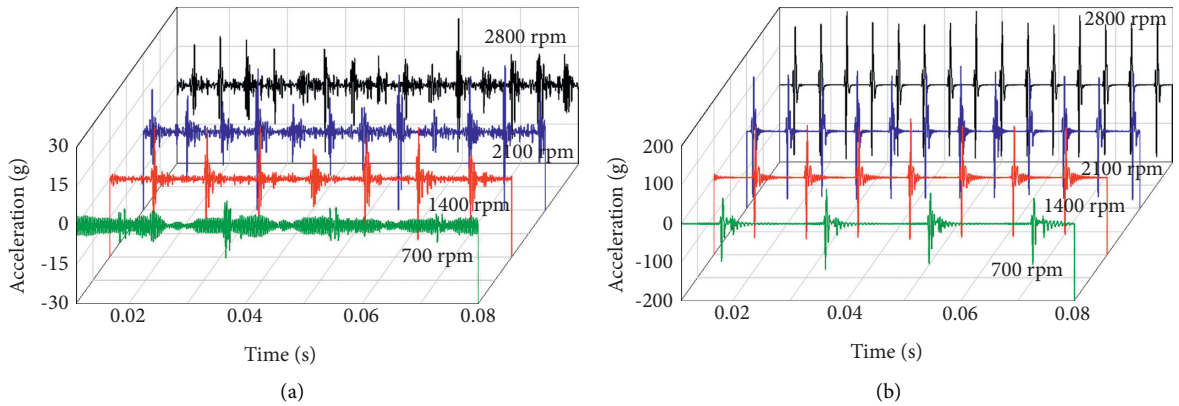


Figure 12: Acceleration signals under different speeds at different points: (a) the measurement point #1 and (b) the defect point #0.

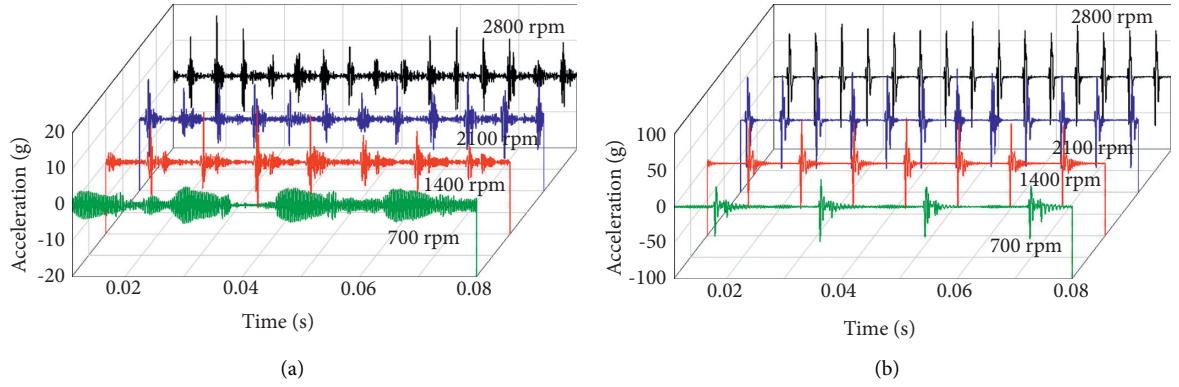


Figure 13: Acceleration signals under different speeds at different points: (a) the measurement point #8 and (b) the defect point #0.

is small, the impact component in the vibration signal at point # 1 is more obvious than that at point #8.

In summary, under the same high-speed working condition, the vibration signal at point #8 is better than that at point #1. Under the same low-speed working condition, the vibration signal at point #1 is better than that at point #8. This indicates that when the rotation speed is high, the influence of the rotation speed on the transmission of defect excitation is smaller than the structural vibration of the bearing housing. On the contrary, when the rotation speed is low, the influence of the rotation speed on the structural vibration of the bearing housing is less than the transmission of the defect excitation. Therefore, the sensor should be placed at the position closest to the fault under the condition of high speed and at the position where the structural stiffness is weakest under the condition of low speed.

## 4. Conclusion

In this article, a novel dynamic model of the rolling bearing-bearing system based on the elastic interface is established. Compared with previous finite element models, the proposed model uses sharing nodes and a contact pair between interfaces to simulate the interferences assembly relationship between the bearing and the housing. This allows the proposed model to faithfully reflect the contact conditions and simulate the attenuation phenomenon when the vibration signal transmits from the interior defect excitation point to the exterior measuring point. An experiment was conducted to verify the proposed model by directly comparing the simulated vibration responses and measured responses at the top surface and side surface of the bearing housing. In addition, the vibration transmission characteristics of the bearing housing system are studied. The influences of load and speed on the vibration signals at various measuring points are analyzed. The conclusions of this study include the following:

(1) The proposed dynamic model using a contact pair between interfaces to simulate the contact condition between the outer ring and the housing can provide a more accurate reflection on the contact interface stiffness and signal attenuation. These enable the proposed model to yield more consistent vibration results with experimentally measured results.

(2) The vibration distribution on the bearing housing surface is related to the bearing housing structure and the fault location. By studying the vibration transmission characteristics of the bearing-bearing housing system, it is found that the optimal measuring points on the outer surface of the bearing housing should be located at the position where the rigidity of the bearing housing structure is weak or the location is closest to the fault.

(3) Under the light load and high speed, the sensor should be placed at the location closest to the fault. However, under the low speed, the sensor should be placed in the position where the rigidity of the bearing housing structure is weak. These findings provide guidance for the sensor arrangement and improvement of fault diagnosis accuracy under different operating conditions.

## Abbreviations

*Symbols*

$C_b$: The speed of bending waves
$D_r$: The bearing roller diameter
$D_j$ ($j = i$, $o$, $m$): The bearing innter diameter ($j = i$), outer diameter ($j = o$), and pitch diameter ($j = m$)
$E_i$ ($i = 1$, 2): The modulus of elasticity of bearing rolling element and races ($i = 1$) and cage ($i = 2$)
$E_b$: The bulk modulus in Figure 3
$F_c$: The normal contact force in Figure 3
$g_n$: The gap parameter in Figure 3
$S_b$: The area of elements in contact in equation (4)
$T$: The thickness of the bearing outer race
$x^k$ ($k = 1$, 2): The positions of the two contact points in Figure 3
$Z$: The number of bearing rolling elements
$\alpha$: The bearing contact angle
$\alpha_f$: The scaling coefficient in equation (4)
$\rho_i$ ($i = 1$, 2): The density of bearing rolling element and races ($i = 1$) and cage ($i = 2$)
$v_i$ ($i = 1$, 2): Poisson's ratio of bearing rolling element and races ($i = 1$) and cage ($i = 2$)
$\omega$: The angular frequency
$\lambda$: The distance parameter in equation (2)
$\varepsilon_1$: The radial clearance between roller and races
$\varepsilon_2$: The cage pocket clearance.

## Data Availability

Data are available upon request through contacting the corresponding author (wennian.yu@cqu.edu.cn).

## Conflicts of Interest

The authors declare that there are no conflicts of interest with respect to the research, authorship, and/or publication of this article.

## Acknowledgments

The research work described in the article was supported by the National Natural Science Foundation of China (Project nos. 51965018, 51865010, and 5210050795).

## References

[1] Y. Yang, C. Liu, and D. Jiang, "Vibration propagation identification of rotor-bearing-casing system using spatio-temporal graphical modeling," *Mechanism and Machine Theory*, vol. 134, pp. 24–38, 2019.

[2] R.-B. Sun, Z.-B. Yang, Z. Zhai, and X.-F. Chen, "Sparse representation based on parametric impulsive dictionary design for bearing fault diagnosis," *Mechanical Systems and Signal Processing*, vol. 122, pp. 737–753, 2019.

[3] J. Liu, Y. Xu, and G. Pan, "A combined acoustic and dynamic model of a defective ball bearing," *Journal of Sound and Vibration*, vol. 501, Article ID 116029, 2021.

[4] W. Tu, J. Yang, W. Yu, and Y. Luo, "Contact characteristic and vibration mechanism of rolling element bearing in the process of fault evolution," *Proceedings of the Institution of Mechanical Engineers - Part K: Journal of Multi-Body Dynamics*, vol. 235, no. 1, pp. 19–36, 2021.

[5] A. Chen and T. R. Kurfess, "Signal processing techniques for rolling element bearing spall size estimation," *Mechanical Systems and Signal Processing*, vol. 117, pp. 16–32, 2019.

[6] S. Singh, U. G. Köpke, C. Q. Howard, and D. Petersen, "Analyses of contact forces and vibration response for a defective rolling element bearing using an explicit dynamics finite element model," *Journal of Sound and Vibration*, vol. 333, no. 21, pp. 5356–5377, 2014.

[7] S. Singh, C. Q. Howard, C. H. Hansen, and U. G. Köpke, "Analytical validation of an explicit finite element model of a rolling element bearing with a localised line spall," *Journal of Sound and Vibration*, vol. 416, pp. 94–110, 2018.

[8] A. Moazen Ahmadi, D. Petersen, and C. Howard, "A non-linear dynamic vibration model of defective bearings - the importance of modelling the finite size of rolling elements," *Mechanical Systems and Signal Processing*, vol. 52-53, pp. 309–326, 2015.

[9] U. K. A. Patel and S. H. Upadhyay, "Nonlinear dynamic response of cylindrical roller bearing-rotor system with 9 degree of freedom model having a combined localized defect at inner-outer races of bearing," *Tribology Transactions*, vol. 60, no. 2, pp. 284–299, 2017.

[10] Z. Shi, J. Liu, H. Li, Q. Zhange, and G. Xiao, "Dynamic simulation of a planet roller bearing considering the cage bridge crack," *Engineering Failure Analysis*, vol. 131, Article ID 105849, 2021.

[11] J. Liu, C. Tang, and G. Pan, "Dynamic modeling and simulation of a flexible-rotor ball bearing system," *Journal of Vibration and Control*, 2021.

[12] Y. M. Shao, Z. G. Chen, X. J. Zhou, and L. Ge, "Study on decaying of shock vibration energy during transmission through multi-interfaces in gear-shaft-bearing-housing system," *Zhendong yu Chongji/Journal Vib Shock*, vol. 6, 2009.

[13] H. Alian, S. Konforty, U. Ben-Simon, R. Klein, M. Tur, and J. Bortman, "Bearing fault detection and fault size estimation using fiber-optic sensors," *Mechanical Systems and Signal Processing*, vol. 120, pp. 392–407, 2019.

[14] M. F. While, "Rolling element bearing vibration transfer characteristics: effect of stiffness," *Journal of Applied Mechanics*, vol. 46, no. 3, pp. 677–684, 1979.

[15] T. C. Lim and R. Singh, "Vibration transmission through rolling element bearings, part I: bearing stiffness formulation," *Journal of Sound and Vibration*, vol. 139, no. 2, pp. 179–199, 1990.

[16] Y. Gao, Z. Li, J. Wang, X. Li, and Q. An, "Influences of bearing housing deflection on vibration performance of cylinder roller bearing-rotor system," *Proceedings of the Institution of Mechanical Engineers - Part K: Journal of Multi-Body Dynamics*, vol. 227, no. 2, pp. 106–114, 2013.

[17] J. Kraus, J. J. Blech, and S. G. Braun, "In situ determination of rolling bearing stiffness and damping by modal analysis," *Journal of Vibration and Acoustics*, vol. 109, no. 3, pp. 235–240, 1987.

[18] D. P. Fleming, *Vibration Transmission through Bearings with Application to Gearboxes*, National Aeronautics and Space Administration Glenn Research Center, Cleveland, OH, USA, 1987.

[19] J. Liu, Y. Shao, and T. C. Lim, "Impulse vibration transmissibility characteristics in the presence of localized surface defects in deep groove ball bearing systems," *Proceedings of the Institution of Mechanical Engineers - Part K: Journal of Multi-Body Dynamics*, vol. 228, no. 1, pp. 62–81, 2014.

[20] J. Liu, Y. Xu, and Y. Shao, "Dynamic modelling of a rotor-bearing-housing system including a localized fault," *Proceedings of the Institution of Mechanical Engineers - Part K: Journal of Multi-Body Dynamics*, vol. 232, no. 3, pp. 385–397, 2018.

[21] J. Liu, C. Tang, and Y. Shao, "An innovative dynamic model for vibration analysis of a flexible roller bearing," *Mechanism and Machine Theory*, vol. 135, pp. 27–39, 2019.

[22] H. Xiao, X. Zhou, J. Liu, and Y. Shao, "Vibration transmission and energy dissipation through the gear-shaft-bearing-housing system subjected to impulse force on gear," *Measurement*, vol. 102, pp. 64–79, 2017.

[23] G. Chen and M. Qu, "Modeling and analysis of fit clearance between rolling bearing outer ring and housing," *Journal of Sound and Vibration*, vol. 438, pp. 419–440, 2019.

[24] B. Wang, J.-y. Zhang, L.-x. Gao, Y.-G. Xu, and L.-L. Cui, "Dynamic response analysis for rolling bearing vibration measuring point," *Journal of Vibration and Shock*, vol. 31, no. 19, pp. 166–168, 2012.

[25] Z. Cao, Y. Chen, and L. Zang, "Model-based transmission acoustic analysis and improvement," *Proceedings of the Institution of Mechanical Engineers - Part D: Journal of Automobile Engineering*, vol. 234, no. 6, pp. 1572–1584, 2020.

[26] C. Xiang, C. Song, C. Zhu, Y. Weng, and W. Guo, "Effects of tooth modifications on the mesh and dynamic characteristics of differential gearbox used in electric vehicle," *Iranian Journal of Science and Technology, Transactions of Mechanical Engineering*, vol. 43, no. S1, pp. 537–549, 2019.

[27] J. Liu, Y. Xu, Y. Shao, H. Xiao, and H. Li, "The effect of a localized fault in the planet bearing on vibrations of a planetary gear set," *The Journal of Strain Analysis for Engineering Design*, vol. 53, no. 5, pp. 313–323, 2018.

[28] X. Yu, Y. Sun, D. Zhao, and S. Wu, "A revised contact stiffness model of rough curved surfaces based on the length scale," *Tribology International*, vol. 164, Article ID 107206, 2021.